

**CHARACTERIZING AND LEVERAGING PROTEIN-SURFACE
INTERACTIONS AND PROTEIN TRANSPORT FOR SEPARATIONS**

by

Ohnmar Khanal

A dissertation submitted to the Faculty of the University of Delaware in partial fulfillment of the requirements for the degree of Doctor of Philosophy in Chemical and Biomolecular Engineering

Fall 2020

© 2020 Ohnmar Khanal
All Rights Reserved

**CHARACTERIZING AND LEVERAGING PROTEIN-SURFACE
INTERACTIONS AND PROTEIN TRANSPORT FOR SEPARATIONS**

by

Ohnmar Khanal

Approved: _____
Eric M. Furst, Ph.D.
Chair of the Department of Chemical and Biomolecular Engineering

Approved: _____
Levi T. Thompson, Ph.D.
Dean of the College of Engineering

Approved: _____
Lou Rossi, Ph.D.
Vice Provost for Graduate and Professional Education and
Dean of the Graduate College

I certify that I have read this dissertation and that in my opinion it meets the academic and professional standard required by the University as a dissertation for the degree of Doctor of Philosophy.

Signed:

Abraham M. Lenhoff, Ph.D.
Professor in charge of dissertation

I certify that I have read this dissertation and that in my opinion it meets the academic and professional standard required by the University as a dissertation for the degree of Doctor of Philosophy.

Signed:

Norman J. Wagner, Ph.D.
Member of dissertation committee

I certify that I have read this dissertation and that in my opinion it meets the academic and professional standard required by the University as a dissertation for the degree of Doctor of Philosophy.

Signed:

Kelvin H. Lee, Ph.D.
Member of dissertation committee

I certify that I have read this dissertation and that in my opinion it meets the academic and professional standard required by the University as a dissertation for the degree of Doctor of Philosophy.

Signed:

Steven M. Cramer, Ph.D.
Member of dissertation committee

ACKNOWLEDGMENTS

I acknowledge everyone who has supported, encouraged, and believed in me throughout my academic and professional career. First, I thank my advisor Bramie M. Lenhoff for his guidance and support. His generosity with his time and his trust in me has fueled this work. I also thank my committee members, Steven Cramer, Kelvin H. Lee, and Norman J. Wagner, as well as Christopher J. Roberts and Millicent Sullivan, for technical discussions, access to their laboratories, group-outing, and lasting encouragements. The guidance, motivation, and companionship from the Lenhoff group members have been invaluable to my learning and satisfaction, particularly those from Vijesh Kumar and Stijn H. S. Koshari. Vijesh Kumar contributed to the modeling aspects of this work in chapters four, five, and six.

I am grateful to Debbie Powell, Jeffery Caplan, and Gerald Poirier for sharing their time and knowledge. I acknowledge the funding from Bristol-Myers Squibb's process development team and their collaboration. Funding through the University Graduate Scholar Award has allowed for additional flexibility in my research.

My family and friends' love and pride have propelled me to where I am. I thank Samuel Scinto for his love and support. My siblings, particularly my sister, Amica Khanal, have been my shade in the sun. Lastly, I extend my deepest gratitude to my biggest advocates, my parents Chandra and Khemlall Khanal, and dedicate this dissertation to them.

TABLE OF CONTENTS

LIST OF TABLES	x
LIST OF FIGURES	xi
ABSTRACT	xx

Chapter

1	INTRODUCTION AND BACKGROUND	1
1.1	Manufacturing of biotherapeutics.....	1
1.2	Depth filtration	5
1.3	Ion-exchange chromatography (IEX).....	7
1.3.1	Emerging fronts in preparative chromatography.....	10
1.4	Outline of the dissertation	11
2	CONTRIBUTIONS OF DEPTH FILTER COMPONENTS TO PROTEIN ADSORPTION.....	14
2.1	Introduction	14
2.2	Materials and methods.....	16
2.2.1	Materials	16
2.2.2	Filter aid and depth filter characterization.....	17
2.2.2.1	Wavelength dispersive X-ray fluorescence spectroscopy (WDXRF).....	17
2.2.2.2	Scanning electron microscopy (SEM).....	18
2.2.2.3	Nitrogen sorption.....	18
2.2.2.4	ζ potential	19
2.2.2.5	Filter aid titration.....	19
2.2.3	Protein batch adsorption experiments	20
2.2.3.1	Protein adsorption on filter aids	20
2.2.3.2	Protein adsorption on cellulose fibers	21
2.2.3.3	Protein adsorption on depth filters	21

2.2.4	Protein adsorption on Zeta Plus-BC25 capsule filters.....	22
2.2.5	Visualization of protein-adsorbed depth filters	22
2.2.5.1	Protein labeling.....	22
2.2.5.2	Protein adsorption for confocal microscopy.....	23
2.3	Results and discussion.....	24
2.3.1	Filter aid characterization	24
2.3.2	Protein adsorption on filter aids	29
2.3.3	Cellulose characterization	31
2.3.4	Protein adsorption on cellulose	32
2.3.5	Depth filter characterization	33
2.3.6	Protein adsorption on depth filters	35
2.4	Conclusions	39
3	THE CONTRIBUTIONS OF ADSORPTION AND SIZE-BASED FILTRATION TO DNA REMOVAL ON DEPTH FILTERS	41
3.1	Introduction	41
3.2	Materials and methods.....	43
3.2.1	Materials	43
3.2.2	Generating dsDNA fragment of 5226 bp	44
3.2.3	Generating dsDNA fragments of 50 and 90 bps	45
3.2.4	dsDNA characterization	46
3.2.5	β -lactoglobulin and DNA labeling	47
3.2.6	Chromosomal DNA labeling and lysate preparation.....	47
3.2.7	Sample loading onto the depth filter	48
3.2.8	Depth filter visualization and image analysis.....	49
3.3	Results and discussion.....	49
3.3.1	DNA vs. protein retention	49
3.3.2	Effect of sample and process parameters	51
3.3.3	Correlations among DNA length, effective size and penetration	53
3.3.4	Effect of wash volume and buffer ionic strength	55
3.3.5	Retention of chromosomal DNA.....	58
3.4	Conclusions	59
4	ESTIMATING AND LEVERAGING PROTEIN DIFFUSION ON ION- EXCHANGE RESIN SURFACES	61

4.1	Introduction	61
4.2	Materials and methods.....	64
4.2.1	Materials	64
4.2.2	Methods	65
4.2.2.1	Chromatography methods	65
4.2.2.2	Mechanistic modeling of chromatography	66
4.2.2.3	Laser scanning confocal microscopy (LSCM)	68
4.2.2.4	Small-angle neutron scattering (SANS)	69
4.2.2.4.1	Background.....	69
4.2.2.4.2	Sample preparation	70
4.2.2.4.3	Data collection.....	71
4.2.2.4.4	Structural models.....	72
4.2.2.4.5	IgG1 form factor.....	75
4.2.2.4.6	Model fitting of resin scattering data.....	75
4.3	Results and discussion.....	77
4.3.1	Surface diffusivity of a protein depends inversely on its binding strength	77
4.3.2	Loading by a decreasing salt and protein gradient promotes faster and more homogeneous mAb uptake	81
4.3.3	The leverage provided by manipulating surface diffusion increases with increasing protein size and affinity	91
4.4	Conclusions	95
5	MULTI-COLUMN DISPLACEMENT CHROMATOGRAPHY FOR SEPARATION OF CHARGE VARIANTS OF MONOCLONAL ANTIBODIES	97
5.1	Introduction	97
5.2	Displacement chromatography principles	100
5.3	Materials and methods.....	104
5.3.1	Materials	104
5.3.2	Methods	105
5.3.2.1	Chromatography method	105
5.3.2.2	Analytical chromatography method	105
5.3.2.3	Methodology for sample displacement chromatography	106

5.3.2.4	Mechanistic modeling	109
5.4	Results and discussion	110
5.4.1	Optimizing the selectivity for mAb variants using one-column breakthrough experiments	110
5.4.2	One-column recycling set-up	114
5.4.3	Two-column set-up.....	115
5.4.4	Three-column set-up.....	117
5.4.5	Predicting displacement behavior in the column using general rate model	119
5.4.6	Implementation approach	123
5.5	Conclusions	125
6	DISPLACEMENT CHROMATOGRAPHY FOR SEPARATION OF HOST-CELL PROTEINS AND PRODUCT AGGREGATES	127
6.1	Introduction	127
6.2	Materials and methods.....	130
6.2.1	Materials	130
6.2.2	Aggregate displacement methods.....	133
6.2.2.1	Batch.....	133
6.2.2.2	Three-column	133
6.2.2.3	Recycle	134
6.2.3	HCP displacement methods.....	135
6.2.3.1	Three-column	135
6.2.3.2	Four-column	135
6.2.3.3	Two-column	136
6.3	Results and discussion.....	136
6.3.1	Aggregate separation by displacement using frontal methods ..	136
6.3.2	Aggregate separation by displacement using sample recycling	138
6.3.3	Aggregate separation by displacement using a multicolumn setup.....	139
6.3.4	HCP separation by displacement.....	144
6.3.5	Significance of displacement in multi-column systems	146
6.4	Conclusions	147

7	CONCLUSIONS AND RECOMMENDATIONS.....	149
	REFERENCES.....	154
Appendix		
A	PUBLICATION REPRINT PERMISSIONS.....	175

LIST OF TABLES

Table 2.1	Elemental compositions of the filter aids compared in terms of their relative mass percentages. Elements lighter than fluorine are not detected.....	25
Table 2.2	BET surface areas of the filter aids, cellulose materials and the depth filters along with their 95% confidence intervals.....	27
Table 4.1	Properties of Fractogel SO ₃ ⁻ M-type resin.	65
Table 4.2	Ligand densities of Fractogel SO ₃ ⁻ M-type variants.	65
Table 4.3	Diffraction settings. The wavelength spread was approx. 12%.	71
Table 4.4	The sum model fitting parameters for the standard neat Fractogel SO ₃ ⁻ (M) resin.	88
Table 5.1	Charge variant profile of different peaks in two-column system.....	117
Table 5.2	Number of cycles, total mass loaded and eluted native variant yield and purity for the three-column experiments.	118
Table 5.3	Parameters resulting from fitting experimental data to the general rate model with a multi-component Langmuir isotherm.....	121

LIST OF FIGURES

Figure 1.1	Simplified depiction of depth filtration and its mechanisms of impurity removal.	6
Figure 2.1	SEM images of dry filter-aid powders. Celpure 100 (A, B), Celite (C, D) and perlite (E, F). Note the difference in magnification between the top and the bottom rows.	25
Figure 2.2	Isotherms for N ₂ adsorption (open symbols) and desorption (filled symbols) onto Celite (□), perlite (○), and Celpure 100 (△). The inset shows the fits to the linear BET equation.....	27
Figure 2.3	(A) Relative surface charge density and (B) ζ potential of Celite (blue) and perlite (red). The vertical line in A denotes the pH at which titration began. The vertical line in B indicates pH 2, which exceeds the PZC values of the filter aids.	28
Figure 2.4	Isotherms for adsorption of catalase, lysozyme and albumin onto Celite (A) in 10 mM phosphate buffer at pH 8, and isotherms for adsorption of lactoferrin (B) and Fc-fusion protein A (C) onto the filter aids in 10 mM phosphate buffer, pH 8, and 10 mM citrate buffer, pH 5, respectively. The black dashed lines show hexagonal close packing limit of the respective proteins.	30
Figure 2.5	Isotherms for N ₂ adsorption (open symbols) and desorption (filled symbols) onto (A) the cellulose fibers used in the 90ZB (□) and the 60SP (○) depth filters, and (B) the 90ZB (□) and the 60SP (○) depth filters. The insets show the isotherm data fitted to the linear BET equation.	31

Figure 2.6	(A) Lysozyme (open symbol) and β -lactoglobulin (closed symbol) coverage on the cellulose fibers used in the 90ZB (\square) and 60SP (\circ) depth filters. The close-packed sphere limits for lysozyme and β -lactoglobulin are shown by the dashed and dotted lines, respectively. (B) Lysozyme (open symbol) and β -lactoglobulin (closed symbol) coverage on 90ZB (\square) and 60SP (\circ) depth filters. The close-packed sphere limits for lysozyme and β -lactoglobulin are shown by the dotted and dashed lines, respectively. (C) Breakthrough curves for mAb B, C and D on 25 cm ² 90ZB05A capsules using 20 mM sodium acetate at pH 5.5. Color-coordinated lines show the masses corresponding to the hold-up volumes. The adsorbed masses of mAb B, C, D and β -lactoglobulin onto the capsules were 2.05, 3.29, 12.99 and 51.85 mg, respectively.....	33
Figure 2.7	SEM images of 90ZB depth filter media at various magnifications. The white dashed line outlines a cellulose fiber whereas the white dashed circle outlines a piece of filter aid. Fibrous webbings on a bed of filter aids are shown in C. Black arrows are to guide the eye.	35
Figure 2.8	Imaging by confocal microscopy of fluorescently-labeled β -lactoglobulin and lysozyme adsorbed individually (A) and simultaneously (B) on 90ZB and 60SP depth filters. The intensities have been enhanced identically in each vertical set for the same protein for ease of comparison of the adsorption of each protein onto the two depth filter media discs. The differences between the red and the green intensities are not to scale.	37
Figure 3.1	Retained CHO genomic DNA (red) and β -lactoglobulin (green) on the 90ZB depth filter; overlapping regions appear orange. (A) β -lactoglobulin was loaded first followed by DNA; (B) DNA was loaded first, then the depth filter was flipped over to load β -lactoglobulin with the flow reversed; (C) DNA and β -lactoglobulin were premixed and loaded simultaneously. Fifteen μ g DNA and 2 mg β -lactoglobulin were loaded in all three cases using 2 mL of 10 mM sodium phosphate at pH 8.	51
Figure 3.2	Retained DNA on the 90ZB depth filter. DNA is shown in red while the depth filter's autofluorescence in the blue region is shown in blue and the overlapping regions appear pink. (A, B) 15 μ g and 500 μ g CHO genomic DNA, respectively, were loaded following the standard procedure. (C) 300 μ g of 90 bp DNA oligo was loaded. All three samples were loaded using 2 mL of 10 mM sodium phosphate at pH 8.	52

Figure 3.3	Retained DNA of (A) 50, (B) 500 and (C) 5000 bp on the 90ZB depth filter. DNA is shown in red while depth filter autofluorescence in the blue region is shown in blue and the overlapping regions appear pink. DNA sample masses of 10 μg were loaded in all three samples using 2 mL of 10 mM sodium phosphate at pH 8.....	54
Figure 3.4	Retention of DNA fragments of 50, 500 and 5000 bp on the 90ZB depth filter represented as the greatest depth into the filter (black) and the % area occupied (red).....	55
Figure 3.5	Effect of wash volume on distribution of retained DNA on the 90ZB depth filter. DNA is shown in red while the depth filter's autofluorescence in the blue region is shown in blue and the overlapping regions appear pink. 15 μg CHO genomic DNA was loaded, followed by a wash volume of 64, 637, 1273 or 2546 L/m ² at 1528 LMH.	56
Figure 3.6	Retention of CHO genomic DNA on 90ZB depth filter as a function of buffer wash volume. Results are represented as the greatest depth into the filter (black) and the % area occupied (red).....	57
Figure 3.7	Retention of 50 bp DNA fragment on 90ZB depth filter as a function of buffer ionic strength. Results are represented as the greatest depth into the filter (black) and the % area occupied (red).....	57
Figure 3.8	Retention of CHO-K1 lysate, its supernatant and pellet after re-suspension, on the 90ZB depth filter are shown in (A), (B) and (C), respectively.....	59
Figure 3.9	Fluorescent particulates from the re-suspended pellet.	59
Figure 4.1	Schematic of protein diffusion in the pore space and on the surface of the resin.	62
Figure 4.2	Schematic of the sum model. Figure not to scale.....	75
Figure 4.3	Experimental uptake curves for cytochrome c (A, B) and mAb (C, D) and their predictions obtained by fixing (A, C) or varying (B, D) surface diffusivities in the mechanistic model.	78

Figure 4.4	<p>MAB surface diffusivities fitted to column breakthrough curves at various pH values (A, C) and resin ligand densities (B, D) are plotted against buffer IS and protein binding equilibrium constant. Data in A and C were for the standard resin and those in B and D were for a buffer pH of 5.5. E) mAb breakthrough and elution curves at 70, 135 and 155 mM IS as well as for a 155-70 mM gradient, all at pH 5. The binding capacities for the samples in E are shown in the table. In panels A and C, black, green and red symbols represent data at pH 6.0, 5.5, and 5.0, respectively. In panels B and D, blue, red and green symbols represent data for the low, standard and high ligand density resins, respectively.</p>	79
Figure 4.5	<p>MAB surface diffusivities fitted to column breakthrough curves of Fractogel SO₃⁻ (M), SP Sepharose Fast Flow and Toyopearl SP-650M at pH 5.0 are plotted against protein binding equilibrium constant. Green triangles, black circles and red rectangles represent Fractogel SO₃⁻ (M), SP Sepharose Fast Flow and Toyopearl SP-650M, respectively.....</p>	80
Figure 4.6	<p>Simulated column-bound protein concentrations during sample loading at pH 5 with a buffer IS of 70 mM (A) or a 155-70 mM gradient (B), and subsequent elution, all as functions of time and column axial position. The corresponding simulated bound protein concentrations within individual resin beads at the column entrance are shown in C and D. Resin particles were removed from the column and visualized (E) after loading of fluorescently-labeled protein in an equivalent manner to the simulation. In both simulations and experiments, the mAb was loaded onto the Fractogel SO₃⁻ (M) column until the DBC was reached. The fluorescence intensity profiles for two particles from each image in E are plotted as a function of normalized radial position in F. In panel F, red circles and purple triangle represent 70 mM pH 5.0, dark green triangle and green square represent 155 mM at pH 5.0, grey square and black circle represent 70 mM at pH 5.6, and dark blue circle and blue triangle represent 155-70 mM at pH 5.0.....</p>	83

Figure 4.7 SANS spectra for the mAb-loaded Fractogel SO₃⁻ (M) resins. The mAb was loaded onto the resin at 70, 112.5, and 155 mM IS, as well as using an IS gradient of 155-70 mM, until the DBC was reached. The spectra are shown in A with the lower and upper insets showing the background incoherent scattering and its correlation to the DBC, respectively. The length scales corresponding to the q-space are provided in blue below the abscissa. The same spectra after background reduction and scaling are shown in B along with the background-reduced spectrum of 7.4 mg/mL pure mAb (right ordinate). The volume-fraction-adjusted sum model is shown in black lines. The blue dotted curve represents the scattering from a 6 mg/mL mAb solution in 100 mM sodium acetate D₂O buffer of pH 5.0. The dashed line is the scattering spectrum of an IgG1 molecule predicted by CRYSON using the PDB ID 1IGY (Harris et al., 1998). Apart from the mAb solution, successive curves are shifted by a factor of 6 for clarity. The arrows at 0.187 Å⁻¹ point to a peak of which the position is interpreted to indicate the nearest-neighbor distance. The lower part of B shows the DBC and the % loss of “protein-occupied pores” with its depiction..... 86

Figure 4.8 A) SANS spectra of neat Fractogel SO₃⁻ (M) resin in D₂O buffers of 155, 112.5 and 70 mM IS at pH 5.0. The length scales corresponding to the q space are provided in blue below the abscissa. After subtraction of the background indicated in A, the intensity was scaled to (1 – the interstitial column void volume) to obtain the form presented in B. The neat resin scattering spectrum was fitted to the sum model, where the lower-q region is primarily affected by the size of the pores modeled by the polydisperse hard spheres (yellow) and the higher-q region is primarily affected by the polymer mesh network modeled by the Lorentz model (white in blue). 88

Figure 4.9	<p>SANS spectra after background subtraction and scaling are shown for the mAb-loaded resins of low (A) and high (B) ligand densities, and cytochrome c-loaded resins (C, D) of high ligand density. The length scales corresponding to the q values are provided in blue below the abscissa. MAb masses of 22.4, 29.4 and 45.4 mg were loaded per mL of low ligand density resin (A) using buffer IS of 35 mM, 45 mM, and a gradient of 55-35 mM at pH 5.5, respectively, until the DBC was reached. (B) Similar data sets at pH 5.5 are shown for the high ligand density resin with mAb (B) loaded at 35 (13.6 mg/mL), 65 (31.4 mg/mL) and 100-35 mM (46.8 mg/mL) IS, and with cytochrome c (C) at 20 (65.4 mg/mL), 85 (75.6 mg/mL) and 150-20 mM (73.5 mg/mL) IS. (D) The scattering spectrum for cytochrome c (65.4 mg/mL of resin) loaded resin at 20 mM IS is shown in red, while the separate spectra for the neat resin and the cytochrome c solution (65.4 mg/mL) are shown in yellow and blue, respectively. The mathematical sum of the spectra for the neat resin and the cytochrome c solution is shown in green. The arrow points to a pronounced peak, the position of which is interpreted to be indicative of the nearest-neighbor distance. .. 93</p>
Figure 5.1	<p>Simulations of zone development along the length of the column for a three-component mixture. Red, blue, and green surfaces represent the adsorbed concentrations of the three components. (A) Simulation for a 25 cm column with load below the column capacity. (B) Simulation for a 25 cm column with load at the column capacity. (C) Simulation for a 25 cm column with load above the column capacity. (D) Simulation for a 50 cm column with load at the column capacity. 104</p>
Figure 5.2	<p>Three-column recycling set-up on the Äkta Explorer. The two three-way valves V1 and V2 are the injection and column direction valves, while V3 and V4 are the column position valves and V5 and V6 are the sample and waste valves, respectively. 106</p>
Figure 5.3	<p>(A-F) Schematics of different stages of three-column displacement chromatography with recycling. (G) Schematic of single-column process with recycling. 109</p>
Figure 5.4	<p>Chromatograms showing the normalized breakthrough curve for each variant using sodium phosphate buffer of pH 6.3 (A), 6.5 (B) and 6.7 (C) at 10 mM sodium phosphate buffer and pH 6.5 (D) at 15 mM sodium phosphate buffer. 111</p>

Figure 5.5	Top panels: Normalized chromatograms showing the breakthrough curve for each variant for each of three mAb variant feed compositions. Bottom panels: The mass of each variant retained within the column as a function of the retention time. The compositions of the acidic-native-basic variants for samples A, B and C were 11.4-63.0-25.6, 17.7-65.0-17.2 and 12.3-51.7-36.0, respectively.....	112
Figure 5.6	The total mass of mAb retained within the column as a function of the retention time for the three cases shown in Figure 5.5.....	113
Figure 5.7	Chromatogram showing the recycled and the subsequently eluted mAb. UV absorbance at 295 nm and conductivity over the course of the experiment are shown in blue and red respectively.....	115
Figure 5.8	Chromatograms showing mAb elution profiles using dual salt-pH gradient in a two-column set-up. UV absorbance and conductivity over the course of the experiment are shown in blue and red respectively. (A) Salt gradient alone. (B) Dual gradient, with pH gradient from 6.5 to 5.5. (C) Dual gradient, with pH gradient from 6.5 to 5.0.....	116
Figure 5.9	Chromatogram showing the absorbance and conductivity obtained in the two-column set-up and the resulting eluted mAb. The elution and loading buffers were of pH 5.5 and 6.5. UV absorbance at 295 nm and conductivity over the course of the experiment are shown in blue and red, respectively.....	116
Figure 5.10	Chromatograms showing five cycles of the three-column experiment and the subsequently eluted mAb. The load buffer was of pH 6.5 and the elution buffer was of pH 6.5 - 5.0. UV absorbance at 295 nm and conductivity over the course of the experiment are shown in blue and red, respectively.....	118
Figure 5.11	Separation of charge variants by a conventional linear gradient of 40 column volumes using column and conditions described in Materials and Methods. (A) Chromatogram showing elution profile. Absorbance at 280 nm and conductivity are shown in blue and red, respectively, while the vertical lines show the fractions collected. (B) Composition and yield of the elution pool as a function of fraction number, shown in descending native variant content, pooled. The horizontal lines indicate the charge variant composition of the load.....	119

Figure 5.12	(Left) Experimental breakthrough curves for samples with various compositions (A, B and C) as well as fits to the general rate model with a multi-component Langmuir isotherm. The variant compositions for A, B and C are as given in Figure 5.5. (Right) Simulated breakthrough curves of the acidic, native, and basic variants showing the exiting protein mass per bed volume as a function of time. No basic variant was seen exiting columns of 20 and 25 cm under a loading of 45 mg/mL resin in the simulation.	122
Figure 5.13	3-D depictions of the charge variants' predicted concentrations as a function of the column axial position and time in a 15 cm column using the simulations of the mechanistic model. Concentrations are shown (A) on the solid phase and (B) in a 2-D projection of (A).....	123
Figure 6.1	(A-C) Schematics of displacement approaches used for aggregate removal: (A) batch experiment conducted on a stir plate, (B) three-column displacement chromatography with partial recycling, and (C) recycling. (D-F) Schematics of displacement approaches used for HCP removal: (D) three-column displacement chromatography with partial recycling, (E) four columns in series, and (F) two-column recycling.	132
Figure 6.2	(A) mAb breakthrough curves generated at 300 cm/hr using 32 mM ionic strength acetate buffer, pH 5 (black circles), 5.5 (red rectangles), and 5.75 (green triangles), and 12 mM ionic strength phosphate buffer, pH 6.2 (blue diamonds). The open and closed symbols represent the monomer and the aggregate, respectively. The abscissa has been adjusted to align the monomer breakthrough curves for ease of comparison. (B) Dependence of monomer displacement and thus aggregate removal on linear velocity determined from breakthrough data. (C) Aggregate content in the solution outside the dialysis device measured over time for the batch experiment depicted in Figure 6.1A at 35 mM ionic strength, pH 5.75. (D) Aggregate content in the tubing depicted in Figure 6.1C, across rounds of recycling. The black and blue bars depict % aggregate for feed concentrations of 12.3 and 4.3 mg/mL, respectively, while the dotted red line represents the yield for both. (E) The effect of sample concentration on aggregate removal using recycling (Figure 6.1C) is represented by black circles, while the recycle and concentrate approach at a starting concentration of 3.5 mg/mL is depicted by the red triangle.....	141

- Figure 6.3 Elution schematic (A) and chromatogram (B) for the three-column approach depicted in Figure 6.1B. The aggregate content in elution from each column across different cycles is presented in (C), while the combined aggregate content between column 2 and 3 and the recovery from those two columns for the respective cycles are presented in (D). 142
- Figure 6.4 HCP and mAb content in the column eluates of four-column set-up depicted in Figure 6.1E with a starting HCP concentration of 20 ppm (A) and 1630 ppm (B), two-column recycling approach depicted in Figure 6.1F with a starting HCP concentration of 23 (D) and 1558 ppm (E), and three-column set-up depicted in Figure 6.1D (F). The chromatogram for the two-column recycling set-up depicted in Figure 6.1F is shown in (C). 143

ABSTRACT

Purification is the current bottleneck in the production of biologics, accounting for well over half of the total manufacturing cost. Purification productivity requires a high capacity and efficient impurity removal. Depth filtration and ion-exchange chromatography are two widely-used purification unit operations. The adsorbing protein may be an impurity originating from the host cell, as is in the case of depth filtration, or the product of interest, as in most cases of ion-exchange chromatography. The performance of these purification steps depends upon the adsorption equilibrium between the adsorbent and the adsorbate and the transport of the adsorbate through the adsorbent. This work describes characterization of depth filters to inform their function and uses fundamental aspects of protein-adsorbent affinity and protein diffusivity to develop new methodologies to overcome capacity and separation limitations of ion-exchange chromatography.

For depth filters, which are routinely used for clarification of cell-culture harvest but are not yet well understood, this work characterizes their microstructure and the mechanisms by which each element contributes to the removal of impurities through adsorption. First, the adsorption of model proteins and monoclonal antibodies (mAbs) onto depth filters and their components was correlated to measured properties such as surface area, morphology, surface charge density, and composition. The polymeric resin binder was shown to be the primary contributor to the depth filter's adsorptive functionality. Monolayer coverage can be used to estimate the capacity for proteins that adsorb.

In addition to proteins, depth filters have been shown to reduce the DNA content of the filter load by tenfold or higher. Given the lengthy and stiff nature of genomic DNA, this work evaluates exclusion, adsorption, and displacement of DNA, in its form as a process impurity, on a commercial depth filter. Through non-destructive covalent labeling and visualization of retained DNA on depth filters, retention by adsorption – driven primarily by electrostatic interactions – was distinguished from retention by size-based filtration. Furthermore, the extent to which DNA, as a process impurity, is solubilized and removed via adsorption/exclusion was probed by labeling DNA in cells and examining its retention after cell lysis.

In ion-exchange chromatography, the impact of protein-adsorbent affinity on protein diffusivity is exploited to improve protein transport into the adsorbent. By exploiting protein surface diffusion, an original method to dramatically improve the attainable transport-limited binding capacity was devised. The method modulates the protein surface diffusivity of the load components by the transient control of buffer ionic strength to increase the rate of protein transport into the resin. The impact of enhanced protein surface diffusion on resin saturation was corroborated using mechanistic modeling, microscopy, and small-angle neutron scattering at various relevant length scales. The findings and the proposed method increased the protein uptake efficiency of a commercial resin by up to 43%, corroborating the importance of protein surface diffusion in protein transport in ion-exchange chromatography.

Compared to protein transport, the protein-adsorbent affinity impacts separation more directly. In this work, we altered the traditional process configuration and methodology to enhance the separation of proteins with similar affinities for the adsorbent. In addition to an ionic environment conducive to competitive adsorption,

saturated loading was shown to promote the displacement of more weakly-binding moieties by more strongly-binding counterparts. Displacement among the mAb product and impurities result in a distribution of impurities along the length of a single- or multi-column system, with the mAb separating the relatively more basic group of impurities from those that are more acidic. The proposed displacement chromatography methods, development and optimization of which were aided by column modeling, afford efficient preparative-scale separation of product isoforms, aggregates, host-cell protein impurities, and other groups of proteins.

In general, this dissertation addresses the retention, adsorption, competitive binding, and transport of biomacromolecules in the realm of depth filtration and ion-exchange chromatography. The presented methods to characterize depth filters are invaluable in the understanding of their structure-function relationships. Furthermore, the methodologies and techniques developed here, using our fundamental understanding of protein adsorption and protein transport, can be employed to address the current challenges facing protein separation and beyond

Chapter 1

INTRODUCTION AND BACKGROUND

1.1 Manufacturing of biotherapeutics

The burgeoning field of biotechnology has benefitted from the elucidation and exploitation of nature's complexity, starting from the insertion and efficient replication of foreign DNA in bacteria in 1972 (Russo, 2003). In the last few decades, the emergence of genome-editing technologies, open-access standardized biological parts, and a several-fold reduction in the cost of DNA sequencing and synthesis have accelerated the development of biologics (National Academies of Sciences, Engineering, 2017). These include recombinant proteins, large peptides, antibody-based proteins, soluble receptors, and vaccines. Among these, antibody-based drugs such as monoclonal antibodies (mAb), antibody-drug conjugates (ADC), nanobodies, bi-specifics, and fusion proteins are designed to be more potent, to bind to dual biological targets and to modulate the cell-mediated immune response (Sifniotis et al., 2019).

Biologics offer the benefits of high specificity to the targets with lower toxicity and reduced drug-drug interactions than traditional small-molecule drugs since they are metabolized and eliminated as endogenous moieties (Oo and Kalbag, 2016). They have transformed patient care, compared to small molecules, in the treatment of an increasing number of diseases such as cancer, infections, autoimmune disorders, and cardiovascular and neurological diseases (An, 2018). However, the structural

complexity of proteins and their high specificity come at the cost of a high sales price, stemming from a complex process of drug discovery, development, and production.

Consistent and efficient production of new and current protein therapeutics in cells, which are inherently variable, is not trivial. Companies face strict regulatory requirements while needing to deliver drug products reliably. The high demand for protein biologics, such as mAbs, is met by stable mammalian cell lines optimized for expression efficiency, scalability, and reproducibility. The mAb must then be harvested and purified to a required standard to reduce the risk of immunogenicity, which can adversely affect the drug's efficacy and patient safety. The impurities can be categorized as process-related, i.e., stemming from the host cell or the processing materials (e.g., DNA, host-cell proteins (HCP), leached affinity chromatography ligand), or product-related (e.g., fragments, aggregates and charge variants of a mAb).

The structural and biochemical similarities among mAb products have enabled a platform purification process for the removal of impurities. The process begins with the clarification of the harvest cell-culture fluid (HCCF) to remove cellular debris and lower the bioburden on the succeeding costly unit operation, affinity chromatography for mAb capture. Depending on the cell-culture density and viability, the harvested fluid can be clarified using centrifugation, tangential-flow filtration, depth filtration, or a combination thereof (Sharma et al., 2017). Disposable depth filters complement centrifugation by removing particulates that are too small to sediment rapidly. In addition to its particulate filtration function, depth filtration improves the clearance of molecular impurities such as HCP and DNA (Yigzaw et al., 2006a). The second chapter of this work characterizes and quantifies the contributions of the depth filter components to its adsorptive capacity for proteins. The third chapter evaluates the

retention of DNA in different physical forms to inform the removal of DNA as an impurity or as a therapeutic product.

Following the clarification of cell-culture broth, multiple stages of chromatography are used to remove remaining contaminants. Unlike analytical chromatography, preparative chromatography involves the separation of the desired product from impurities in a large quantity of feed. Affinity chromatography, such as performed using a protein A resin, is often employed first as it effectively and selectively captures the mAb due to its high selectivity for IgGs. Polishing steps can then be used to remove remaining contaminants that can adversely affect the product quality and shelf-life, or patient safety. Depending on the biophysical properties of the mAb, such as its isoelectric point and molecular weight, polishing steps may include ion-exchange, size-exclusion, hydrophobic-interaction, and multi-modal chromatography. Ion-exchange chromatography is the most widely-used chromatographic unit operation and is present at least once in most mAb purification processes (Liu et al., 2010). Since most mAbs are basic, cation-exchange chromatography is employed to selectively bind the cationic mAb below its isoelectric point and aid in the removal of protein A, HCP, mAb aggregates, charge variants, and fragments. After polishing, the mAb must be concentrated into an appropriate buffer to be formulated into the drug product and packaged accordingly.

The series of stages of product development, starting from biologics discovery to the last stage of production, is costly compared to that of small-molecule drugs. However, biologics generate substantial revenue (Aggarwal, 2010), given that a relatively larger percentage of preclinical-stage biologics (24.4%) persist into the market compared to that of small molecules (7.1%). Particularly in the USA, upon

patent expiration biologics also face less competition from biosimilars, which are required to be clinically equivalent to the innovator drug (Mulcahy et al., 2018). Given that biologics accounted for only 1% of all prescriptions but made up 28% of total medication expenditures as of 2016, biosimilars have the potential to reduce the cost of health care (Gutka et al., 2017). However, despite its production in an inherently-variable biological expression system and purification in a different manufacturing facility, a biosimilar must have a similar quality to that of the innovator product. The quality attributes include sequence, structure, post-translational modifications, charge variants, the extent of degradation, aggregation, and HCP content (Gutka et al., 2017).

Aggregates and degraded fragments of the product mAb are the most abundant group of impurities in the mAb production process. While mAb fragmentation occurs primarily due to proteolytic degradation during cell culture (Vlasak and Ionescu, 2011), aggregates can continue to form during the low-pH elution during affinity chromatography and the subsequent viral inactivation step (Arosio et al., 2013; Liu et al., 2010). Aggregates are of particular concern in the production of biosimilars since they may elicit an immune response (Claman, 1963; Gamble, 1966; Moore and Leppert, 1980). Given that some commercial products have a significant non-critical aggregate content, whether biosimilars must match the innovator product's aggregate content or meet the established product quality standard is debated (Gutka et al., 2017). Chapters 5 and 6 of this work present an adaptable multi-column ion-exchange chromatography system for efficient and effective removal of not only mAb aggregates but also mAb charge variants and HCP.

Charge variants are a group of product-related impurities arising from certain post-translational modifications that change either the net charge of the protein or the

local charge distribution along with the structure. These changes include loss of positive charges from cleavage of C-terminal lysines or a gain of negative charges from deamidation. Variations such as oxidation of the Fc region or asparagine deamidation in the complementarity-determining region (CDR) may reduce the antigen-binding affinity and the potency of the mAb (Leblanc et al., 2017). Biosimilars must also match the charge variant composition of the innovator product.

Biosimilars must also demonstrate reduction of the total HCP content below the established standard. However, even below the set threshold, a small group of host-cell proteins may still pose an immunogenic risk (Bailey-Kellogg et al., 2014) or reduce the stability of the drug product (Bee et al., 2015; Dixit et al., 2016; Gao et al., 2011).

1.2 Depth filtration

The high-cell-density cell-culture fluid must be clarified into a low-turbidity fluid prior to the more specific product purification steps. There are different approaches to removing whole cells, cellular debris and insoluble particulates, such as centrifugation, depth filtration, flocculation, tangential-flow filtration and acoustic aggregation. Among these approaches, primary clarification is often carried out using depth filtration, along with centrifugation (Liu et al., 2010). As its name suggests, a depth filter retains cell debris and other particulate contaminants across its depth, as shown in Figure 1.1.

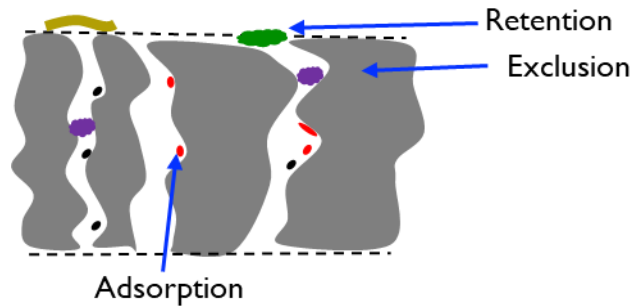


Figure 1.1 Simplified depiction of depth filtration and its mechanisms of impurity removal.

A typical depth filter is a disc or sheet comprising at least three components, which are individually associated with purification and filtration. Cellulose or polypropylene fibers serve as the base of the depth filter and provide a fibrous network with a characteristic pore-size range that enables filtration of particulates based on size as the liquid feed follows a tortuous path through the filter. The most abundant component of a depth filter by mass, the filter aid, contributes to capture of particulates (Buyel et al., 2015) and thereby increases the throughput of the depth filter. Common filter aids are siliceous materials such as diatomaceous earth (DE), fossilized diatoms that have naturally-occurring pore structures, and perlite, a glassy volcanic rock. These filter aids have had utility in water filtration applications (Farrah et al., 1991; Kalyani et al., 2005). The final component of a depth filter is a polymeric binder with some degree of cationic charge. The filter aid serves to retain impurities and improve the throughput of the depth filter (Buyel et al., 2015) while the polymeric resin binder binds the components together and imparts ion-exchange-like adsorptive capacity (Liu et al., 2010). Despite the composite nature of the depth filter, which can give rise to various mechanisms for impurity removal, its pore-size distribution is

often the only criterion for selection. Chapters 2 and 3 of this work characterize the structural and functional properties of depth filters and evaluate their adsorptive capacity for proteins and mechanisms of DNA retention.

Depth filters are also routinely used for additional necessary clarification post-protein A chromatography (Chollangi et al., 2015a). Due to the high affinity with which mAbs bind on a protein A resin, a denaturing condition is required for protein retrieval, such as elution by a low-pH buffer. This pH reduction often leads to degradation, aggregation, and/or precipitation of the product, which may be exacerbated by the presence of contaminants such as host-cell proteins and DNA (Chollangi et al., 2015b). Depth filtration has been shown to be particularly useful in removing host-cell proteins and DNA, leading to less precipitation further downstream. Therefore, informed selection and sizing of the depth filter is important not only for its performance but for also for the performance of the succeeding operations. While over-sizing raises costs, under-sizing can lead to blockage of the depth filter and fouling of the succeeding protein A column (Goldrick et al., 2017). Investigation of the depth filter composition, structure, and capacity for insoluble particulates and soluble impurities is critical for accurate sizing of the depth filter.

1.3 Ion-exchange chromatography (IEX)

Ion-exchange resins rely upon reversible adsorption driven by ionic interactions to capture moieties such as small ionic molecules, oligonucleotides, peptides, or proteins such as monoclonal antibodies. Cation-exchange resins contain anionic ligands such as sulfopropyl or carboxymethyl groups immobilized onto matrices typically prepared from natural or synthetic polymers. Since adsorption is a surface phenomenon, these resin matrices are fabricated as porous beads to present a

large surface-area-to-volume ratio while maintaining a pore size practical for solute transport. Additionally, some commercial resins such as Fractogel (Merck KGaA) are functionalized with polymer chains containing desired ionic groups. These polymer-grafted resins allow the solute to adsorb beyond monolayer coverage on the base matrix by protein infiltration into the polymer layer (Müller, 2005; Yao and Lenhoff, 2006). Although the polymer chains impart additional surface area for solute adsorption, their exclusion of larger proteins from small "pores" that form within or between the polymer chains (Bhambure et al., 2017; Hardin et al., 2009; Thomas et al., 2013) has been reported.

Given that proteins are large, anisotropic macromolecules whose function depends on their structure, their chromatographic separation poses exclusion, stability, and mass-transfer challenges. Apart from the potential exclusion of proteins, the introduction of additional interfacial region through polymer functionalization may result in a mAb-specific increase in surface-mediated conformational changes (Guo and Carta, 2015; Voitl et al., 2010) and self-association (Bethea et al., 2012; Esfandiary et al., 2013; Liu et al., 2005; Luo et al., 2014; Nishi et al., 2010) in the local high effective concentration in the adsorbed state. Furthermore, mass-transfer limitations in the operation of the separation in column mode may significantly lower resin utilization. While the equilibrium or static binding capacities (SBC) of IEX resins are typically on the order of 100 mg of protein per mL of resin, the amount of protein that can bind to the column under realistic operating conditions without incurring unnecessary losses is usually lower due to transport limitations arising from operation in column mode. This smaller capacity is termed the dynamic binding capacity (DBC). Since chromatography is the primary means of industrial protein

purification, understanding and tackling the challenges associated with protein separation is relevant to the biopharmaceutical industry. Chapters 4, 5 and 6 of this work present novel approaches to improving the utilization of and obtaining effective separation using cation-exchange chromatography.

Apart from the binding capacity, the rates of protein transport can influence the performance of a chromatographic operation more broadly. The transport processes in chromatography include convection, axial dispersion, mass transfer from the liquid phase to the resin particle, and diffusion within the particle (Schmidt-Traub, 2005). While extraparticle protein transport is usually not limiting, intraparticle transport limitations are usually dominant. The intraparticle diffusion can occur in the pore space (pore diffusion) or on the adsorbent surface (surface diffusion). Surface diffusion contributes to intraparticle solute diffusion in cases of gas-solid and liquid-solid adsorption (Choi et al., 2001; Medved' and Černý, 2011; Yoshida et al., 1994). In the area of chromatography, surface diffusion has been invoked in many studies involving reverse-phase liquid chromatography (RPLC) (Gritti and Guiochon, 2011; Gritti and Guiochon, 2014; Miyabe and Guiochon, 2010; Rybka et al., 2015; Rybka et al., 2017). Given that proteins are larger, less rigid, multivalent macromolecules with higher adsorption energies, surface diffusivities of proteins would be expected to be small and difficult to measure. Therefore, the importance of surface diffusion of proteins in chromatography has been debated. Chapter 4 of this work shows that protein diffusion on a charged surface can contribute substantially to the overall transport rate of proteins through the tortuous channels within a porous chromatographic resin particle, and demonstrates how surface diffusion can be leveraged to improve the DBC.

1.3.1 Emerging fronts in preparative chromatography

Antibody-based treatments are clinically ideal for difficult-to-treat diseases, including oncological and hematological ones, which account for 40% of all mAb indications approved (Hernandez et al., 2018). Faster and more efficient therapeutic mAb production processes would aid in addressing the doubling in the average cost of cancer treatment in the last decade and the predicted rise in new cancer cases per year to 23.6 million by 2030 (National institute of Health, 2018). Given that purification may account for up to 80% of the mAb production cost (Walsh, 2010), more efficient purification processes are desired.

The performance of chromatographic separations depends on numerous parameters, including the protein, resin, column dimensions, buffer conditions, and temperature. The large number of parameters calls for optimization of each mAb product/resin combination, which can be labor-, capital- and time-intensive. To this end, chromatography modeling can expedite process development with or without providing some level of mechanistic understanding of the process. Design of experiments is a form of empirical model, which can guide process development without informing the underlying mechanisms. In contrast, mechanistic models can inform the adsorption and mass transfer occurring in the column, within the scope of the defined model. Certain simplifying assumptions and empirical parameters are often incorporated into these mechanistic models (Kumar et al., 2015). Several careful experiments are also necessary initially to calibrate the model, requiring some effort upfront. Despite these conditions, mechanistic models are more robust and accurately predictive of chromatographic operation. Apart from the purification of mAbs, the utility of mechanistic models will extend to the effective separation of emerging biologics, including recombinant proteins, peptides, virus-like particles, exosomes,

and cell therapeutics (Zobel-Roos et al., 2019). Chapters 4 and 5 of this work employ mechanistic modeling to aid in optimizing the operating conditions to improve the purity and yield of chromatographic separations.

Mechanistic model-based control strategies are also necessary in transforming currently batch (Hernandez, 2015) unit operations to a continuous and automated process (Zobel-Roos et al., 2019). The current transition from one unit operation to another often involves offline sample adjustment, holding, or sanitization steps, which are time- and labor-intensive. Furthermore, the operation of bind-and-elute chromatography in a single large column limits resin utilization due to the dynamics of protein uptake (Ulmer et al., 2019). Continuous chromatography addresses these challenges through the systematic use of multiple smaller columns, effectively reducing resin and buffer consumption along with the footprint of the purification suite. The increased resin utilization, along with the decreased protein residence time on smaller columns, increases productivity (Somasundaram et al., 2018). The continuous transition from one column to another also reduces labor costs and provides consistent products. Continuous chromatography is particularly suited for the purification of degradation-prone proteins as it streamlines downstream purification (Somasundaram et al., 2018). Chapters 5 and 6 of this work employ a multi-column displacement chromatography set-up, which can be adapted to be continuous, for the separation and removal of various impurities.

1.4 Outline of the dissertation

The adsorptive performance of separation operations such as depth filtration and ion-exchange chromatography depends largely on the ease with which proteins arrive at the site of adsorption and the availability of adsorption sites. This work

demonstrates that the interaction potential between the protein and the adsorbent surface influences both aspects. Studies of depth filtration in chapters 2 and 3 demonstrate that the affinity between the protein and the resin binder of the depth filter dictates the adsorptive capacity of the depth filter. When adsorption is weak, however, as is the case for DNA, the adsorbate can continue to migrate through the filter. This relation between binding affinity and transport is systematized in chapter 4 and modulated to obtain efficient protein penetration into an ion-exchange adsorbent, yielding an unparalleled dynamic capacity. Finally, the relative affinity of different proteins to the adsorbent surface is leveraged in chapters 5 and 6 to obtain efficient separation of similar or distinct groups of proteins. The implications of the adsorbent/adsorbate interaction for the protein capacity, separation efficiency, and protein mass transfer are carefully evaluated by characterization of the adsorbent with and without the adsorbate using microscopy, spectroscopy, and modeling techniques.

In chapter 2, the protein adsorptive capacity of a depth filter is decoupled by characterizing each depth filter component and evaluating its adsorptive capacity for protein. These capacities correlate to bulk measured properties such as surface area, morphology, surface charge density, and composition. The role of each depth filter component in the adsorption of proteins with different net charges was evaluated using confocal fluorescence microscopy.

The retention of DNA on depth filters is evaluated in Chapter 3. The mechanisms by which double-stranded DNA (dsDNA) is retained on depth filter media was probed by visualizing the distribution of fluorescently-labeled retained DNA on spent depth filter discs using confocal fluorescence microscopy. In addition, to elucidate the role of the size of the DNA in its form as an impurity and whether it

may break through into the filtrate, DNA in dividing CHO cells was labeled using 5-ethynyl-2'-deoxyuridine (EdU) before its retention profile was visualized on the depth filter.

With regard to ion-exchange chromatography, chapter 4 provides complementary evidence supporting the role of surface diffusion in protein transport into IEX media. The surface diffusivity, estimated using mechanistic modeling, is shown to depend explicitly on adsorption affinity. Different surface diffusivities give rise to different protein distributions within the resin, as characterized using confocal microscopy and small-angle neutron scattering (length scales of μm and nm respectively). Exploiting this relationship, an innovative procedure for loading protein onto a column, which dramatically increases the column productivity, is presented.

In chapters 5 and 6, the competitive adsorption among proteins is leveraged for their efficient separation. Case studies for removal of mAb charge variants are presented in chapter 5, while those for HCP and aggregates are presented in chapter 6. Run conditions were optimized using modeling. These two chapters present configurations for multi-column continuous systems to consecutively displace the more weakly-binding components and hence achieve some separation during product loading. The method presented enables higher resin utilization while delivering improved separation and efficiency, compared to relying solely on the bind-and-elute mode of chromatography.

Chapter 2

CONTRIBUTIONS OF DEPTH FILTER COMPONENTS TO PROTEIN ADSORPTION

2.1 Introduction

Depth filters are near-ubiquitous in the processing of biotechnology products such as therapeutic proteins. Disposable, low-cost depth filters are often used to complement centrifugation by removing particles that are too small to sediment given practical relative centrifugal forces (Iammarino et al., 2007). In addition, depth filtration can replace centrifugation in some small-scale operations or in some cases of low cell density (Low et al., 2007). In the context of production of monoclonal antibodies, the utility of depth filters extends beyond harvest clarification to clarification of turbidity often seen during the neutralization of the protein A eluate (Chollangi et al., 2015a). Of particular interest for the present work is that depth filtration has been shown to improve clearance of host-cell proteins by adsorption, in addition to the more explicitly stated filtration function (Yigzaw et al., 2006b).

Depth filters comprise a cellulose base, a type of siliceous filter aid, and a polymeric resin binder with some level of cationic charge resulting from primary to quaternary amine functional groups (3M, 2013). For example, two particular grades of depth filters from 3M, Zeta Plus ZA and Zeta Plus SP, are specified to have strong anion-exchange and weak-anion exchange properties, respectively (3M, 2013). Presumably due to differences in the pK_a values of chemical functionalities in the binder, the Zeta Plus ZA and SP grades are advertised to have different charge

dependence on pH (3M, 2013). The binder chemistry is, however, often a trade secret and depth filters may contain additional charged polymers to augment the retention of charged species (Knight and Ostreicher, 1998).

The multiple components comprising a depth filter impart to it additional functionality beyond simply that of particulate filtration, as a result of which the overall performance characteristics may be difficult to decouple. In addition to retaining particulates on its surface and along the tortuous path (Van Holten and Autenrieth, 2003; Maschio and Arruda, 2000), depth filters have been shown to adsorb solubilized proteins (Schreffler et al., 2015; Singh et al., 2017; Yigzaw et al., 2006b). Electrostatic attraction between the proteins and the charged polymeric binder, as well as hydrophobic interaction, have been examined as relevant retention mechanisms (Charlton et al., 1999; Yigzaw et al., 2006b). For instance, the removal of colloidal impurities such as endotoxin from water (Gerba and Hou, 1985) and DNA from buffered solutions (Dorsey et al., 1997) was correlated with the degree to which the depth filters were charged. However, the complex mixtures with which depth filters are challenged in bioprocessing, even with partially purified streams such as Protein A eluate in monoclonal antibody purification (Schreffler et al., 2015; Yigzaw et al., 2006b), make protein clearance data more difficult to interpret.

Although the existing body of work has demonstrated that depth filters can remove solubilized impurities, a more systematic understanding of the depth filter components and their affinity for protein can inform their adsorptive capacity. Here we characterize the depth filter and some of its components and use those findings to inform the affinity and capacity of the depth filter for proteins. In addition, protein-adsorbed depth filters were visualized, and the spatial distribution of the adsorbed

proteins was used to obtain additional insights into the depth filters' structure and charge capacity.

2.2 Materials and methods

2.2.1 Materials

Monobasic sodium phosphate (NaH_2PO_4), sodium phosphate dibasic (Na_2HPO_4), sodium bicarbonate (NaHCO_3), sodium acetate ($\text{C}_2\text{H}_3\text{NaO}_2$), acetic acid ($\text{CH}_3\text{CO}_2\text{H}$), sodium chloride (NaCl), anhydrous DMSO, NHS-rhodamine and Alexa Fluor™ 647 NHS ester were all purchased from Fisher Scientific (Fair Lawn, NJ).

Celpure 100 was purchased from Sigma-Aldrich (St. Louis, MO) while Celite and perlite were obtained from 3M (Maplewood, MN). 3M also provided samples (discs) of 90ZB and 60SP media, hydrated cellulose fibers used in these media discs, and 25 cm² 90ZB05A Zeta Plus capsule filters. Celite serves as the filter aid in the 90ZB depth filter whereas the filter aid in the 60SP depth filter is a combination of Celite and perlite. The polymeric binders contain some level of cationic charge from primary to quaternary amine functional groups. Compositional data for the specific filters used are not available, but the approximate ranges of 20-40, 60-80 and 1-4 wt % for cellulose, filter aid and the binder, respectively (Woo et al., 2015) were used for data analysis via the midpoint values of 30 wt % for cellulose and 70 wt % for filter aid.

Human serum albumin, lysozyme from hen egg white, β -lactoglobulin from bovine milk and catalase from bovine liver were purchased from Sigma-Aldrich and recombinant human lactoferrin from rice was purchased from Lee Biosolutions (Maryland Heights, MO). These proteins were dissolved in desired buffers and buffer-

exchanged as necessary using appropriate molecular weight cut-off Amicon centrifugal filters (MilliporeSigma, Burlington, MA) or a Sephadex G-25 (GE Healthcare, Chicago, Illinois) desalting column (2 cm i.d. x 22 cm long) on an Äkta Purifier (GE Healthcare). The resulting protein solutions were then filtered using 0.2 µm polyvinylidene difluoride filters. Fc-fusion protein A and mAbs B, C and D were provided by Bristol-Myers Squibb (Devens, MA) as unformulated drug substance at 20–60 mg/mL and were stored at –80 °C for up to 1-3 months prior to the experiments. Stock protein solutions of 10–20 mg/mL were prepared and characterized using ultraviolet (UV) absorbance at 280 nm using a NanoDrop 2000 (Thermo Scientific, Waltham, MA).

2.2.2 Filter aid and depth filter characterization

2.2.2.1 Wavelength dispersive X-ray fluorescence spectroscopy (WDXRF)

The relative elemental compositions, from fluorine to uranium, of the filter aids were determined using a Rigaku Supermini200 wavelength dispersive X-ray fluorescence spectrophotometer (Tokyo, Japan). No light elements (hydrogen – oxygen) are reported because the likelihood of characteristic X-ray emission decreases with decreasing electron binding energy of the vacant shell and elements with a smaller atomic number have lower energies associated with their valance shells (Ellis, 1953). Measurements were taken in qualitative scan mode for comparison among the three different filter aids.

2.2.2.2 Scanning electron microscopy (SEM)

Filter aids and depth filters were prepared for SEM imaging following two nights of freeze-drying. Filter aids were mounted on aluminum stubs using double-sided carbon tabs and sputter-coated with a 3 nm thick layer of palladium. Depth filter pieces of approximately 5 mm x 5 mm were also mounted on aluminum stubs using double-sided carbon tabs and sputter-coated with a 5–6 nm thick layer of palladium. Conductive carbon paint was applied to the sides of the depth filter pieces to address possible poor coating with palladium. Samples were visualized using a Hitachi S4700 field emission scanning electron microscope (Tokyo, Japan) at 3 kV.

2.2.2.3 Nitrogen sorption

Celpure 100, Celite and perlite were freeze-dried for 48 hours prior to the gas adsorption measurement to remove moisture. Once the samples had been dried, N₂ adsorption and desorption isotherms were collected using 0.5–1 g of filter aid on a Micromeritics Accelerated Surface Area and Porosimetry System 2020 (Norcross, GA). The specific surface area was found by fitting adsorption isotherm data up to a relative pressure of 0.2–0.3 to the linearized Brunauer, Emmett and Teller equation (Kim et al., 2013); coefficients of determination greater than 0.99 were achieved. The surface areas of 90ZB and 60SP depth filters and their respective cellulose fibers were also determined following the aforementioned procedure on 0.8–1 g of filter media.

2.2.2.4 ζ potential

Filter aids were suspended in unbuffered 10 mM NaCl solution at 25 mg/mL and centrifuged. The supernatant was removed and the filter aids were washed by suspension, vortexing and centrifugation twice more using 10 mM NaCl solution. The filter aids were then resuspended at 25 mg/mL in 10 mM NaCl and were divided into four parts of equal volume and titrated using 1 M HCl or 1 M NaOH to target pH values of 2, 4, 6 and 10, thereby spanning a pH range of 2-10. The actual final pH values were 1.95, 4.06, 5.30 and 9.80 for Celite and 2.00, 4.28, 6.60 and 9.10 for perlite. The filter aid suspensions were set aside for 15–20 minutes to allow large particles to settle prior to electrophoretic mobility measurements on a Möbiu ζ from Wyatt (Santa Barbara, CA). Measurements were made for each sample by switching electrode polarities at 10 Hz at a constant voltage of 3.5 V. Nine to ten measurements were made for each sample over collection periods of 20 s each. The ζ potential was inferred from the electrophoretic mobility in the limit of the Smoluchowski approximation (Matijević, 1979).

2.2.2.5 Filter aid titration

Suspensions containing 3–4 g of filter aid, corresponding to minimum total surface areas of 7 m² as determined by the N₂ sorption measurements, were prepared in 10 mM NaCl solutions. The filter aids were washed three times by suspension, vortexing and centrifugation with 10 mM NaCl and resuspended in the same solution and allowed to equilibrate overnight with gentle end-over-end rotation. After equilibration, 50 mL of each suspension at 60–75 mg/mL were titrated in a 100 mL beaker agitated at 400 rpm by an axial flow impeller with a blade radius of 1 cm. The suspension was sparged with nitrogen prior to titration to remove CO₂.

The suspension was titrated to lower and higher pH values using equivalent volumes of 1 M HCl and 1 M NaOH, respectively. The pH of the suspension was recorded via a probe placed in the beaker directly above the impeller. The starting solution of 10 mM NaCl was also titrated to lower and higher pH values using equivalent volumes of titrant to serve as a blank following the aforementioned procedure. The relative surface charge densities were determined by dividing the number of moles of potential-determining ions on the surface by the total available surface area (Lützenkirchen et al., 2012).

2.2.3 Protein batch adsorption experiments

2.2.3.1 Protein adsorption on filter aids

A series of protein dilutions from 0.2–1.2 mg/mL were prepared in 1.6 mL Eppendorf tubes containing 20 mg of filter aid suspended in the same buffer in which protein solutions were prepared. Samples were allowed to rotate end-over-end overnight at room temperature (22±2 °C), after which no appreciable further depletion of the supernatant protein was seen. The total protein depletion for the last data points of the isotherms was less than 50%, indicating that the plateau values are meaningful indicators of saturation. After equilibration, samples were centrifuged for 3 min at 3000 g to pellet the filter aid. The filter aid surface coverage by the adsorbed protein Γ (mg/m²) was determined by mass balance

$$\Gamma = \frac{V(C_0 - C)}{m_s a_s} \quad (2.1)$$

where V (mL) is the solution volume, m_s (mg) is the filter aid mass, a_s (m²/mg) is the filter aid specific surface area and C_0 (mg/mL) and C (mg/mL) are the initial and final protein concentrations, respectively, as measured by absorbance at 280 nm.

2.2.3.2 Protein adsorption on cellulose fibers

Pieces of cellulose fibers of mass 13.5–15 mg were pulled apart and suspended in a series of solutions containing 0.1–1.2 mg/mL protein in 10 mM sodium phosphate buffer at pH 8 in 1.6 mL Eppendorf tubes. Samples were equilibrated by end-over-end rotation and the supernatant protein concentrations were measured after 94 hours. An equilibration time of ~ 4 days was provided to ensure that the protein had sufficient time to diffuse into the various cellulose structures involved. After equilibration, samples were centrifuged for 3 min at 3000 g to clarify the supernatant. The cellulose surface coverage by the adsorbed protein Γ (mg/m²) was determined by mass balance following eqn. (1).

2.2.3.3 Protein adsorption on depth filters

Using single-edge cutter blades, 90ZB and 60SP depth filters (3–4 mm thick) were cut into rectangular pieces approximately 7–9 mm by 9–11 mm that weighed 90–130 mg for 90ZB and 110–150 mg for 60SP. A series of protein dilutions from 0.2–2 mg/mL in 10 mM sodium phosphate buffer at pH 8 was prepared in 2 mL Eppendorf tubes containing the depth filter pieces. Samples were equilibrated by end-over-end rotation for the first 24 hours at 22±2 °C, followed by incubation at 4 °C for an additional 264 hours to provide sufficient time for proteins to diffuse into the 3–4 mm thick media. After equilibration, samples were centrifuged for 3 min at 3000 g to clarify the supernatant, after which the supernatant protein concentrations were measured. The depth filter surface coverage by the adsorbed protein Γ (mg/m²) was determined by mass balance following eqn. (1).

2.2.4 Protein adsorption on Zeta Plus-BC25 capsule filters

Frontal adsorption (breakthrough) measurements were performed by passing stock solutions of mAbs B, C and D at 0.8–1.2 mg/mL in 20 mM sodium acetate buffer at pH 5.5 through 25 cm² 90ZB05A depth filter pods (3M, Maplewood, MN) at 12 L/m².hr using an Äkta Explorer chromatographic workstation. The absorbance at 280 nm was measured using the Äkta UV-900 detector and the corresponding protein concentration was normalized to the stock concentration measured using a NanoDrop 2000. The binding capacity was determined by subtracting the protein mass in solution in the holdup volume from the total mass of protein fed. The holdup volume was determined by injecting 1% acetone, with detection following the same method as in the protein runs.

2.2.5 Visualization of protein-adsorbed depth filters

2.2.5.1 Protein labeling

Lysozyme was fluorescently labeled via primary amine groups using NHS-Rhodamine (ThermoFisher Scientific). NHS-Rhodamine was chosen over sulfonated cyanine dyes, which can impart a significant negative charge to the labeled protein, to minimize the perturbation to the charge distribution on lysozyme post-labeling at pH 8. Lysozyme was labeled following the manufacturer's protocol with some modifications. NHS-Rhodamine was dissolved in DMSO at 10 mg/mL and was added to 1 mL of a 10 mg/mL lysozyme solution in 100 mM sodium phosphate, 150 mM sodium chloride (pH 7.4), at a molar ratio of 0.5:1 dye to protein. Conjugation was performed at a low dye-to-protein molar ratio to minimize the occurrence of lysozyme molecules being labeled with more than one dye molecule, so that the charge state of lysozyme would be changed minimally. The mass shift of lysozyme post-conjugation

was confirmed by LC-MS (Xevo G2-S QToF, Waters), based on assuming equal ionization efficiency between the unlabeled and labeled protein; over 97% of the protein was found to be unlabeled or labeled in a 1:1 stoichiometric ratio. The assumption of equal ionization efficiency of the unlabeled and labeled protein is plausible given that the label constitutes only a small fraction of the labeled protein molecule.

Alexa Fluor™ 647 NHS Ester (ThermoFisher Scientific) was used to label the primary amine groups in β -lactoglobulin following the manufacturer's protocol; the additional negative charge introduced by labeling was assumed not appreciably to affect the adsorption behavior of the already negatively-charged protein. Assuming all residues within β -lactoglobulin have the pK_a values of the isolated residues, the estimated charge of ~ -10 would be altered to -14 in the event of 1:1 dye to protein conjugation. The conjugates were buffer-exchanged and the free dye in solution was removed using a Sephadex G-25 (GE Healthcare) desalting column. After purification, the molar labeling ratios of 1.5–2 mg/mL stock solutions of the labeled proteins were determined following the manufacturers' protocols to be 44%.

2.2.5.2 Protein adsorption for confocal microscopy

Batch adsorption experiments were carried out in 1.6 mL Eppendorf tubes containing 80–100 mg depth filter media and 1 mL of 6% labeled protein at 1 mg/mL. Equal concentrations of each protein were used for the binary protein samples to give a sample volume of 1 mL and 0.5 mg/mL each of 6% labeled lysozyme and β -lactoglobulin. Each suspension was allowed to equilibrate by end-over-end rotation for 24 hours and then the sample was placed in a Nunc chamber (ThermoFisher) and weighed down with a glass block. The sample was visualized on an inverted Zeiss 710

confocal microscope (Oberkochen, Germany) using a Zeiss 40× C-Apochromat (water/1.2 NA) Korr M27 objective. The laser intensity, gain and pinhole were kept constant in visualizing the same protein on different filters for each experiment to allow comparison of intensities. The depth probed along the z-axis was also kept similar ($\pm 2 \mu\text{m}$) to ensure that the densities of collapsed visualizations were comparable.

2.3 Results and discussion

2.3.1 Filter aid characterization

Three filter aids were characterized in terms of their elemental analysis, morphology, specific surface area (SSA), surface charge density and ζ potential. The filter aids evaluated were two grades of diatomaceous earth (DE), Celpure 100 and Celite, along with perlite. As shown in Table 2.1, Celpure 100 was found to be the most siliceous, followed by Celite and perlite. The two grades of DE comprise primarily Si while perlite contains over 10 mass % of K and Al. Perlite also differs morphologically from DE, as shown by the SEM images in Figure 2.1. Heterogeneous distributions of diatom species confer varying pore structures and morphologies to Celpure 100 (Figure 2.1A, B) and Celite (Figure 2.1C, D). Additionally, Celite has a larger population of smaller particles than Celpure 100. Perlite (Figure 2.1E, F), on the other hand, appears smooth. All three filter aids appear from the images to have a broad particle size distribution. These differences in elemental composition and physical structure of the filter aids may result in different surface areas and surface chemistries and these may influence the adsorptive functionality of the filter aids.

Table 2.1 Elemental compositions of the filter aids compared in terms of their relative mass percentages. Elements lighter than fluorine are not detected.

Element	Celite (wt%)	Celpure 100 (wt%)	Perlite (wt%)
Si	89.4	95.3	67.5
K	2.2	0.8	15.4
Al	3.2	1.1	10.6
Na	< 0.5	< 0.5	2.8
Fe	3.5	2.0	1.8
Ca	< 0.5	< 0.5	1.4
Mn	< 0.5	< 0.5	< 0.5

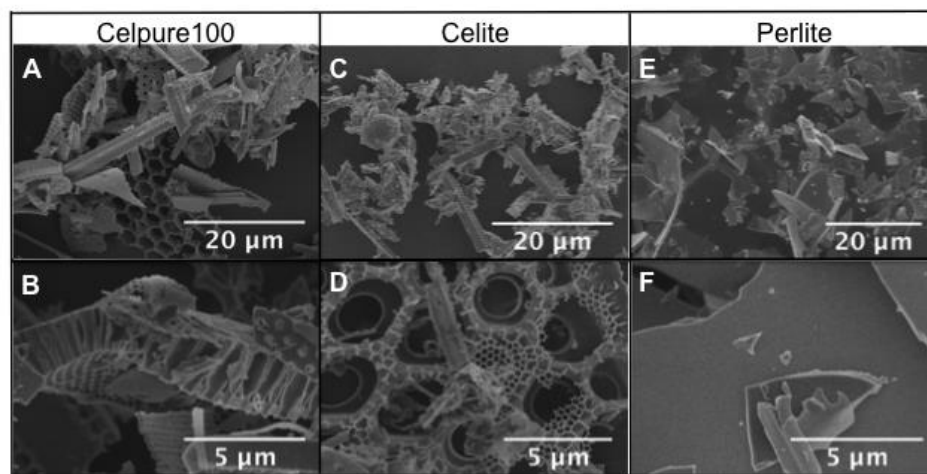


Figure 2.1 SEM images of dry filter-aid powders. Celpure 100 (A, B), Celite (C, D) and perlite (E, F). Note the difference in magnification between the top and the bottom rows.

Figure 2.2 shows the N₂ adsorption isotherms on the different filter aids. The observed isotherm shapes, resemble Type I & II forms, and the absence of significant hysteresis are typical for microporous (> 2 nm pore diameter), non-porous, or macroporous (> 50 nm pore diameter) materials, with the plateau values corresponding to micropore capacity or monolayer coverage (Alothman, 2012; Brunauer et al., 1940; Storck et al., 1998). The SSAs were determined by fitting the isotherms in the range of low relative pressures to the linearized BET equation (Rouquerol et al., 2007). As shown in the inset of Figure 2.2, the data fit the equation well and lead to the SSAs listed in Table 2.2. As expected, the porous filter aids had larger SSAs than the non-porous perlite. Celite has a larger SSA than Celpure 100, which may correlates with the larger population of small particles seen in Celite via SEM (Figure 2.1). All the filter aid SSAs in Table 2.2 are 2 to 3 orders of magnitude smaller than the range 300–1500 m²/g typical of microporous materials (Budd et al., 2004), which supports the designation of the filter aids as macroporous or non-porous. This pore character would readily allow access by proteins under conditions favorable for adsorption.

Table 2.2 BET surface areas of the filter aids, cellulose materials and the depth filters along with their 95% confidence intervals.

Sample	BET surface area (m ² /g): 95% CI
Celpure 100	6.93 ± 0.03
Celite	8.14 ± 0.04
Perlite	2.12 ± 0.2
Cellulose: 60SP	4.11 ± 0.01
Cellulose: 90ZB	4.51 ± 0.01
60SP	4.86 ± 0.03
90ZB	6.67 ± 0.03

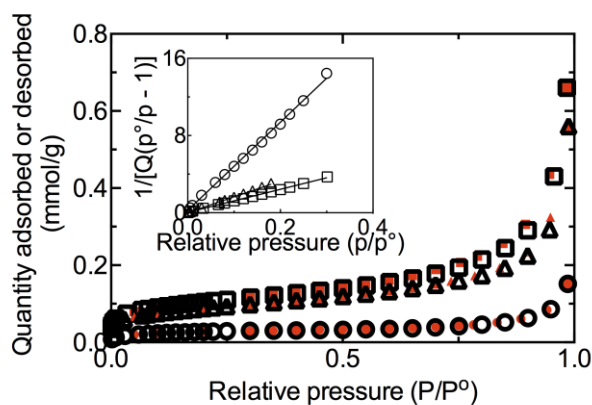


Figure 2.2 Isotherms for N₂ adsorption (open symbols) and desorption (filled symbols) onto Celite (□), perlite (○), and Celpure 100 (△). The inset shows the fits to the linear BET equation.

In addition to the SSA available for adsorption, the relative surface charge densities of the filter aids were also compared to aid in interpreting protein adsorption. The surface charge densities presented in Figure 2.3A are relative to the value at the starting pH at which the filter aids were equilibrated in a low-salt solution. Therefore

the pH values corresponding to 0 C/m^2 are not the absolute points of zero charge (PZCs). Although the PZC values of the siliceous filter aids are likely around pH 2 (Bergna and Roberts, 2005; Yoon and Lueptow, 2006), the ζ potential of a subset of particles that remained suspended in solution was determined by electrophoretic light scattering for confirmation. Figure 2.3B confirms that the filter aids have a PZC of less than 2, thus are negatively-charged for the entire range of pH relevant to purification.

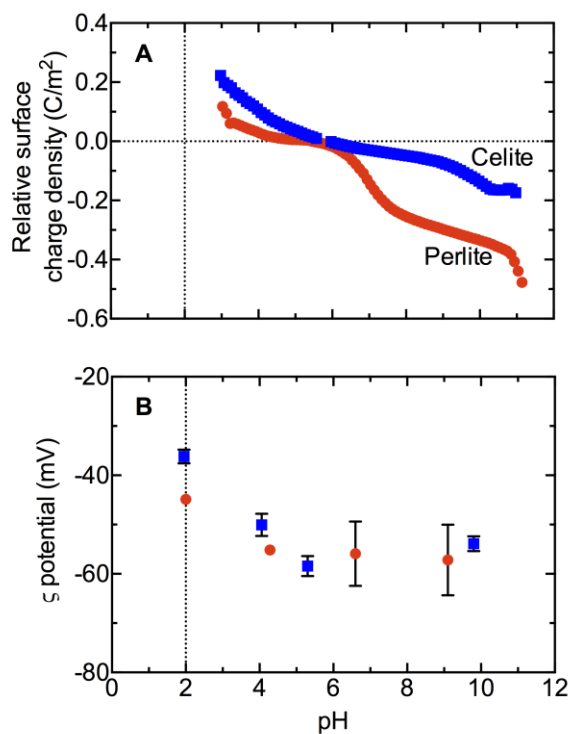


Figure 2.3 (A) Relative surface charge density and (B) ζ potential of Celite (blue) and perlite (red). The vertical line in A denotes the pH at which titration began. The vertical line in B indicates pH 2, which exceeds the PZC values of the filter aids.

2.3.2 Protein adsorption on filter aids

Figure 2.4A shows adsorption isotherms for catalase, lysozyme and albumin on Celite in 10 mM sodium phosphate at pH 8. Lysozyme adsorption shows a relatively steep initial slope and attains a well-defined plateau at about 2 mg/m² while albumin does not exceed a relatively low coverage value. Catalase rises to a higher coverage than does lysozyme, but with a lower slope and hence lower affinity.

The isoelectric points (pI) of lysozyme, catalase and albumin, as reported by the vendor based on published measurements, are 11.4, 5.4 and 4.7, respectively and their molar masses are 14.3, 250 and 66.4 kDa, respectively. Based on the protein pI values, lysozyme has a net positive charge and catalase and albumin have net negative charges at pH 8, while the ζ potential measurements (Figure 2.3B) indicate that Celite is negatively-charged at pH 8. Therefore the high adsorption affinity for lysozyme and the lower affinities for catalase and albumin appear to reflect electrostatically-driven adsorption, akin to that on a cation exchanger. That catalase and albumin adsorb at all is presumably due to the heterogeneous charge distribution on proteins as well as possible contributions of other forms of interaction, including van der Waals, hydrophobic interactions and hydrogen bonding (Asthagiri and Lenhoff, 1997; Kopaciewicz et al., 1983; Lesins and Ruckenstein, 1988). Conformational changes may also play a role (Kondo et al., 1991).

That the coverage of catalase exceeds that of lysozyme in Figure 2.4A is attributable to the larger size of catalase; the molecular weight ratio corresponds to an effective radius ratio of about 2.6. An absolute frame of reference for the surface coverage values is provided by monolayer coverage, which can be estimated by assuming hexagonal close packing of uniform spheres on a surface (Chang and Lenhoff, 1998; Guzman et al., 1986; Yang et al., 2002; Yao and Lenhoff, 2006). For

lysozyme the estimated maximum coverage exceeds 2 mg/m^2 , which is consistent with measurements by various methods of lysozyme adsorption on flat surfaces (Arai and Norde, 1990; Guzman et al., 1986; Shibata and Lenhoff, 1992) as well as with the plateau value shown in Figure 2.4A.

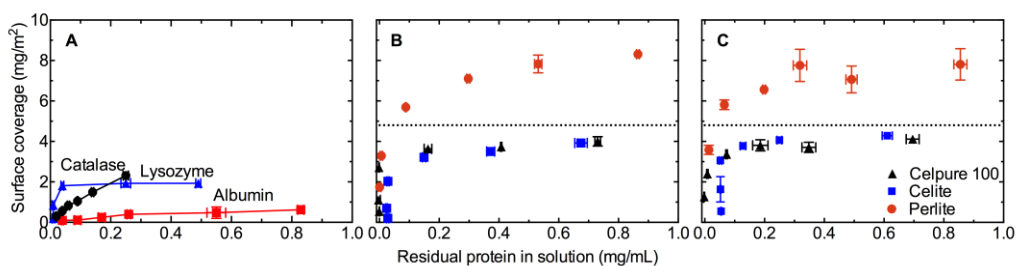


Figure 2.4 Isotherms for adsorption of catalase, lysozyme and albumin onto Celite (A) in 10 mM phosphate buffer at pH 8, and isotherms for adsorption of lactoferrin (B) and Fc-fusion protein A (C) onto the filter aids in 10 mM phosphate buffer, pH 8, and 10 mM citrate buffer, pH 5, respectively. The black dashed lines show hexagonal close packing limit of the respective proteins.

Figures 2.4B and C compare adsorption isotherms for lactoferrin and an Fc-fusion protein on the different filter aids. Both proteins (pI 8.7 and 5.9 respectively) should be net positively-charged under the conditions studied (pH 8 and 5 respectively). The calculated coverages on the two DE materials are very similar but those on perlite, which has a lower SSA, are noticeably higher. Effective radii for lactoferrin and the Fc-fusion protein, both of which have molecular weights $\sim 80 \text{ kDa}$, were calculated using an average protein partial specific volume of $0.73 \text{ cm}^3/\text{g}$ (Creighton, 1985) to be approximately 2.8 nm, leading to estimated monolayer coverage of closely-packed spheres of 4.8 mg/m^2 (dashed lines in Figures 2.4B and C). The lactoferrin and Fc-fusion protein coverages on the two grades of DE are similar to the closely-packed spheres limit, but the coverage on perlite exceeds that

value. The higher coverage on perlite may be due to denser packing due to a different adsorption orientation, since both lactoferrin and the Fc-fusion protein are elongated. For example, approximating lactoferrin as a cylinder with a diameter of 4.7 nm and a length of 10.5 nm (Lu et al., 2005) leads to coverages of 8.7 and 4.6 mg/m² for end-on and side-on adsorption respectively. A preferred orientation may be promoted by perlite's higher relative surface charge density at pH 8 (Figure 2.3A).

2.3.3 Cellulose characterization

Figure 2.5A shows N₂ adsorption isotherms on the two grades of cellulose fibers used in the 90ZB and 60SP depth filter media, with their inferred specific surface areas shown in Table 2.2. The cellulose used in the 90ZB depth filter has a slightly larger SSA than that used in the 60SP filter, but the deviation of less than 10% indicates that the differences are minor.

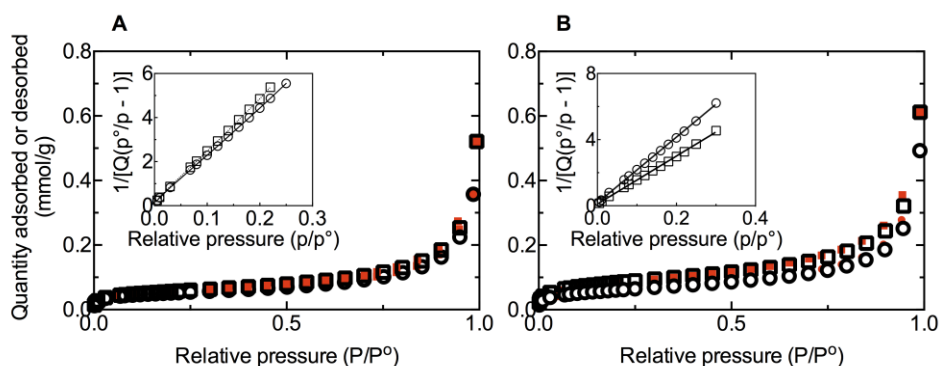


Figure 2.5 Isotherms for N₂ adsorption (open symbols) and desorption (filled symbols) onto (A) the cellulose fibers used in the 90ZB (□) and the 60SP (○) depth filters, and (B) the 90ZB (□) and the 60SP (○) depth filters. The insets show the isotherm data fitted to the linear BET equation.

2.3.4 Protein adsorption on cellulose

Adsorption isotherms of lysozyme and β -lactoglobulin on the cellulose fibers used in the 90ZB and the 60SP depth filter discs are shown in Figure 2.6A. The maximum lysozyme surface coverage was higher than that of β -lactoglobulin, perhaps reflecting negative charge on the cellulose from carboxyl and hydroxyl groups (Stana-Kleinschek and Ribitsch, 1998). The lysozyme coverage is about double the close-packed sphere limit. The higher coverage may be due to the difference in the state of the cellulose fibers during the surface area measurement and the adsorption experiment. At the microscopic level, nitrogen sorption experiments require the sample to be free of moisture, which may allow some pores in the cellulose fibers to collapse during the surface area measurements but re-open to some extent during rehydration and equilibration (Park et al., 2006; Wang et al., 2003). Since the surface coverage is based on the total available surface area measured on the dried cellulose fibers, a reduced surface area would give a deceptively large protein surface coverage. An additional factor, on a more macroscopic scale, is that the cellulose fibers are not shaped or bound in the protein adsorption experiments but are tightly packed into the glass sampling tube to enable measurement of sufficient surface area.

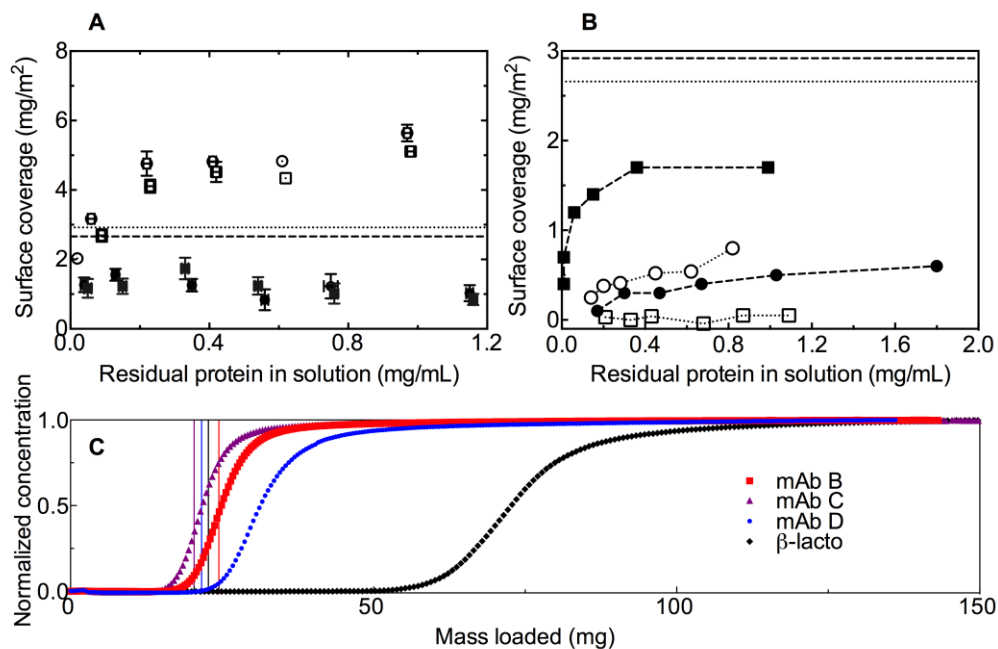


Figure 2.6 (A) Lysozyme (open symbol) and β -lactoglobulin (closed symbol) coverage on the cellulose fibers used in the 90ZB (\square) and 60SP (\circ) depth filters. The close-packed sphere limits for lysozyme and β -lactoglobulin are shown by the dashed and dotted lines, respectively. (B) Lysozyme (open symbol) and β -lactoglobulin (closed symbol) coverage on 90ZB (\square) and 60SP (\circ) depth filters. The close-packed sphere limits for lysozyme and β -lactoglobulin are shown by the dotted and dashed lines, respectively. (C) Breakthrough curves for mAb B, C and D on 25 cm² 90ZB05A capsules using 20 mM sodium acetate at pH 5.5. Color-coordinated lines show the masses corresponding to the hold-up volumes. The adsorbed masses of mAb B, C, D and β -lactoglobulin onto the capsules were 2.05, 3.29, 12.99 and 51.85 mg, respectively.

2.3.5 Depth filter characterization

The N₂ sorption data (Figure 2.5B) and fitted SSAs (Table 2.2) of the two depth filters show the 90ZB depth filter to have a larger SSA than the 60SP filter. The cellulose used in the 90ZB depth filter also has a larger SSA than that used in the 60SP filter, but the difference here is smaller. The filter aid in 60SP is an equimixture of Celite and perlite whereas 90ZB contains only Celite. Calculating the SSA of the

depth filters from approximate mass % values of the cellulose and the filter aid (30% cellulose, 70% filter aids), i.e., excluding the binder, results in values of 7.05 and 4.82 m²/g for the 90ZB and 60SP depth filters, respectively. The value for 60SP is in excellent agreement with the measured surface area whereas for 90ZB the measured surface area is 6% lower. This discrepancy is small considering the nature of the calculation, but it may be due in part to the binder, which may add surface area of its own but may also block some pores in the DE as it coats the depth filter. The filter aids are calculated to provide 70-80% of the total surface area of the depth filter, discounting the presence of the binder, but it is uncertain whether the surface area, especially the internal pore surface, is indeed accessible in the assembled depth filter.

The presence of the binder and the microstructure of the depth filter were probed using SEM in order to seek clarification of the roles of the different components. Figure 2.7 shows the 90ZB filter at various magnifications. While Figure 2.7A provides a general view of the structure, a closer view shows that the filter aids appear packed onto the cellulose fibers (Figure 2.7B). Upon further magnification, webbing of small fibers (Figure 2.7C) on filter aids is seen within certain regions of the depth filter. These fibers are an order of magnitude narrower than most cellulose fibers and therefore appear to be polymeric binder-rich regions. Based on these images, it appears that the polymeric binder coats a significant fraction of the depth filter's surface area.

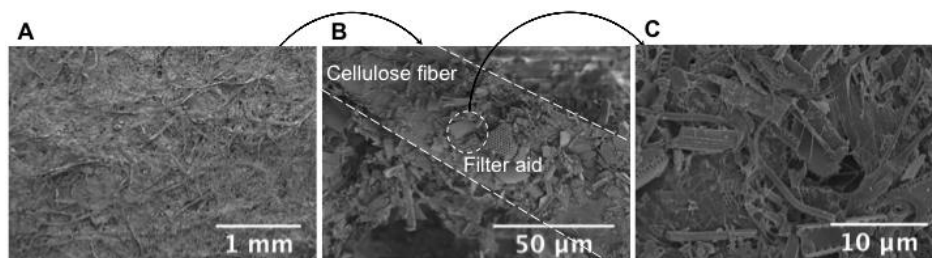


Figure 2.7 SEM images of 90ZB depth filter media at various magnifications. The white dashed line outlines a cellulose fiber whereas the white dashed circle outlines a piece of filter aid. Fibrous webbings on a bed of filter aids are shown in C. Black arrows are to guide the eye.

2.3.6 Protein adsorption on depth filters

The character of the exposed surface area in intact depth filters was investigated by adsorbing a protein with a net positive charge, lysozyme, and one with a net negative charge, β -lactoglobulin, on pieces of the 90ZB and 60SP filters at pH 8 in 10 mM sodium phosphate buffer. Although β -lactoglobulin adsorbed onto both depth filters, the coverage of β -lactoglobulin on the 90ZB filter was higher than that on the 60SP, as shown in Figure 2.6B. Conversely, the coverage of lysozyme on the 90ZB filter was lower than that on the 60SP. If adsorption is driven primarily by electrostatic interactions (Yigzaw et al., 2006b), these results suggest that the 90ZB filter has more positively-charged surface area than the 60SP. The maximum β -lactoglobulin coverage on the 90ZB filter is about 60% of the calculated monolayer coverage based on the simple geometrical argument presented earlier, and the adsorption isotherm is less steep than those of positively-charged proteins on the filter aids (Figure 2.4). This suggests a moderate affinity that is presumably determined largely by the properties of the binder. For the other cases shown in Figure 2.6B, the adsorption affinity and extent are both much weaker. These results may indicate a

greater degree of heterogeneity in the 60SP filter surface vs. comparative homogeneity in the 90ZB filter surface.

In an effort to provide a spatially-resolved interpretation of the observations in Figure 2.6B, the locations of the adsorbed proteins on the depth filter were visualized by confocal microscopy using fluorescently-labeled proteins. As shown in Figure 2.8A, β -lactoglobulin adsorbed widely across the 90ZB filter while it adsorbed less uniformly on the 60SP filter. This may indicate that the binder coats the depth filter more uniformly or more extensively in the 90ZB filter than in the 60SP. Alternatively, the functionalities with the cationic charge may be more prevalent on the surface of the 90ZB compared to the 60SP, which agrees with 3M's specification that the Z grade of depth filter has a higher charge capacity than that of the S grade (3M, 2013). Similar results were obtained from the simultaneous adsorption of lysozyme and β -lactoglobulin onto the depth filters (Figure 2.8B), although competitive adsorption occurs in that situation. The relatively low level of lysozyme adsorption on the 60SP depth filter appears to occur primarily on the cellulose fibers, and there is little indication of significant adsorption on the filter aids. As described previously (Figure 2.6A), more lysozyme than β -lactoglobulin adsorbed onto the uncoated cellulose fibers. These collective findings suggest that the cationic binder found in the 60SP filter may preferentially coat the filter aids over the cellulose fibers, rendering the filter aids largely inaccessible to lysozyme. Alternatively, the binder in the 60SP filter may have some anionic character that contributes to adsorption on the cellulose fibers.

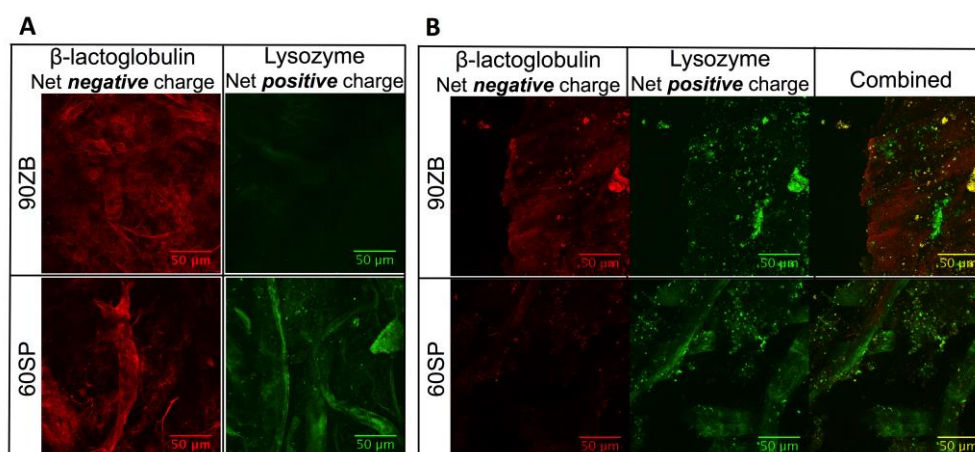


Figure 2.8 Imaging by confocal microscopy of fluorescently-labeled β -lactoglobulin and lysozyme adsorbed individually (A) and simultaneously (B) on 90ZB and 60SP depth filters. The intensities have been enhanced identically in each vertical set for the same protein for ease of comparison of the adsorption of each protein onto the two depth filter media discs. The differences between the red and the green intensities are not to scale.

Apart from the model proteins, the depth filters' adsorptive capacities for pure therapeutic mAbs were explored to provide a functional measure of adsorptive capacity under flow conditions. Capacities were measured using breakthrough experiments on intact 90ZB05A depth filter capsules to provide a realistic adsorption environment with minimization of transport limitations of the kind seen in Figure 2.6B. Figure 2.6C shows the breakthrough curves for the three mAbs evaluated in 10 mM sodium acetate at pH 5.5 along with a breakthrough curve for β -lactoglobulin in 10 mM sodium phosphate at pH 8. The isoelectric points of mAb B, C, D and β -lactoglobulin are 9.2, 8.4, 7.9 and 5.1, respectively. The mass of protein adsorbed onto the capsule for mAb B, C, D and β -lactoglobulin was 2.05, 3.29, 12.99 and 51.85 mg, respectively. The extent of adsorption of the basic mAbs onto the 90ZB filters was generally low. The adsorption results with the two model proteins suggest that the

90ZB filter is primarily cationic and therefore basic mAbs are expected to adsorb to a smaller extent than the primarily acidic host-cell proteins and β -lactoglobulin. However, the adsorptive capacity of the depth filter for mAb D was about three- to sixfold higher than that for mAbs B and C.

The mass of each mAb adsorbed in the flow experiments can be interpreted more effectively by expressing the values in terms of surface area using the relationship of filter dimension to filter mass. Using the mass-weighted specific surface area of $4.86 \text{ m}^2/\text{g}$ for the 90ZB05A capsule comprising an upper layer of 90ZB and a lower layer of 30ZB media discs, protein coverage values of 0.062, 0.10 and $0.40 \text{ mg}/\text{m}^2$ were found for mAb B, C and D, respectively. Since both layers are of ZB grade, differing only in their pore rating, the mAbs' coverage values, derived using the mass-weighted specific surface area, were compared to the lysozyme coverage measured on the 90ZB filter. The lower two of these three are comparable to the lysozyme coverage measured on the 90ZB filter, which is low compared to monolayer coverage for lysozyme and therefore an even smaller fraction of monolayer coverage for the larger mAbs. For comparison, the breakthrough experiment using β -lactoglobulin yielded coverage of about $1.6 \text{ mg}/\text{m}^2$, comparable to the small-scale batch experimental findings from Figure 2.6B, indicating the relevance of the small-scale experimental results. These results support a dominant role for electrostatically-driven adsorption and show that calculated monolayer coverage is a useful guide for estimating the theoretical maximum capacity of a depth filter for adsorption of therapeutic targets.

In an attempt to understand the relative extents of adsorption in terms of the structural differences among the three mAbs, the sequences were compared and most

of the differences were found in the complementarity-determining regions (CDR). The surface area of anionic patches found on the electrostatic surface potential (Gilson and Honig, 1987) of the CDR at pH 7.2 is, in descending order, mAb C, B and D. On the other hand, the ranking of the hydrophobicity of the mAbs using the spatial-aggregation-propensity model (Chennamsetty et al., 2009) is, in descending order, mAb D, B and C. These findings suggest that hydrophobic interactions may contribute to the higher adsorptive capacity of the depth filter for mAb D compared to mAb B and C. However, the presence of more anionic patches on mAb C may contribute to the higher adsorptive capacity of the depth filter for mAb C over B, although the difference between the two is very small.

2.4 Conclusions

The characterization of depth filters and their components described here provides quantitative and mechanistic information regarding their protein adsorptive functionality. These complement the current body of work on depth filtration in bioprocessing and extend our understanding of a depth filter as a composite unit. The differences in the extent of protein adsorption onto two nominally similar siliceous filter aids were supported by the comparative differences in measured relative surface charge density and morphology. Decoupling protein coverage on the depth filter from adsorption onto its most abundant component, the filter aid, reveals the prevalence of the polymeric binder coat over a large fraction of the depth filter surface area, solidifying the binder's role as the primary contributor to the adsorptive functionality through electrostatic interactions.

Furthermore, visualization of protein-adsorbed depth filters allows comparison of the spatial distribution of protein adsorption, and through it of the binder, over the

depth filter surface. The 90ZB depth filter appeared to be more homogeneously coated with the binder and possessed the highest capacity among the cases considered for an acidic model protein. The comparability of the 90ZB depth filter capacity for a basic model protein (lysozyme) and two of the three therapeutic mAbs considered demonstrates that protein surface coverage, and the monolayer coverage to some extent, can be used to approximate a depth filter's maximum capacity for therapeutic targets and protein impurities. Which proteins are likely to adsorb can be assessed to a first approximation from electrostatic considerations; for instance, 46% of the identified host cell proteins identified in mAb production from Chinese hamster ovary cells have isoelectric points below 7.3 (Aboulaich et al., 2014), so they would be expected to bind at pH values typical for cell culture. Furthermore, changing the charge of the binder may allow manipulation of binding affinity. Quantitative estimates of the amount of protein bound may be obtained from estimates of monolayer coverage.

Chapter 3

THE CONTRIBUTIONS OF ADSORPTION AND SIZE-BASED FILTRATION TO DNA REMOVAL ON DEPTH FILTERS

3.1 Introduction

Animal cell culture has been used to produce recombinant proteins for human application since 1985 (Smith, 1996). Over the subsequent decades the understanding of the risks associated with the cellular components, which are process-related impurities, has evolved. DNA, which is excreted from the cells due to either apoptosis or necrosis, was originally considered a risk factor because the continuous cell lines in question were immortalized, leading to a requirement that DNA be reduced to exceptionally low levels (Petricciani and Horaud, 1995; Wurm, 2004). However, after additional findings showing lack of tumor development in primates injected with tumor chromatin (Wierenga et al., 1995) and thorough evaluation of the contextual risks (Petricciani and Horaud, 1995), the World Health Organization recommended that residual DNA be considered a general cellular contaminant, and up to 10 ng of DNA may be present per dose (Griffiths, 1997).

Since the perspective on residual DNA has changed to that of a simple impurity, the removal of DNA in downstream operations is tracked primarily in terms of its total mass. DNA is usually quantified based on UV absorbance at 260 nm by the heterocyclic rings in the DNA bases and fluorescence emission upon the intercalation of dye into DNA. Tracking the mass balance of DNA by utilizing these approaches has shown that a range of separations media, including immuno-affinity (Tauer et al.,

1995), anion-exchange (Jiskoot et al., 1989), and size-exclusion (Ng and Mitra, 1994) resins, as well as filter aids and depth filters (Yigzaw et al., 2006b), can reduce the total amount of DNA by two logs or more. In addition to adsorbent-based purification approaches, DNA removal of three logs has been obtained by precipitation using cationic detergents (Goerke et al., 2005). Among these methods, determining the mechanisms by which depth filters remove DNA is less straightforward. Depth filters generally comprise a base of cellulose or polypropylene fibers, siliceous filter aid and cationic polymeric binder with primary to quaternary amine functional groups (3M, 2013).

Since depth filters are an amalgamation of disparate components, impurities can be retained on them via various functionalities, as a result of which the mechanisms by which various impurities such as nucleic acids, proteins and cellular debris are removed can be difficult to decouple. Charlton et al. found that buffers that neutralize the charge on the depth filter and impede possible hydrophobic interactions reduced the operational capacity of the depth filter (Charlton et al., 1999), while Singh et al. suggested that while electrostatic interactions are primary in the removal of DNA, other interactions such as hydrogen bonding also play an essential role (Singh et al., 2017).

The lack of information other than the total mass of the DNA, determined using absorbance or fluorescence methods, can be limiting in inferring the various mechanisms that may be involved. In particular, these measurements cannot shed light on the DNA length and size distribution and their effect on the retention and escape of DNA. DNA secreted from NS0 myeloma cells in the later stages of batch cell culture has been found to comprise both high molecular weight and short oligo-like fragments

(Murray et al., 1996). The presence of relatively low molecular weight DNA fragments could be linked to the fragmentation of nucleosomes from nuclear chromatin by an intracellular endonuclease during programmed cell death (Wyllie, 1980). Charlton et al. investigated the molecular weight of DNA from clarified, large-scale, fed-batch, mammalian cell culture and reported that it is predominantly of less than 1 kDa. However, since both apoptosis and necrosis can be present in cell culture conditions, they could not further determine the source of these smaller DNA fragments with certainty (Charlton et al., 1998).

Keeping in mind the uncertainty of the distribution of length and hence effective size in a DNA impurity, we have investigated the mechanisms involved in the retention of DNA on depth filters by directly visualizing retained DNA on spent depth filters. The distribution of the retained DNA on a spent depth filter need not be the same for two disparate DNA samples of equal total DNA mass, and the differences show the importance of the effect of DNA length and effective size on retention profiles. This is the first instance of which we are aware where the distribution of retained DNA on spent depth filters has been visualized directly to substantiate the importance of DNA size and length distributions on the retention profile.

3.2 Materials and methods

3.2.1 Materials

Monobasic sodium phosphate (NaH_2PO_4), sodium phosphate dibasic (Na_2HPO_4), sodium bicarbonate (NaHCO_3), tris base ($\text{C}_4\text{H}_{11}\text{NO}_3$), hydrochloric acid (HCl), sodium chloride (NaCl), anhydrous DMSO, NHS-rhodamine, copper(II) sulfate pentahydrate ($\text{CuSO}_4 \cdot 5\text{H}_2\text{O}$), l-ascorbic acid sodium salt ($\text{C}_6\text{H}_7\text{NaO}_6$),

peptone and yeast extract were all purchased from Fisher Scientific (Fair Lawn, NJ). 3M provided samples (discs) of diameter 10 mm of the 90ZB grade commercial depth filter media.

β -lactoglobulin from bovine milk was purchased from Sigma-Aldrich (St. Louis, MO). NoLimits™ individual dsDNA fragments of 500 and 5000 base pairs (bp) were purchased from ThermoFisher Scientific (Waltham, MA), while custom-designed dsDNA fragments of 50 bp and 90 bp were ordered from Integrated DNA Technologies (IDT, Coralville, IA). Bristol-Myers Squibb (Devens, MA) provided CHO genomic DNA of 1.29 mg/mL in 10 mM tris, 1 mM EDTA at pH 8.

Chinese hamster ovary (CHO)-K1 cell line was provided by the Millicent O. Sullivan research group, University of Delaware. Gibco™ Dulbecco's modification of Eagle's medium (DMEM), Gibco™ phosphate-buffered saline (PBS), pH 7.2, Gibco™ fetal bovine serum (FBS), Gibco™ trypsin-EDTA (0.25%) and Gibco™ penicillin-streptomycin (10,000 U/mL) were purchased from Fisher Scientific. 5-Ethynyl-2'-deoxyuridine (EdU) and 5-TAMRA azide were purchased from Click Chemistry Tools (Scottsdale, AZ).

A cloning vector of 6136 base pairs, pET28a mCherry, was provided by the Joseph M. Fox research group, University of Delaware. Restriction enzymes EcoRI-HF and XbaI were purchased from New England Biolabs (Ipswich, MA) and HiSpeed plasmid mega extraction kits and QIAquick gel extraction kits were purchased from Qiagen (Hilden, Germany).

3.2.2 Generating dsDNA fragment of 5226 bp

The plasmid was provided in bacteria streaked on an agar plate. Two to three colonies were inoculated into each of three vials containing 3 mL of lysogeny broth

(LB) with 100 µg/mL ampicillin and placed in an incubator at 37 °C for 8 hours. Approximately 4.5 mL of the starter culture was then inoculated into each of two baffled flasks containing 500 mL of LB containing 100 µg/mL ampicillin, which were shaken at 180 rpm for 13 hours at 37 °C. Plasmid DNA was extracted from the resulting culture using a HiSpeed plasmid mega kit from Qiagen (Mansfield, MA) following the manufacturer's protocol. The purified plasmids were digested with EcoRI and XbaI restriction endonucleases at 0.5 unit of each enzyme per µg of dsDNA for 11 hours following the manufacturer's protocol. Two separate bands at ~ 900 bp and ~ 5000 bp were seen on 1% agarose gel electrophoresis, confirming that the digest was complete. Following digestion, the sample was concentrated by isopropanol precipitation in which isopropanol equivalent to 70% of the sample volume was added to the DNA sample and centrifuged at 161,000 g for 10 minutes. The pellet containing the DNA was dissolved in 50 µL of 10 mM tris, 1 mM EDTA at pH 8.0 prior to extraction via electrophoresis in a 1% agarose gel. The two dsDNA fragments were separated using a QIAquick Gel Extraction Kit from Qiagen following the manufacturer's protocol.

3.2.3 Generating dsDNA fragments of 50 and 90 bps

Randomly generated DNA sequences of 50 bp and 90 bp, with GC content of 40-42 % and T_m of 64-70 °C, and their respective reverse complementary strands were purchased from IDT and were annealed following IDT's protocol. The annealed products were suspended in 10 mM tris with 100 mM NaCl and 1 mM EDTA at pH 7.5.

3.2.4 dsDNA characterization

The 5226 bp DNA fragment was analyzed using a multi-angle light scattering detector, Dawn Heleos II, from Wyatt, over a collection period of 5 minutes. Scattering intensities for sample concentrations of 0.045, 0.091, 0.136 and 0.181 mg/mL were measured across the detectors at angles θ of 64°, 72°, 81°, 90° and 108° from the sample cell to construct a Zimm plot, consistent with the relation for the Rayleigh ratio R_θ in terms of the form factor for small submicron particles that scatter light (Matijević, 1979):

$$\frac{Kc}{R_\theta} = \left(\frac{1}{M_w} + 2A_2c \right) \left[1 + \frac{16\pi^2 n^2 R_g^2}{3\lambda^2} \sin^2 \left(\frac{\theta}{2} \right) \right] \quad (3.1)$$

In the equations below, n , λ , and c denote the refractive index, laser wavelength, and sample concentration, respectively, while

$$K = \frac{2\pi^2 \left(\frac{dn}{dc} \right)^2}{\lambda^4 N_{AV}} \quad (3.2)$$

where N_{AV} is Avogadro's number. The Zimm plot allows simultaneous extrapolation of the experimental static light scattering intensity to both the zero angle and zero concentration limits to allow the molecular weight M_w , second virial coefficient A_2 , and radius of gyration R_g to be estimated. As shown in Equation 1, in the limit of zero concentration, R_g can be estimated from the slope of the plot of Kc/R_θ as a function of $\sin^2(\theta/2) + Bc$, where B is an arbitrary constant that is selected to ensure that the concentration term is of a comparable magnitude to $\sin^2(\theta/2)$, which varies from 0 to 1 (Chu, 1970). The radius of gyration was inferred in the limit of sample concentrations approaching zero. An isotropic scatterer, bovine serum albumin (0.75 mg/mL), was used to normalize the light scattering detectors in each buffer under consideration, which relates the measured voltage at each detector to that of the 90° detector and offset the differences in the gain between the detectors. Toluene was used as a

standard for instrument calibration and the scattering from the respective buffers was subtracted from that of the sample of interest.

3.2.5 β -lactoglobulin and DNA labeling

β -lactoglobulin was fluorescently labeled via its primary amine groups using NHS-Rhodamine (ThermoFisher Scientific), following the manufacturer's protocol with some modifications. NHS-Rhodamine was dissolved in DMSO at 10 mg/mL and was added to 1 mL of a 10 mg/mL β -lactoglobulin solution in 100 mM sodium phosphate, 150 mM sodium chloride, pH 7.4, at a molar dye-to-protein ratio of 0.5:1. Label IT[®] nucleic acid labeling kit Cy[®]5 from Mirus Bio (Madison, WI) was used to covalently tag the cyanine dye along with a linker onto the 7th nitrogen of the guanine base. The manufacturer's protocol was followed with the exception of a reduction in the ratio of μ g of nucleic acid to μ L of Label IT[®] reagent to 1: 0.025 - 0.05.

3.2.6 Chromosomal DNA labeling and lysate preparation

Adherent CHO-K1 cells were labeled using EdU following the protocol described by Salic et al. (Salic and Mitchison, 2008), with modifications. Adherent CHO-K1 cells were grown in DMEM with 10% FBS, penicillin and streptomycin. After the fifth passage at ~ 40% confluency, EdU was added to the dividing cells at 0, 4, 8 and 12 hours to obtain concentrations of 100, 400, 2500 and 10000 nM, respectively. After an additional 12 hours, the cells were washed with PBS and 10 mL of the staining solution, comprising PBS supplemented with 0.5 mM copper(II) sulfate pentahydrate, 1 μ M 5-TAMRA-azide and 50 mM l-ascorbic acid sodium salt, was added to the T-75 flask with adherent cells. The cells were placed in a 37 °C incubator for 30 minutes, after which the staining solution was replaced with PBS and 1 mL

trypsin was used to detach the cells and the cells were collected using the previously-described growth media. A 15 mL cellular suspension of ~ 90,000 cells/mL in the growth media was vortexed for 3 minutes and then lysed by passing it 10 times between two syringes connected by a union with a negligible orifice and a low dead volume. The overall time elapsed was approximately 1 minute. One third of the lysate was kept for analysis of its retention on the depth filter while the rest was centrifuged at 4500 rpm for 1 hour. After centrifugation, the supernatant was collected while the pellet was resuspended in 4 mL of the growth media.

3.2.7 Sample loading onto the depth filter

Depth filter (90ZB) discs 10 mm in diameter were punched out using a custom-made punching set comprising a male and a female part. The disc was then inserted into the online filter holder of an Äkta Explorer in place of the standard 10 mm diameter polypropylene filter and placed on a column position. The standard operating procedure comprised washing of the filter using 13 mL (165.6 L/m²) of the buffer under consideration at a flow rate of 1.5 mL/min (1146.5 LMH), followed by loading of a 2 mL (25.5 L/m²) sample at 1 mL/min (764.3 LMH) and washing with 5 mL (63.7 L/m²) of the same buffer at 1 mL/min (764.3 LMH). The pressure drops during the experiments with the 90ZB depth filter were approximately 0.35 – 0.4 MPa. The only significant increase in pressure seen during sample loading was by about 10%, during loading of the resuspended lysate pellet. The depth filter pieces were subsequently stored at –20 °C for 3-48 hours in an opaque container until they were visualized by confocal microscopy.

3.2.8 Depth filter visualization and image analysis

After sample loading, the 10 mm 90ZB depth filter discs were sliced along the center using a MITER CUT precision cutting tool (Lexington, KY) to give two approximately equal three-dimensional arcs. The wet sliced faces of the half discs were placed on a glass slide, making sure there was a minimal gap between them, and visualized on a Zeiss 710 inverted confocal microscope (Oberkochen, Germany) using a Zeiss 10× EC Plan-Neofluar (0.3 NA) objective. The laser intensity, gain and pinhole were kept constant in visualizing the comparative sample sets to allow for direct and qualitative comparison. The depth probed along the z-axis (depth into the samples) was also kept similar ($\pm 2 \mu\text{m}$) to ensure that the densities of collapsed visualizations were comparable. Fixed-area thresholding was performed in Image J between a set of images, where direct comparisons of the extent of DNA penetration were made.

3.3 Results and discussion

3.3.1 DNA vs. protein retention

The retention of CHO genomic DNA (red) and β -lactoglobulin (green) on the 90ZB depth filter is shown in Figure 3.1. Fifteen μg DNA and 2 mg β -lactoglobulin were loaded in all three cases using 2 mL of 10 mM sodium phosphate at pH 8, but three modes of loading were used in order to probe the mechanisms driving DNA retention. In Figure 3.1A, β -lactoglobulin was loaded first, followed by DNA, while in Figure 3.1B, DNA was loaded first, then β -lactoglobulin was loaded after the depth filter was flipped over to reverse the flow direction. These modes were used to determine whether the presence of one species would affect the subsequent retention of the other, specifically whether DNA would compete with β -lactoglobulin in

adsorbing onto the depth filter or would co-exist via means other than adsorption. The filter was flipped after the loading of DNA in Figure 3.1B to determine, in addition, whether the retained DNA would break through, remain stationary or rearrange in position with flow in the opposing direction. For the results in Figure 3.1C, DNA and β -lactoglobulin were mixed just prior to loading.

β -lactoglobulin saturates the depth filter while DNA is retained near the top face of the filter in all cases. Figures 3.1A and 3.1C are similar in that the DNA appears to be retained primarily on the surface. Whether DNA is loaded prior to protein or along with protein does not appear to impact the extent to which DNA is able to migrate into the filter. It is also worth noting that although the 90ZB depth filter has a nominal retention rating of 0.2 μm (3M, 2013), it has a pore size gradient along the depth of the filter, so the pores become narrower with depth into the filter.

Our previous work (Khanal et al., 2018) showed that the 90ZB depth filter's adsorption capacity for β -lactoglobulin is $\sim 1.7 \text{ mg/m}^2$ using 10 mM sodium phosphate buffer at pH 8 and that the 90ZB depth filter has a specific surface area of $4.86 \text{ m}^2/\text{mg}$. Given that a 90ZB depth filter disc of 10 mm in diameter weighs 90–120 mg, we can deduce that our filter is able to retain only $\sim 0.75\text{--}1 \text{ mg}$ of β -lactoglobulin. Hence, it is saturated with protein and DNA resides along with the protein at the upper surface. The distribution of DNA in the case where the filter is flipped after loading DNA, prior to loading protein, is less dense and the DNA is present to a greater depth (Figure 3.1B). This and the filter's saturation by protein suggest that the DNA is not strongly adsorbed and is able to redistribute with flow. Furthermore, it is possible that some DNA was lost in the scenario shown in Figure 3.1B. The flow in this case during

protein loading is in the direction of increasing pore size, whereas in the case of Figure 3.1A, the flow is in the direction of decreasing pore size.

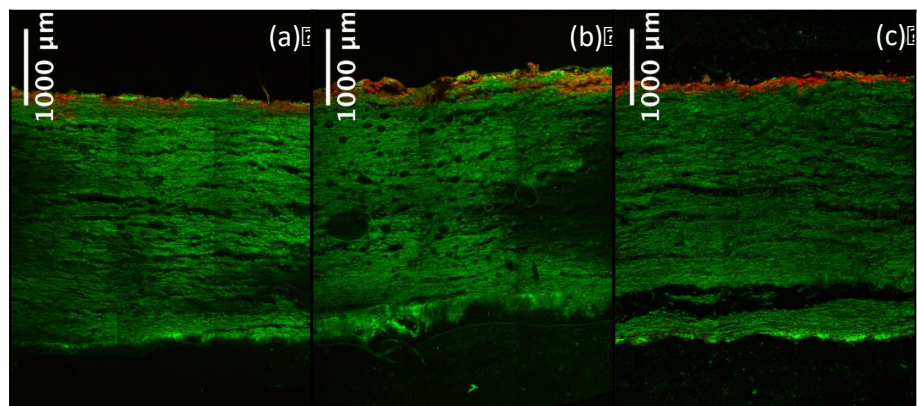


Figure 3.1 Retained CHO genomic DNA (red) and β -lactoglobulin (green) on the 90ZB depth filter; overlapping regions appear orange. (A) β -lactoglobulin was loaded first followed by DNA; (B) DNA was loaded first, then the depth filter was flipped over to load β -lactoglobulin with the flow reversed; (C) DNA and β -lactoglobulin were premixed and loaded simultaneously. Fifteen μ g DNA and 2 mg β -lactoglobulin were loaded in all three cases using 2 mL of 10 mM sodium phosphate at pH 8.

3.3.2 Effect of sample and process parameters

In order to determine whether the retention of CHO genomic DNA on the filter surface was due primarily to the large size of CHO genomic DNA or to a limited injected sample mass (15 μ g), the retention profiles of a larger quantity of genomic DNA as well as of a DNA oligo were explored. Figures 3.2A, B and C show the retention of 15 μ g of CHO genomic DNA, 500 μ g of CHO genomic DNA and 300 μ g of a 90 bp DNA oligo, respectively, loaded using 2 mL of 10 mM sodium phosphate buffer at pH 8 on the 90ZB depth filter. Although further displacement into the filter is seen in Figure 3.2B compared to that in Figure 3.2A, the difference in the extent to

which DNA penetrates into the depth filter is not significant given the 33-fold increase in the mass of CHO genomic DNA loaded. This finding indicates that while the retention of proteins like β -lactoglobulin is driven primarily by electrostatic interactions between the protein and the resin binder of the depth filter (Khanal et al., 2018), the retention of DNA, which can be present in a wide range of sizes, is dictated largely by size-based retention effects.

Compared to the limited permeability of CHO genomic DNA, the DNA oligo of 90 bp was able to penetrate the depth filter significantly further and was retained in a manner similar to that of β -lactoglobulin (Figure 3.2C). The 90 bp oligo molecular weight of 55.5 kDa is of the same order of magnitude as β -lactoglobulin (18.4 kDa), and although the size of the DNA may be significantly greater than that of protein (see below), electrostatic interactions and short-range interactions are likely play a greater role in its retention if it remains much smaller than the depth filter pores.

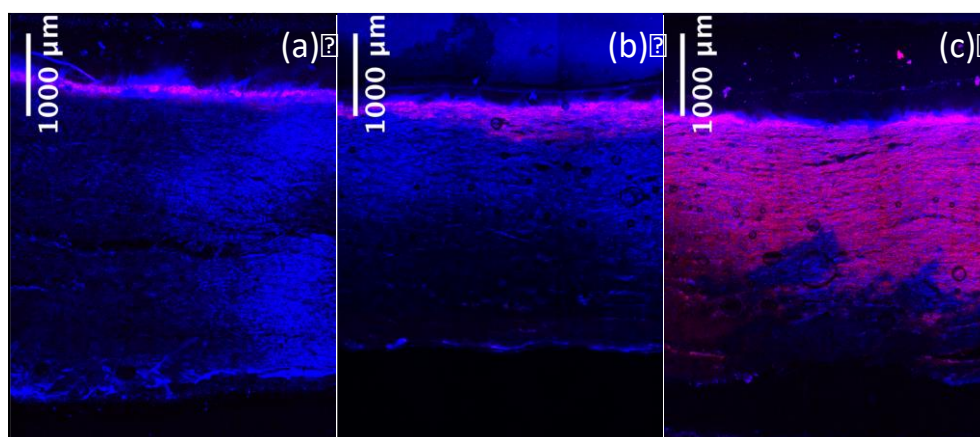


Figure 3.2 Retained DNA on the 90ZB depth filter. DNA is shown in red while the depth filter's autofluorescence in the blue region is shown in blue and the overlapping regions appear pink. (A, B) 15 μ g and 500 μ g CHO genomic DNA, respectively, were loaded following the standard procedure. (C) 300 μ g of 90 bp DNA oligo was loaded. All three samples were loaded using 2 mL of 10 mM sodium phosphate at pH 8.

3.3.3 Correlations among DNA length, effective size and penetration

Figure 3.3 shows the retention of 10 μg each of three DNA fragments of different length, loaded in 2 mL of 10 mM sodium phosphate buffer at pH 8. The qualitative reduction in the extent of DNA penetration with increasing DNA length is readily apparent, but a more quantitative interpretation of the confocal images was obtained by fixed area thresholding of the three images under comparison. Figure 3.4 shows a quantitative decrease in the extent of DNA penetration as a function of DNA length as expressed through the greatest depth into the filter, which is defined as the distance from the surface of the filter to the furthest distance the DNA has reached, and the % area of the depth filter where the DNA is seen. The data suggest that size-based retention of DNA is a combined effect of DNA length and the pore size gradient along the depth of the filter.

In order to interpret the extent of penetration into the depth filter (Figure 3.4) in terms of the effective size of DNA as a function of the contour length, efforts were made to estimate the effective size. For the 5226 bp DNA sample, the radius of gyration was estimated from static light scattering (SLS) using a Zimm plot as 124 ± 6 nm (95% confidence interval). This value is slightly smaller than for comparable studies in the literature, although fairly consistent given differences in the sample (Latulippe and Zydney, 2010; Smith et al., 1996; Voordouw et al., 1978). The geometric diameter, relevant to the study of retention and penetration through the filter, would then be of order 300 nm. Since the nominal retention rating of the 90ZB filter is 200 nm, it is reasonable that DNA fragments of ~ 5000 bp would not penetrate a depth filter, as shown in Figure 3.3C.

For the two smaller DNA samples the interpretation is less clear, as SLS data were not reliable for the 500 bp sample and unobtainable for the 50 bp sample.

Furthermore, using a contour length of 0.33 nm/bp (Borochoy et al., 1981; Sanchez-Sevilla et al., 2002) gives contour lengths of 165 nm and 16.5 nm for the respective samples. Since the persistence length of DNA is approx. in the range 50 nm (Garcia et al., 2007; Hammermann et al., 1997), these two samples cannot be considered as globular coils but rather as a bent fiber (500 bp) or a rigid rod (50 bp). The lack of a single characteristic length and the possibility of alignment of the DNA with the flow field makes clear conclusions regarding effective size problematic. However, for these two samples retention by a nominal 200 nm filter appears likely to be either only partial or negligible, generally consistent with the results for these two samples in Figure 3.4.

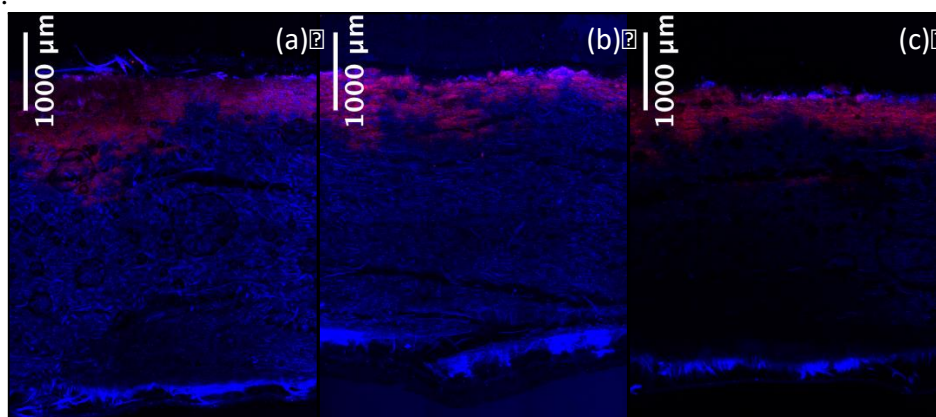


Figure 3.3 Retained DNA of (A) 50, (B) 500 and (C) 5000 bp on the 90ZB depth filter. DNA is shown in red while depth filter autofluorescence in the blue region is shown in blue and the overlapping regions appear pink. DNA sample masses of 10 µg were loaded in all three samples using 2 mL of 10 mM sodium phosphate at pH 8.

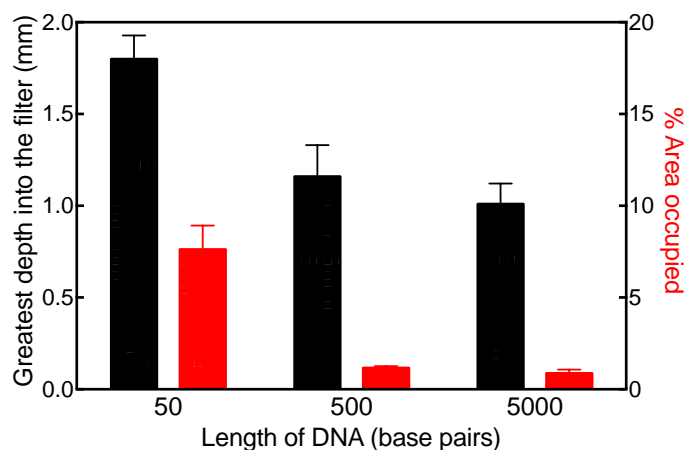


Figure 3.4 Retention of DNA fragments of 50, 500 and 5000 bp on the 90ZB depth filter represented as the greatest depth into the filter (black) and the % area occupied (red).

3.3.4 Effect of wash volume and buffer ionic strength

Apart from the effect of the size of the DNA, the effect of operational parameters such as wash volume and buffer ionic strength on the extent of DNA penetration into the depth filter were also explored. Figure 3.5 shows that when the loading of 15 μg of CHO genomic DNA in 2 mL of buffer (10 mM sodium phosphate, pH 8) was followed by 5, 50, 100 and 200 mL (64-2546 L/m²) of the same buffer at 1528 LMH, the small amount of DNA was displaced further into the depth filter. Figure 3.6 shows that both the greatest depth into the filter and the % area occupied by each sample increase with increasing wash volume, with the exception of the lowest wash volume. This indicates that large DNA, such as CHO genomic DNA, is not strongly bound or adsorbed onto the filter and is retained primarily through size-based retention effects. Figures 3.1B and C also indicate that DNA, unlike acidic proteins, is not sufficiently strongly bound or adsorbed on the surface to prevent its travel through the filter with flow.

The strength of adsorption can be directly affected by another operational parameter, buffer ionic strength, which was also systematically varied by loading 10 μg of 50 bp DNA oligo using 10 mM tris buffer, pH 7.5, also containing 0, 56 or 504 mM NaCl to give 8, 64 and 512 mM total ionic strengths, respectively. In this experiment, tris buffer was chosen to remove the effect of binding of buffer anions to the depth filter, as is possible with phosphate. Figure 3.7 shows that the greatest depth into the filter increases with increasing buffer ionic strength, although the difference appears to be more pronounced at lower ionic strengths. This may be due in part to screening of electrostatically-driven adsorption but also screening of intramolecular electrostatic repulsion, which reduces the stiffness of the DNA and allows it to become more compact (Borochoy et al., 1981) and hence to penetrate further into the depth filter. Therefore, the buffer ionic strength can impact the extent to which DNA, as a process impurity, is retained on the depth filter or escapes into the filtrate.

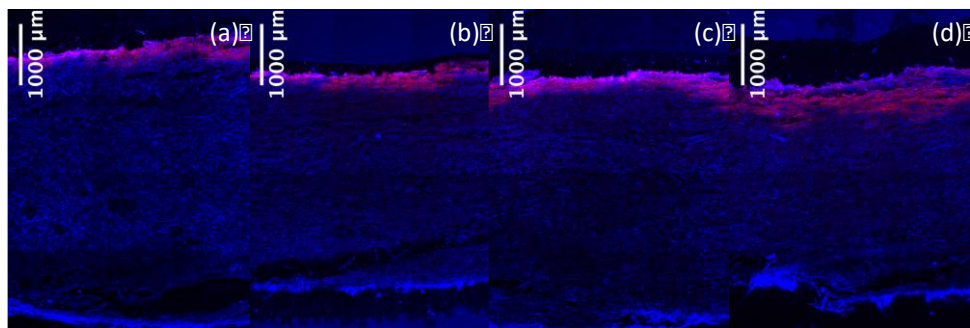


Figure 3.5 Effect of wash volume on distribution of retained DNA on the 90ZB depth filter. DNA is shown in red while the depth filter's autofluorescence in the blue region is shown in blue and the overlapping regions appear pink. 15 μg CHO genomic DNA was loaded, followed by a wash volume of 64, 637, 1273 or 2546 L/m^2 at 1528 LMH.

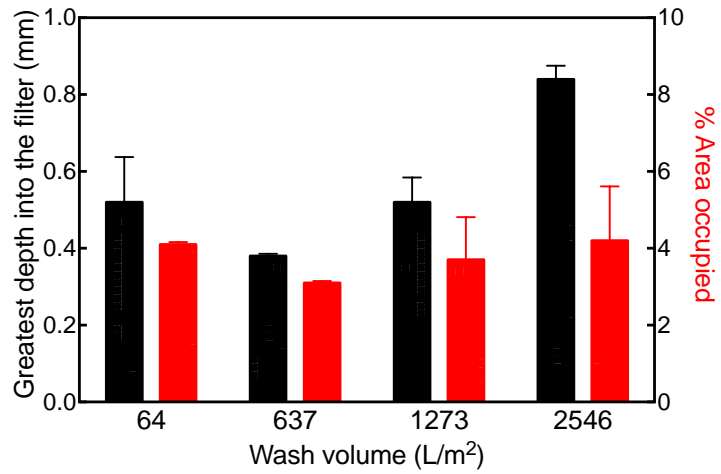


Figure 3.6 Retention of CHO genomic DNA on 90ZB depth filter as a function of buffer wash volume. Results are represented as the greatest depth into the filter (black) and the % area occupied (red).

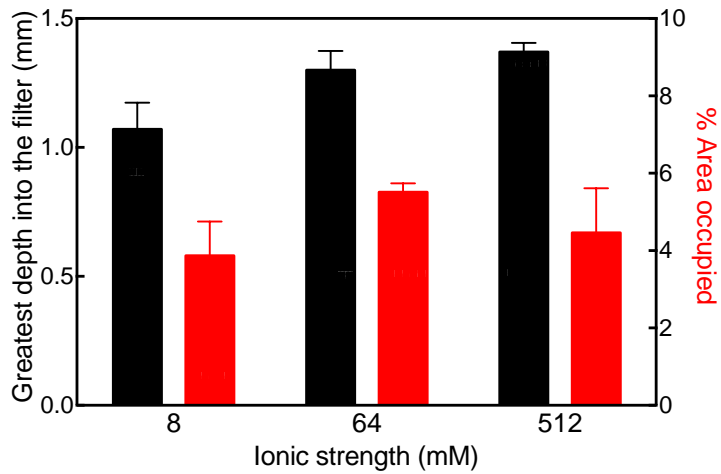


Figure 3.7 Retention of 50 bp DNA fragment on 90ZB depth filter as a function of buffer ionic strength. Results are represented as the greatest depth into the filter (black) and the % area occupied (red).

3.3.5 Retention of chromosomal DNA

The retention of CHO chromosomal DNA was visualized by incorporating EdU into dividing adherent CHO-K1 cells and detecting it with 5-TAMRA azide. The cell lysate was centrifuged, and the subsequent supernatant and the re-suspended pellet were loaded onto the 90ZB depth filter. Figures 3.8A, B and C show the retention profiles of the CHO-K1 lysate, its supernatant and pellet after re-suspension, on the 90ZB depth filter, respectively. DNA in the supernatant penetrates slightly into the filter, but similarly to pure DNA of a few kbp, the re-suspended pellet is retained strictly on the surface of the filter; the pellet appears rich in DNA. The surface retention of the resuspended pellet is explained by the size of the particles carrying the DNA, shown in Figure 3.9. Despite the heterogeneity in the particulates size, these are much larger than the depth filter's nominal retention rating of 0.2 μm , which may include whole cells and cell debris. The mixture prior to centrifugation has the features seen in both the supernatant and the re-suspended pellet; a brighter band at the top (re-suspended pellet) with some DNA penetration into the filter (supernatant), as seen in Figure 3.8C. A qualitative comparison between the retention of purified CHO genomic DNA and CHO intracellular DNA suggests that DNA during harvest clarification is lengthy and cleared primarily through exclusion, although the concentration in the case of the DNA from the CHO culture was not controlled.

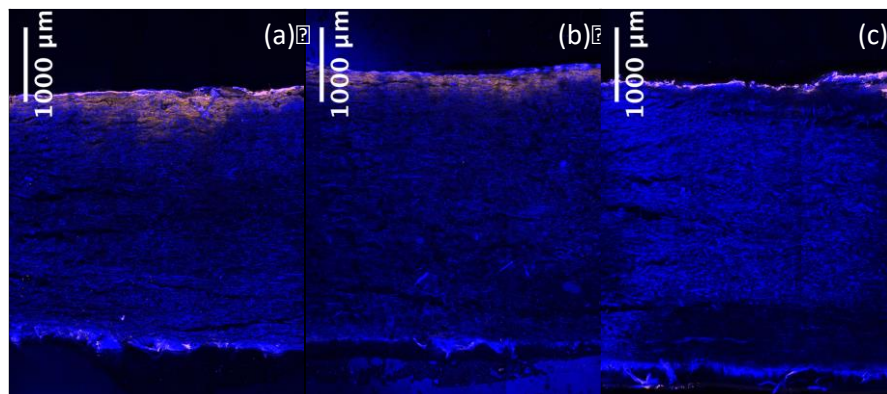


Figure 3.8 Retention of CHO-K1 lysate, its supernatant and pellet after re-suspension, on the 90ZB depth filter are shown in (A), (B) and (C), respectively.

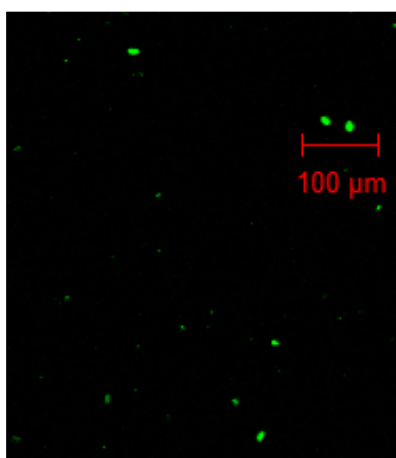


Figure 3.9 Fluorescent particulates from the re-suspended pellet.

3.4 Conclusions

The visualization of the retained-DNA distribution on the 90ZB depth filter, shown here, provides information relating the length of DNA to its retention and capacity on the depth filter. Genomic DNA and longer lengths of DNA were found to be primarily retained on the surface and hence excluded from the interior of the filter,

while short oligos can adsorb throughout the depth filter. The use of confocal microscopy allows for qualitative discrimination of retention – driven primarily by electrostatic interactions – from retention by size-based filtration. These findings provide another facet to the understanding of DNA clearance using depth filters, in that apart from the depth filters themselves, the properties of DNA, as an impurity, also impact its propensity to be retained on the depth filter. Furthermore, the greater penetration of the retained DNA on the depth filter with an increase in the buffer strength and the wash volume inform the impact of process parameter changes on DNA clearance. Labeled CHO intracellular DNA was also retained on the surface, suggesting that DNA during harvest clarification is either lengthy or exists within the debris and is cleared primarily through exclusion. Our experimental approach can be leveraged in investigating the current approaches to removal of DNA, whether in its form as an impurity or as a therapeutic product. The experimental design can potentially be used to study the retention kinetics of nucleic acids and other impurities on depth filters at a reasonably small scale. Furthermore, these findings can directly inform depth filter and operational parameter selection for efficient removal of DNA.

Chapter 4

ESTIMATING AND LEVERAGING PROTEIN DIFFUSION ON ION-EXCHANGE RESIN SURFACES

4.1 Introduction

Protein diffusion on surfaces is prevalent in biological events such as the diffusion of reparatory protein complexes on dsDNA for break repair (Brouwer et al., 2016) and of surface-mobile amyloid- β peptides in enhancing fibril formation, associated with neurodegenerative diseases (Lin et al., 2018; Shen et al., 2012). Protein surface diffusion can also impact the performance of microcapillary immunosensors (Kaneki et al., 1994; Wang et al., 2008) and of label-free technologies such as surface plasmon resonance sensors (Johnsson et al., 1991) and chromatography (Schmidt-Traub, 2005). The phenomenon has also been invoked in analysis of preparative ion-exchange chromatography (IEX) of proteins, an enabling technology for high-selectivity adsorptive purification of proteins based on differences in their charge properties. The chromatographic beads used for IEX feature narrow, tortuous pores to maximize the surface-to-volume ratio, making intraparticle diffusion the rate-limiting factor in protein adsorption. Inside the particle, diffusion can occur in the liquid pore space (pore diffusion) and potentially on the resin surface (surface diffusion), as shown in the simplified schematic in Figure 4.1 (Feller et al., 2010; Wesselingh and Bosma, 2001). On the particle length scale, such surface diffusion can enhance the protein uptake rate and consequently also the process efficiency. Surface diffusion can also increase the local capacity for protein adsorption beyond what is anticipated for

random sequential adsorption by allowing rearrangement of adsorbed molecules to improve the packing efficiency. In both these cases, modulation of the protein diffusivity on the surface (D_s) can provide an additional means to improve performance. However, protein surface diffusion is not sufficiently well accepted to be used by design to enhance performance.

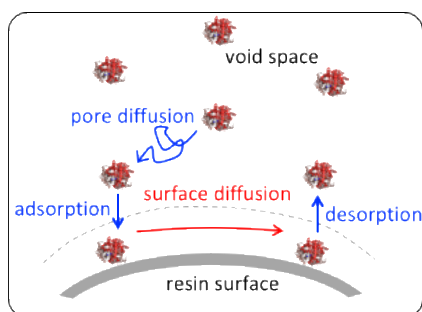


Figure 4.1 Schematic of protein diffusion in the pore space and on the surface of the resin.

Surface diffusion of small molecules (Choi et al., 2001; Medved' and Černý, 2011; Yoshida et al., 1994) and polymers (Wang et al., 2015; Wang et al., 2016; Zhao and Granick, 2004; Zhao and Granick, 2007), unlike that of proteins, has been widely reported in liquid-solid systems. In reverse-phase liquid chromatography, hydrocarbons have been reported to diffuse at the interfacial region near the end of the alkyl chains of the stationary phase (Gritti and Guiochon, 2011; Gritti and Guiochon, 2014; Miyabe and Guiochon, 2010; Rybka et al., 2015; Rybka et al., 2017). Surface diffusion of proteins is more difficult to study due to their size and anisotropic structures, as well as their stronger adsorption. For conditions relevant to IEX, where protein-surface attraction is governed mainly by electrostatic interactions, the surface diffusivity of bovine serum albumin (BSA) (Feller et al., 2010; Michaeli et al., 1980;

Tilton et al., 1990) and ferritin (Nygren et al., 1994) on flat charged surfaces has been measured. However, for structurally-intact IEX particles, direct observation of the surface is difficult and surface diffusion has been inferred with the aid of mechanistic chromatographic modeling (Basconi et al., 2014; Wesselingh and Bosma, 2001). Differences in protein uptake patterns among resins of different structures, observed by confocal microscopy, could be explained by the presence of surface diffusion but with a variable D_s (Corbett et al., 2013; Stone et al., 2009). For mechanistic models accounting for surface diffusion, the dependence of D_s on protein concentration (Miyabe and Guiochon, 2000; Weaver and Carta, 1996; Yoshida et al., 1994), ionic strength (Basconi et al., 2014; Feller et al., 2010) and binding strength (Wesselingh and Bosma, 2001) has been reported, warranting a consistent and more comprehensive investigation into protein surface diffusion in IEX. An extensive understanding of protein surface diffusion in IEX can inspire engineering measures that can reduce losses associated with what the FDA describes as inefficient and wasteful manufacturing (Woodcock and Woosley, 2008) of increasingly prevalent (Wu, 2000) and costly therapeutic proteins.

Bridging a gap between idealized investigations and practical applications, we probe the role of surface diffusion in the uptake of an industrially relevant protein, a monoclonal antibody (mAb), onto commercial resins. We probed the variability of protein D_s and its dependence on parameters pertaining to protein adsorption, such as buffer pH, ionic strength (IS) and the adsorbent ligand density. Using our findings, we developed a novel gradient method of protein loading that significantly increases resin utility. As was done in the prior studies noted above, we estimated D_s using a mechanistic column model. However, the impact of surface diffusion on protein

uptake was also investigated via microscale observations by confocal microscopy and nanoscale structure characterization by small-angle neutron scattering (SANS) to corroborate and expand the model insights. This multi-pronged approach informed the exploitation of the surface diffusivity to increase protein uptake, transcending the customary perception that it limits protein uptake.

4.2 Materials and methods

4.2.1 Materials

Amersham Cy3.5 mono-reactive dye (GE Healthcare, Chicago, IL) was purchased from Fisher Scientific. Deuterium oxide (D, 99%) and acetic acid-D₄ (D, 99.5%) were purchased from Cambridge Isotope Laboratories (Tewksbury, MA). The mAb used was obtained from Amgen's manufacturing facility in Thousand Oaks, CA. The mAb formulation (160 mg/mL) was diluted and buffer-exchanged immediately before use into the respective buffers using a GE Sephadex G-25 desalting column.

The chromatography experiments were performed on an Äkta Pure workstation (GE Healthcare, Uppsala, Sweden). Glass columns (Omnifit, Diba Industries Inc., CT) of inner diameter 0.3 cm and length 5 cm (volume 0.353 mL) were first slurry-packed (50% slurry) with chromatographic resin in deionized water. The resins evaluated were Fractogel SO₃⁻ M-type (Merck, KGaA), including variants with different ligand densities, Toyopearl SP-650M (Tosoh Bioscience, PA) and Sepharose Fast Flow (GE Healthcare, Chicago, IL). Fractogel SO₃⁻ resin particles are methacrylate-based polymeric beads with attached linear polymer chains ("tentacles") that carry the functional ligands. The physical properties of the standard Fractogel M-type resin are presented in Table 4.1, while the ligand densities of the variants are presented in Table

4.2. Toyopearl® SP–650 M is similar to the base matrix of Fractogel SO₃⁻ resin without the grafted tentacles. Sepharose Fast Flow is an agarose-based resin without grafted polymer chains.

Table 4.1 Properties of Fractogel SO₃⁻ M-type resin.

Particle size	40-90 μm (Merck KGaA)
Mean pore diameter	~ 800 Å (Merck KGaA)
Packing void volume (ϵ_c)	~ 0.4 (experimentally determined)
Intraparticle porosity (ϵ_i)	0.68 (Zhang et al., 2017)
Average tentacle length	~ 100 Å
Density	1.43 g/cm ³ (Merck KGaA)

Table 4.2 Ligand densities of Fractogel SO₃⁻ M-type variants.

Ligand density variant	Ligand density (μeq/g dry resin)
Low	395
Standard	541
High	645

4.2.2 Methods

4.2.2.1 Chromatography methods

The column was first equilibrated with buffer A (sodium acetate buffer, either 100 or 155 mM ionic strength (IS)) at pH 5.0 or 5.5 on an Äkta Pure chromatographic workstation. Bind-and-elute measurements were then performed by loading the mAb solution (3-6 mg/mL) either isocratically in buffer A or across an optimized gradient of 0-100% B over 60-130 column volumes, where buffer B was the same as buffer A but at 35 or 70 mM IS. The flow rate for all operations was 0.17 mL/min. Sample

loading was continued until protein breakthrough and stopped when the outlet mAb concentration was > 95% of the feed concentration. The column was then washed with 100% buffer B until the UV 280 nm reading reached a stable baseline of < 20 mAU, then the bound mAb was eluted with one column volume of buffer B with 300 mM added NaCl. The column was regenerated and sanitized with 1 M NaCl and 0.5 M NaOH, respectively, after every run. The data from these experiments were used for model validation and parameter estimation for various loading and elution conditions.

4.2.2.2 Mechanistic modeling of chromatography

A mechanistic model that can accurately simulate chromatographic separations was employed for efficient optimization of the gradient loading approach and for parameter estimation. Among the available models, the general rate model (Carta and Jungbauer, 2010) was chosen because of its generality in accounting for convection, axial dispersion, external mass transfer to and from the particle and diffusive transport inside the particle (Figure 4.1). The governing equations are protein mass balances in the column's interstitial space, for a column of length L ,

$$\frac{\partial c_i}{\partial t} = -u \frac{\partial c_i}{\partial z} + D_{ax} \frac{\partial^2 c_i}{\partial z^2} - \frac{1-\epsilon_c}{\epsilon_c} \frac{3}{r_p} k_{film,i} [c_i - c_{pi,r=r_p}] \quad \text{for } t \geq 0, z \in [0, L] \quad (4.1)$$

and in a porous bead of radius r_p ,

$$\frac{\partial c_{pi}}{\partial t} = D_{pi} \left(\frac{\partial^2 c_{pi}}{\partial r^2} + \frac{2}{r} \frac{\partial c_{pi}}{\partial r} \right) + D_{si} \frac{1-\epsilon_i}{\epsilon_i} \left(\frac{\partial^2 q_i}{\partial r^2} + \frac{2}{r} \frac{\partial q_i}{\partial r} \right) - \frac{1-\epsilon_i}{\epsilon_i} \frac{\partial q_i}{\partial t} \quad \text{for } t \geq 0, z \in [0, L] \text{ and } r \in [0, r_p] \quad (4.2)$$

Here c_i , c_{pi} and q_i denote the concentration of solute i in the interstitial space, the pore space, and adsorbed on the solid phase, respectively. The external and internal porosities are given by ϵ_c and ϵ_i respectively. D_{ax} and $k_{film,i}$ are the dispersion coefficient and the mass transfer coefficient to and from the surface of a particle of

radius of r_p while u denotes the interstitial velocity. D_{pi} and D_{si} are the diffusivities within the pore space and on the adsorbent surface, respectively.

The general rate model was coupled with a linear driving force model (Carta and Jungbauer, 2010) to incorporate the kinetics of protein adsorption

$$\frac{dq_i}{dt} = k_{kin} (c_{pi} - c_{pi}^*) \quad (4.3)$$

where k_{kin} is the adsorption rate constant and c_{pi}^* is the concentration of protein in the pore space at equilibrium. To describe the equilibrium partitioning of solute between the liquid and solid phases, protein adsorption was modeled by a colloidal isotherm model (Oberholzer and Lenhoff, 1999)

$$q_i^* = K_{eq} c_{pi}^* \exp\left(-\frac{3 B_{pp} a}{2 R} \exp[-\kappa(R - 2a)](3 + \kappa R)\right) \quad (4.4)$$

Briefly, q_i^* is the protein concentration on the solid at equilibrium, while K_{eq} is the equilibrium binding constant. The exponential factor accounts for protein-protein interactions in the adsorbed phase, where B_{pp} is a protein-protein interaction parameter, κ is the Debye screening parameter, a is the protein molecular radius and R is the nearest-neighbor center-to-center protein spacing on the surface. R is related to the protein concentration on the solid by

$$R = \left(\frac{2\varphi}{\sqrt{3}(q_i^* N_A)}\right)^{\frac{1}{2}} \quad (4.5)$$

where N_A is Avogadro's number and φ the phase ratio. Although the model is formulated for an adsorbed monolayer, the formulation adequately describes the form of isotherms on adsorbents such as Fractogel too.

All simulations were based on the general rate model in combination with the colloidal isotherm and were performed using the Chromatography Analysis and Design Toolkit (CADET 3.1) (von Lieres and Andersson, 2010). The model parameters K_{eq} , B_{pp} and D_s were estimated by fitting breakthrough experiments

performed at different ionic strengths. The estimated parameters at various ionic strengths were fitted to power-law equations to incorporate ionic strength dependence:

$$\ln K_{eq} = k_1 c_0^{k_2} + k_3 \quad (4.6)$$

$$B_{pp} = b_1 c_0^{b_2} + b_3 \quad (4.7)$$

$$D_s = d_1 (\ln K_{eq})^{d_2}$$

(4.8) The parameters k_i , b_i and d_i for various i are constants while c_0 is the ionic strength. The interstitial column porosity was determined from the retention of a tracer, dextran (3000 kDa), that is too large to penetrate the resin particles, while the intraparticle porosity was provided by the manufacturer (Table 4.1). The column dispersion coefficient was estimated from the peak shape of a UV trace obtained by loading a mAb solution under non-binding conditions (500 mM added NaCl). A value of $3.9 \times 10^{-7} \text{ m}^2/\text{s}$ was obtained by fitting the UV trace to CADET simulations. Based on prior experience, external mass transfer was assumed to be rapid, leading to a value of 10^{-4} m/s for the mass-transfer coefficient in all simulations. Other parameters were calculated based on reported correlations (Carta and Jungbauer, 2010).

4.2.2.3 Laser scanning confocal microscopy (LSCM)

Cy3.5 was used to label the mAb following the manufacturer's protocol. The conjugates were buffer-exchanged and the free dye in solution was removed using a Sephadex G-25 desalting column. The labeled protein was reconstituted with unlabeled protein in the appropriate buffer to give 3–6 mg/ml solutions of 3% molar labeling ratio.

Labeled protein was loaded onto a glass column to the dynamic binding capacity (DBC). Protein-loaded resin beds were ejected from the columns by removing the bottom adapter and injecting the appropriate experimental buffer from

the top. The resin slurry was stored at 4 °C for 12-24 hours, after which the samples were visualized by LSCM at 20-23 °C. A slurry droplet of ~ 50 μL was placed on a glass slide and covered with a cover slip. The slide sandwich containing the sample was visualized on an inverted Zeiss 710 confocal microscope using a Zeiss 20× Plan-Apochromat (0.8 numerical aperture) M27 objective, with the coverslip facing the objective. The laser intensity, gain and pinhole were kept constant in visualizing the same protein on different samples for each experiment to allow comparison of intensities. The depth probed along the z -axis was also kept similar ($\pm 2 \mu\text{m}$) to ensure that the densities of collapsed visualizations were comparable.

4.2.2.4 Small-angle neutron scattering (SANS)

4.2.2.4.1 Background

SANS probes structural details of a sample in the approximate range of length scales of 10-1000 Å. The collected intensity $I(q)$ of the scattered neutrons at an angle 2θ from the incident beam is, for elastic scattering, a function of the momentum transfer vector,

$$q = \frac{4\pi}{\lambda} \sin(\theta) \quad (4.9)$$

where λ is the wavelength of the neutrons. The magnitude q is related to the length scale probed, L , by Bragg's Law

$$L = \frac{2\pi}{q} \quad (4.10)$$

In the case of independent scatterers, the intensity I can be written as (Sivia, 2012)

$$I(q) = (\Delta\rho)^2 v^2 P(q) S(q) + B \quad (4.11)$$

where $\Delta\rho$ is the contrast in the scattering length density (SLD) of the material and the background, v is the scattering volume, $P(q)$ is the form factor, which characterizes the

shape of individual scatterers, and $S(q)$ is the structure factor, which describes the interactions among scatterers. B is the background scattering, which is generally independent of q and does not contain structural information but may contain information about the overall composition of the sample. In particular, B often indicates the hydrogen content in the sample as hydrogen atoms have a large incoherent-scattering cross-section. The background scattering is determined by fitting the raw spectrum to the Porod scaling for flat interfaces at large q (Deniz, 2007):

$$I(q) \cdot q^4 \propto A + B \cdot q^4 \quad (4.12)$$

where A is a constant proportional to the surface-to-volume ratio of the sample.

4.2.2.4.2 Sample preparation

Samples of chromatographic resins were investigated using SANS both without and with adsorbed protein. The samples with adsorbed protein were taken from column experiments to ensure comparability with other measurements reported here. To prepare each column, nine column volumes of water were passed through the column followed by nine column volumes of sodium acetate buffer of appropriate IS and pH. The experimental buffers were prepared using deuterium oxide (D, 99%), acetic acid-D4 (D, 99.5%), sodium acetate anhydrous and sodium chloride.

The mAb was loaded at 0.17 mL/min under several different solution conditions. For the standard ligand density resin, 3 mg/mL of mAb was loaded isocratically at 155, 112.5 and 70 mM IS and across a decreasing concentration gradient of 3-0 mg/mL and a simultaneous decreasing IS gradient of 155-70 mM over 60-130 column volumes, all at pH 5. Similarly, the mAb was loaded isocratically at 35 and 55 mM IS and across a 55-35 mM IS gradient onto the low ligand-density resin, and isocratically at 35 and 100 mM IS and across a 100-35 mM IS gradient onto the

high ligand-density resin, all at pH 5.5. Control resin samples without protein were analyzed at 155, 112.5 and 70 mM IS for the standard ligand-density resin and at 70 mM IS for the low and high ligand-density samples.

After column loading, the resin beds were ejected from the glass columns as previously described. Samples were stored at 4 °C for 24-48 hours, then placed into quartz window cells with a path length (thickness) of 1 mm for SANS analysis.

For measurement of the mAb form factor (section 4.2.2.4.5), a mAb solution of 7.4 mg/mL in sodium acetate deuterium oxide buffer of pH 5.0 was prepared by exchanging the mAb from an aqueous buffer into the deuterium oxide buffer using a GE Sephadex G-25 desalting column. The desalting column and the Äkta workstation were equilibrated in the deuterium oxide buffer prior to protein loading.

4.2.2.4.3 Data collection

SANS experiments were conducted at the National Institute of Standards and Technology's National Center for Neutron Research in Gaithersburg, MD, using the 30 m NG7 SANS instrument. The diffractometer settings are shown in Table 4.3.

Table 4.3 Diffractometer settings. The wavelength spread was approx. 12%.

	Sample-to-detector distance (m)	Neutron wavelength (Å)	Count time (s)
High q	1	6	300
Intermediate q	4	6	900
Low q	13	6	1200

Raw data were reduced using IGOR Pro following standard procedures (Kline, 2006). Reduction involves correcting the data for background and empty-cell scattering, scaling the intensity and averaging the 2D data circularly to obtain data in the form of $I(q)$ vs. q . Data from the three scattering ranges were then spliced together to give a collective range of $0.004 \text{ \AA}^{-1} < q < 0.5 \text{ \AA}^{-1}$, which corresponds to a range of $\sim 13\text{-}1500 \text{ \AA}$ in length scale.

4.2.2.4.4 Structural models

The collected SANS spectra were fit to various standard models to obtain quantitative structural information about the chromatographic resin with and without adsorbed protein. Individual models for shapes such as polydisperse spheres, core-shell spheres, monodisperse flexible cylinders, cylinders with polydisperse radii, and core-shell cylinders with polydisperse radii did not fit the scattering spectra of the neat resin and hence do not describe the neat resin's structure adequately. On the other hand, a fuzzy sphere model fit the scattering spectra but was unnecessarily elaborate. The sum of a polydisperse spheres model and the Lorentz model, which we term the sum model, was the simplest model that provided a good fit. Although a good fit does not ensure a good physical model, our physical knowledge of the resin structure and properties and the alignment between our SANS model interpretation and the outcomes from the chromatography and LSCM experiments together make a strong case for using the proposed sum model to interpret the scattering data. Hence, in view of the lack of good fits using other, similar models, we use the sum model to describe the average three-dimensional structure of the neat resin on length scales ranging from $1500\text{-}13 \text{ \AA}$.

The polydisperse hard-sphere model (Griffith et al., 1987) is used to calculate the scattering intensity for a population of polydisperse spheres with uniform scattering length density, allowing for hard-sphere interactions among them. In this model, the polydispersity of the spheres is represented by a Schulz distribution and the partial structure factors contain information about the distribution of distances between spheres of various sizes. The scattering intensity is given by

$$I(q) = n \int_0^\infty F_i^2(q) f(\sigma_i) d\sigma_i + n \int_0^\infty \int_0^\infty F_i(q) F_j(q) H_{ij}(q) f_i(\sigma_i) f_j(\sigma_j) d\sigma_i d\sigma_j + B \quad (4.13)$$

where $f(\sigma_i)$ and $f(\sigma_j)$ are the distribution functions of particle i and j respectively. The first term stems from the square of the modulus of the molecular form factor, $F^2(q)$, and the distribution of radii, $f(\sigma_i)$, where σ^2 is the variance of the distribution. The second term stems from the distribution of partial structure factors, $S_{ij}(q)$, arising from pairwise combination of partial pair-correlation functions describing sets of separations between differently-sized particles. The $H_{ij}(q) = S_{ij}(q) - 1$ are the partial distribution functions, related to the partial structure factors. The polydisperse hard-sphere model accommodates six parameters: the mean radius, polydispersity, volume fraction (φ), SLD of the sphere, SLD of the void and the background B . The SLDs of the two phases comprising the polydisperse hard-sphere model affect the scaling of the spectrum but not its shape, while the sphere mean size, polydispersity and perhaps the void volume, in the presence of interactions among the spheres, impact the shape of the scattering spectrum.

Since the polymer forming the chromatographic media is not simply composed of a solid phase but rather consists of a network of polymeric strands or a hydrogel, as

indicated by the name “Fractogel”, the Lorentz model (Debye et al., 1957; Debye and Bueche, 1949)

$$I(q) = \frac{I(0)}{[1+(q\xi)^2]} + B \quad (4.14)$$

is combined with the hard-sphere model to impart additional structural features describing the network. The Lorentz model represents the scattering due to fluctuations arising from a gel network with a flat background scattering contribution B , where $I(0)$ is the scale factor and ξ is the correlation length or the average mesh size. The three parameters of the Lorentz model are the scale factor $I(0)$, the correlation length ξ and the background B .

Since the two background terms are combined, the sum model contains a total of 8 fitting parameters; a structural depiction of the model is shown in Figure 4.2. In the context of our experimental data pertaining to the resin, the spheres represent the pore space within the approx. 100 micron-sized resin particles while the void space represents the polymer matrix. It is worth noting that in the sum model, the scattering contributions from the polydisperse hard spheres and the Lorentzian network are added. Although one cannot discern whether the Lorentzian network exists in the pores (spheres) or polymer matrix (void space), for the mathematical formulation of the model due to Babinet’s principle (Sivia, 2012), attributing the Lorentzian network to the polymer backbone makes physical sense since density fluctuations exist in polymer networks (Shibayama, 1998).

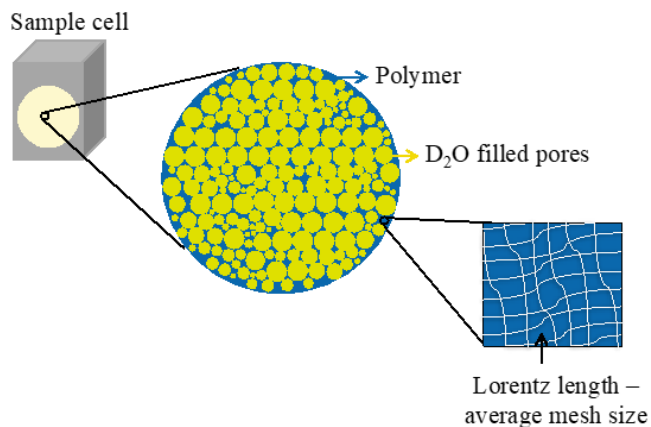


Figure 4.2 Schematic of the sum model. Figure not to scale.

4.2.2.4.5 IgG1 form factor

In the case of proteins, the form factor $P(q)$ is the scattering spectrum arising from the shape of the protein molecule while $S(q)$ arises from correlations in the positions of different protein molecules resulting from local interactions. In a dilute solution of monomeric native proteins, the positional correlations are negligible and hence $S(q)$ goes to 1, making it possible to obtain $P(q)$ directly from the scattering spectrum. The 7.4 mg/mL mAb solution, prepared as described in section 4.2.2.4.2, was used for this purpose. The approximate scattering spectrum of the mAb was also computed using an appropriate Protein Data Bank (PDB) (Berman et al., 2002) file (PDB ID 1IGY) for an IgG1 (Harris et al., 1998), which is physically representative of a mAb, within CRYSON (Svergun et al., 1998).

4.2.2.4.6 Model fitting of resin scattering data

Because the scattering intensity scales linearly with the total sample volume, the scattering from the column interstitial void volume, which is on a length scale O (10-100s of μm) and so much larger than the length scales probed by SANS, does not

contribute significantly to the collected intensity. Therefore, in fitting the scattering spectra to the sum model, a reasonable simplifying assumption was made, which was to scale the intensity of the spectra by the interstitial void fraction of the packed column. This scaling treats the scattering volume as a block of material in the dimension of the sample cell with the same internal structure as the resin beads. This procedure simplifies further parameter estimation.

The sum model was directly fit to the neat resin using IGOR Pro's NCNR Analysis Macros. In fitting to the sum model, three of the eight fitting parameters, the background, the sphere/pore volume fraction and the sphere/pore SLD, were determined respectively from the background determined from Porod analysis described in section 4.2.2.4.1, the neat resin intraparticle pore volume fraction (Zhang et al., 2017) and the SLD of D₂O, calculated using the NCNR SLD calculator (Brown and Kienzle, 2015). Physically-meaningful values of the remaining five parameters were obtained by fitting the neat resin spectra to the sum model. The mean pore radius obtained from the fitting coincides closely with the vendor-provided mean pore radius (Table 4.1). The SLD of the deuterated matrix was found to be $3.88 \times 10^{-6} \text{ \AA}^2$, which is within 15% of the reported SLD (Dunne et al., 2017) of D₂O-exchanged maltose binding protein and matches the SLD of poly(methyl methacrylate) calculated using the NCNR SLD calculator (13) assuming a ~ 47% fraction of D₂O in the polymer network.

The values of the five parameters determined from fitting the neat resin samples were held fixed in fitting the scattering spectra for the protein-adsorbed resin samples, as were the background and the SLD of D₂O. Therefore, in fitting the spectra

for the protein-adsorbed samples, the only parameter that was treated as adjustable was the sphere volume fraction.

4.3 Results and discussion

4.3.1 Surface diffusivity of a protein depends inversely on its binding strength

Although qualitative confirmation of the importance of surface diffusion in protein chromatography is provided by confocal microscopy observations, quantitative estimates of D_s are best obtained by fitting column data to mechanistic models. Models that account only for pore diffusion provide acceptable uptake predictions for small proteins such as lysozyme (Gallant et al., 1996) and cytochrome c (Figure 4.3A, B) but not for mAbs ((Kumar et al., 2015) and (Figure 4.3C, D)). Incorporation of surface diffusion leads to a more accurate prediction of protein uptake (Figure 4.3B, D), including of mAbs, and allows D_s to be estimated. Fitted surface diffusivities for a mAb on Fractogel SO_3^- at various pH values are plotted in Figure 4.4A and show a systematic increase with increasing IS, consistent with prior reports (Basconi et al., 2014; Feller et al., 2010; Lenhoff, 2008). The same data plotted against the adsorption equilibrium constant, K_{eq} , estimated from the same model fits (Figure 4.4C), collapse onto a single curve, indicating that D_s is primarily a function of protein binding affinity. Similar results are obtained for Fractogel variants with different ligand densities (Figure 4.4B, D), although the effect of ligand density is smaller than that of pH. The correlation of D_s with K_{eq} is also consistent across resins with differing architectures, specifically ones lacking the polymer functionalization of Fractogel (Figure 4.5).

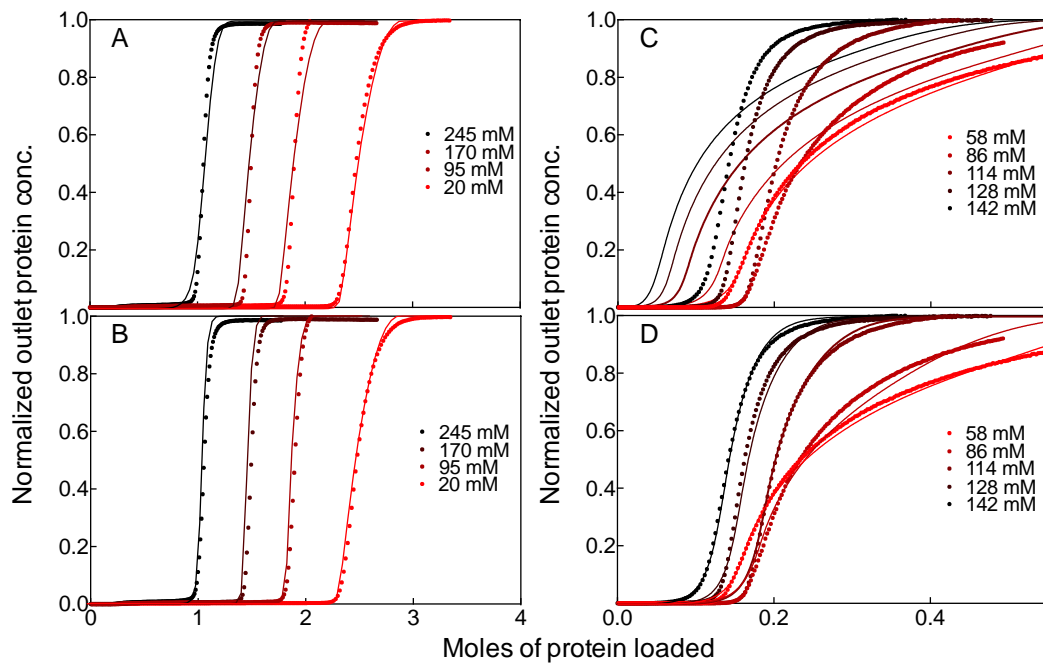


Figure 4.3 Experimental uptake curves for cytochrome c (A, B) and mAb (C, D) and their predictions obtained by fixing (A, C) or varying (B, D) surface diffusivities in the mechanistic model.

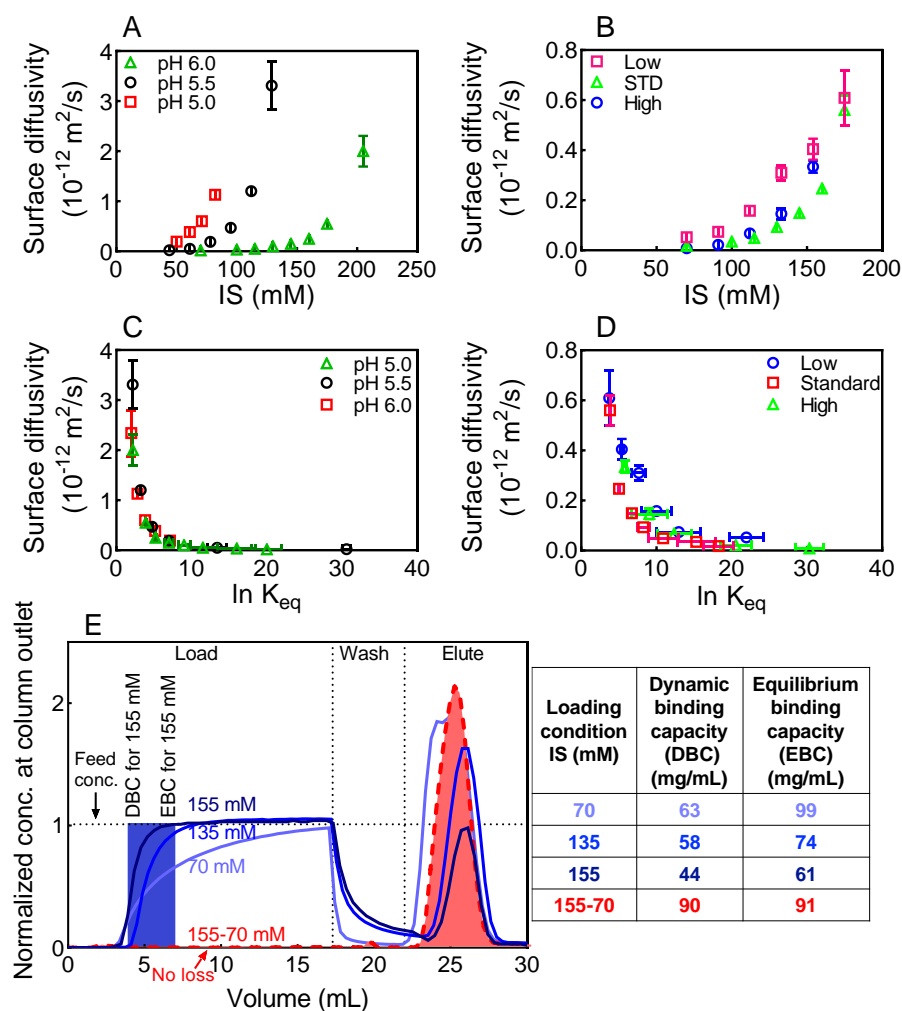


Figure 4.4 MAb surface diffusivities fitted to column breakthrough curves at various pH values (A, C) and resin ligand densities (B, D) are plotted against buffer IS and protein binding equilibrium constant. Data in A and C were for the standard resin and those in B and D were for a buffer pH of 5.5. E) mAb breakthrough and elution curves at 70, 135 and 155 mM IS as well as for a 155-70 mM gradient, all at pH 5. The binding capacities for the samples in E are shown in the table. In panels A and C, black, green and red symbols represent data at pH 6.0, 5.5, and 5.0, respectively. In panels B and D, blue, red and green symbols represent data for the low, standard and high ligand density resins, respectively.

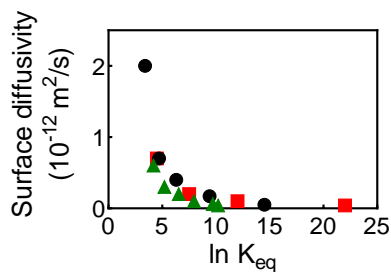


Figure 4.5 MAb surface diffusivities fitted to column breakthrough curves of Fractogel SO_3^- (M), SP Sepharose Fast Flow and Toyopearl SP-650M at pH 5.0 are plotted against protein binding equilibrium constant. Green triangles, black circles and red rectangles represent Fractogel SO_3^- (M), SP Sepharose Fast Flow and Toyopearl SP-650M, respectively.

The dependence of the surface diffusivity on parameters such as IS, pH and resin ligand density is therefore predominantly through their effect on K_{eq} . That the tendency for a protein to diffuse on the adsorbent surface is a function of how strongly it is bound to the surface has been surmised and modeled (Wesselingh and Bosma, 2001) previously, but the direct relationship of D_s to K_{eq} that emerges from our data provides quantitative confirmation. Operationally, the results in Figs. 4.4A and 4.4B show that D_s can be modulated by changing the IS or by using a resin with a different ligand density. The very low values of D_s below 50–70 mM IS reflect the strong adsorption in the absence of significant screening of Coulombic attraction. This effect has been modeled on IEX resins (Lenhoff, 2008; Wesselingh and Bosma, 2001) and observed across enzyme-immobilized substrates (Feller et al., 2010).

In IEX operation, the lower D_s at a lower IS results in slower uptake into particles in the column, as a result of which more protein leaves the column prior to saturation of the resin beads (Dziennik et al., 2005; Harinarayan et al., 2006); this is

seen in the shallowness of the protein uptake curves presented in Figure 4.4E. To avoid unnecessary product loss in preparative operations, the protein feed is usually stopped before this breakthrough occurs and the amount of protein bound at this point is termed the dynamic binding capacity (DBC). The steeper the breakthrough is, the smaller the difference between the equilibrium and dynamic binding capacities. However, the benefit of the sharper breakthrough that results from higher D_s at higher IS is significantly offset by the associated lower equilibrium capacity, shown in the table next to Figure 4.4E.

4.3.2 Loading by a decreasing salt and protein gradient promotes faster and more homogeneous mAb uptake

In order to leverage the relation between D_s and K_{eq} , the binding strength during sample loading was modulated by changing the buffer IS to obtain faster protein surface diffusion initially, but with the final IS low enough so as not to compromise the DBC. Specifically, the IS and the protein concentration in the feed were decreased linearly during sample loading onto the column, with model simulations used to optimize the protein and salt concentration ranges. Using the optimal IS range of 155-70 mM, the experimental protein concentration exiting the column is shown for the mAb at pH 5.0 in Figure 4.4E in red, while the simulated amounts bound to the column are shown vs. column position and time in Figure 4.6A and B for isocratic (constant IS) and gradient loading respectively. The gradient method significantly delayed protein breakthrough (Figure 4.4E) and resulted in a 43% higher DBC than at 70 mM IS, as evident from the larger area under the blue surface at a given time in Figure 4.6B than in Figure 4.6A. Overall, faster and more sustained protein uptake (Figure 4.6B) is achieved compared to that using isocratic

loading (Figure 4.6A) at a lower IS (Bowes and Lenhoff, 2011; Harinarayan et al., 2006; Ljunglöf et al., 2007). This is consistent with a higher D_s value during the early stages of protein loading as a result of the higher IS.

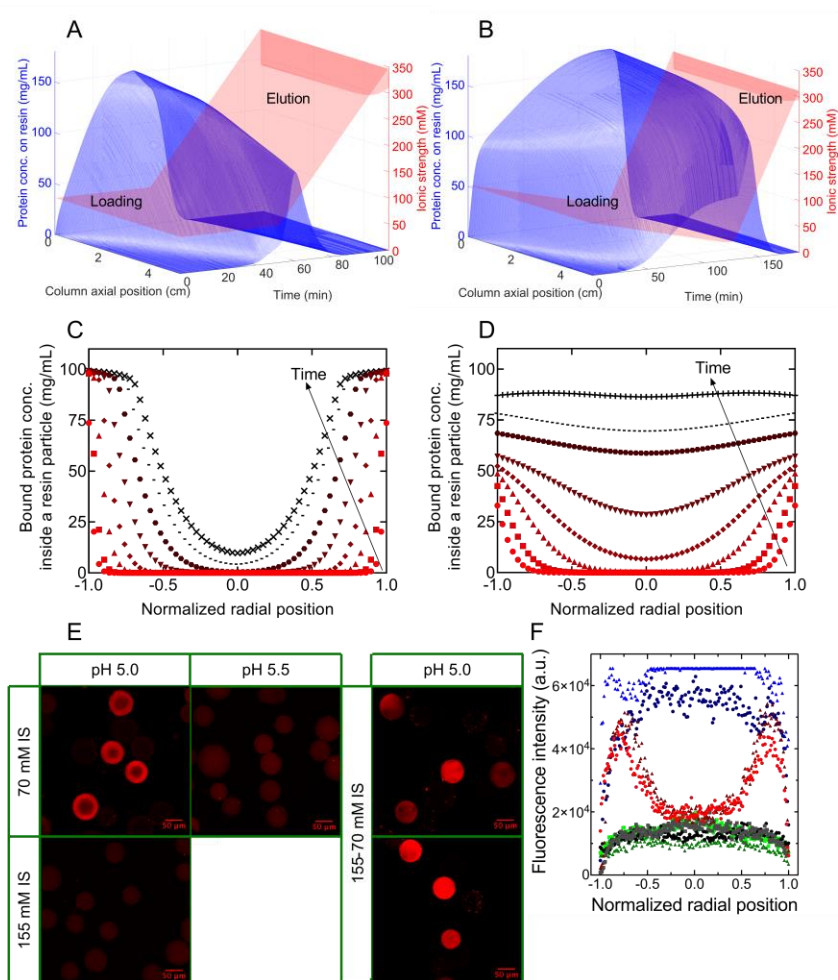


Figure 4.6 Simulated column-bound protein concentrations during sample loading at pH 5 with a buffer IS of 70 mM (A) or a 155-70 mM gradient (B), and subsequent elution, all as functions of time and column axial position. The corresponding simulated bound protein concentrations within individual resin beads at the column entrance are shown in C and D. Resin particles were removed from the column and visualized (E) after loading of fluorescently-labeled protein in an equivalent manner to the simulation. In both simulations and experiments, the mAb was loaded onto the Fractogel SO₃⁻ (M) column until the DBC was reached. The fluorescence intensity profiles for two particles from each image in E are plotted as a function of normalized radial position in F. In panel F, red circles and purple triangle represent 70 mM pH 5.0, dark green triangle and green square represent 155 mM at pH 5.0, grey square and black circle represent 70 mM at pH 5.6, and dark blue circle and blue triangle represent 155-70 mM at pH 5.0.

Characterization of the gradient-loaded resin by confocal microscopy and SANS provides microscopic and nanoscopic information on the intraparticle protein distribution that confirms the role of surface diffusion. Confocal micrographs of resin beads imaged after loading of fluorescently-labeled mAb to the DBC under different conditions are shown in Figure 4.6E. Isocratic loading at low IS (70 mM, pH 5.0) gives rise to a core-shell protein distribution, with very little protein near the center of the particle (18-20). In contrast, loading at high IS (155 mM, pH 5.0) leads to a more uniform protein distribution, but at the cost of a lower total capacity. A similar contrast is seen upon a pH increase from 5.0 to 5.5 at 70 mM IS (Figure 4.6E) because this decreases the mAb's net charge and hence weakens its affinity to the resin, thereby increasing its D_s (Figure 4.4A). Unlike for isocratic loading, gradient-loaded resin beads show the highest amount of bound protein with a quite uniform protein distribution (Figure 4.6E). The radial intensity profiles after protein loading shown in Figure 4.6F are in very good agreement with the corresponding simulated radial protein distributions shown in Figure 4.6C and D, specifically the higher protein concentration or intensity at the shell of the particle when the protein is loaded isocratically at 70 mM IS, with the core remaining undersaturated.

The impact of surface diffusion on the protein distribution was further probed on the nanoscale – structural features 1-100s of nm – using SANS. Briefly, the resin structure was studied with and without adsorbed protein using the coherent scattering contribution arising from the contrast between the D_2O -buffer-filled pores and the hydrogen-containing protein and resin. The scattering spectra of resin beads with and without protein are shown in Figure 4.7A and B before and after subtraction of incoherent background scattering and scaling, respectively. The large incoherent

scattering cross-section of the hydrogen atom dominates the incoherent scattering manifested in the baselines of the spectra. This correlates to the protein content (Figure 4.7A inset) in equivalently D₂O-exchanged samples in which the protein is the variable source of hydrogen.

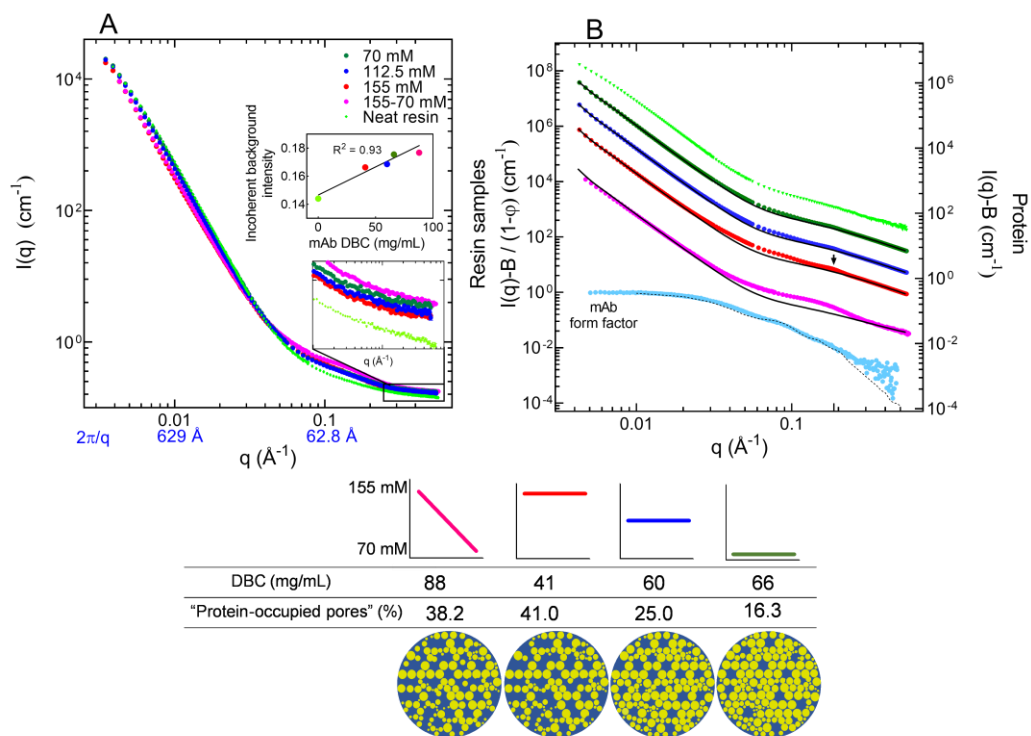


Figure 4.7 SANS spectra for the mAb-loaded Fractogel SO₃ (M) resins. The mAb was loaded onto the resin at 70, 112.5, and 155 mM IS, as well as using an IS gradient of 155-70 mM, until the DBC was reached. The spectra are shown in A with the lower and upper insets showing the background incoherent scattering and its correlation to the DBC, respectively. The length scales corresponding to the q -space are provided in blue below the abscissa. The same spectra after background reduction and scaling are shown in B along with the background-reduced spectrum of 7.4 mg/mL pure mAb (right ordinate). The volume-fraction-adjusted sum model is shown in black lines. The blue dotted curve represents the scattering from a 6 mg/mL mAb solution in 100 mM sodium acetate D₂O buffer of pH 5.0. The dashed line is the scattering spectrum of an IgG1 molecule predicted by CRYSON using the PDB ID 1IGY (Harris et al., 1998). Apart from the mAb solution, successive curves are shifted by a factor of 6 for clarity. The arrows at 0.187 \AA^{-1} point to a peak of which the position is interpreted to indicate the nearest-neighbor distance. The lower part of B shows the DBC and the % loss of "protein-occupied pores" with its depiction.

SANS measurements on the neat resin (Figure 4.8A) showed no detectable changes in resin structure as a function of IS in the range of the chromatographic salt gradient over the length-scale range 13–1500 Å. This is consistent with the small (5%) increase in Fractogel porosity (Thomas et al., 2013) or virtually overlapping small-angle X-ray scattering spectra (Bhambure et al., 2017) reported for buffer IS increases of 500 and 80 mM, respectively. Therefore, changes in the SANS spectra in the protein-loaded samples can be attributed to protein effects, not to the neat resin. A simple yet quantitative interpretation of both the neat resin and protein-loaded samples was obtained by fitting the respective spectra to a physical model based on the sum of polydisperse hard spheres (Griffith et al., 1987) and the Lorentz model (Debye et al., 1957; Debye and Bueche, 1949), representing the buffer-filled intraparticle pores and the hydrated polymer network respectively (Figure 4.2). For the neat resin, this model, termed the sum model, fits the spectra (Figure 4.8B) with physically meaningful parameter values (Table 4.4).

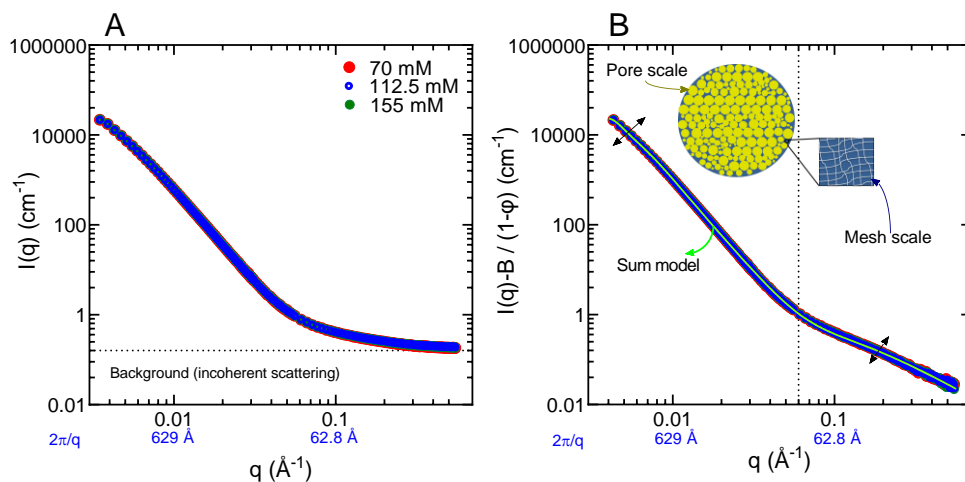


Figure 4.8 A) SANS spectra of neat Fractogel SO_3^- (M) resin in D_2O buffers of 155, 112.5 and 70 mM IS at pH 5.0. The length scales corresponding to the q space are provided in blue below the abscissa. After subtraction of the background indicated in A, the intensity was scaled to $(1 - \text{the interstitial column void volume})$ to obtain the form presented in B. The neat resin scattering spectrum was fitted to the sum model, where the lower- q region is primarily affected by the size of the pores modeled by the polydisperse hard spheres (yellow) and the higher- q region is primarily affected by the polymer mesh network modeled by the Lorentz model (white in blue).

Table 4.4 The sum model fitting parameters for the standard neat Fractogel SO_3^- (M) resin.

Mean pore radius (\AA)	789
Pore radius polydispersity	0.31
Intraparticle pore volume fraction	0.68
SLD of pores (\AA^2)	6.4×10^{-6}
SLD of matrix (\AA^2)	3.88×10^{-6}
Background (cm^{-1})	0.144
Lorentz scale factor	0.49
Lorentz length (\AA)	8.72

The model also fits the spectra for the protein-adsorbed samples in the low- q region ($< 0.03 \text{ \AA}^{-1}$; length scales $> 200 \text{ \AA}$ and therefore comparable to pore sizes) (Figure 4.7B); the key fitting parameter represents the fraction of the "hard-sphere" (pore) volume that is now occupied primarily by protein rather than D_2O . Protein-filled pores attain a similar scattering length density (SLD) to that of the polymer network, hence neutrons detect an effective reduction in the pore volume fraction upon protein adsorption, as illustrated schematically at the bottom of Figure 4.7B. This is reasonable as an SLD within 15% of the fitted value for the resin matrix was reported for a D_2O -exchanged mAb (Dunne et al., 2017). The sum model takes a binary view of a pore as either "empty" or "filled" for ease of analysis. Although realistically there is a gradient between empty and filled states, this approach allows the sum model to enable quantitative analysis of SANS data to obtain insights into the protein distribution on the pore scale.

Comparing the fitted fraction of protein-filled pores for the isocratic loading experiments at three different IS values shows that the fraction varies inversely with DBC. Therefore, pore occupancy reflects not the total protein loading but rather the distribution of protein within the beads, which is less uniform at lower IS values, i.e., when surface diffusion is slower. This distribution on the pore level is consistent with the inference from the confocal microscopy data, e.g., the core-shell adsorption pattern seen at 70 mM (Figure 4.6E) is manifested as low pore occupancy in the SANS data. Therefore the confocal micrographs, SANS spectra and column simulations all demonstrate that the higher the surface diffusivity during loading, the more uniform the protein distribution that is seen at the column (cm), bead (tens of μm) and pore (tens of nm) length scales. The gradient loading combines this surface diffusion effect

with the increased equilibrium capacity at lower IS, resulting in 2.3 times higher pore occupancy than for the 70 mM sample, with a 43% higher DBC.

The higher q regions of the SANS spectra indicate additional features of the protein distribution. The discrepancies in the fits in Figure 4.7B between 0.03 and 0.3 \AA^{-1} (209-20.9 \AA) reflect the scattering from the individual protein molecules and their arrangement with respect to one another, which is not accounted for in the sum model. The sum model accounts for the presence of protein only via the contribution of the protein-filled pores. The individual molecules ($\sim 137 \times 83 \text{\AA}$ (Tan et al., 2008)) collectively contribute to the scattering intensity through their shape via the form factor, shown by the light blue (measured) and black dashed (computed) lines in Figure 4.7B. These contributions may be modulated by inter-protein correlations, termed the structure factor, which may be significant given the mAb loadings of 44-90 mg/mL, with actual local concentrations effectively much higher. Indeed, the scattering spectrum of the sample with the highest local protein density and potentially largest inter-protein correlations, from loading at 70 mM IS, seemingly deviates the least from the model fit between 0.03-0.2 \AA^{-1} (Figure 4.7B), probably due to the masked form factor. A subtle peak at 0.186 \AA^{-1} on the 155 mM sample (arrow in Figure 4.7B) suggests a prominent nearest-neighbor distance of 34 \AA between the mAb molecules, similar to the 37 \AA reported for mAb-sorbed chromatographic resins (Koshari et al., 2018) and the 31 \AA reported for a frozen 171 mg/mL mAb solution (Curtis et al., 2012). Given that the radius of gyration of a typical mAb is 48 \AA (Castellanos et al., 2016; Yearley et al., 2014), an interprotein distance of 34 \AA suggests interdigitation of subunits (Castellanos et al., 2016). The equivalent peak for the gradient loading sample is broader, which may suggest a broader distribution of

nearest-neighbor distances, per our hypothesis that the gradient method promotes mAb surface diffusion in the resin bead. A broad distribution of protein spacing in a chromatographic resin with a large surface area may mitigate surface-mediated (Guo and Carta, 2015; Voitl et al., 2010) and self-associated (Bethea et al., 2012; Esfandiary et al., 2013; Liu et al., 2005; Luo et al., 2014; Nishi et al., 2010) protein conformational changes.

4.3.3 The leverage provided by manipulating surface diffusion increases with increasing protein size and affinity

The utility of the gradient loading method was evaluated for two different proteins and for a set of resins differing in ligand density (Table 4.2), which has been shown to affect the adsorption affinity (Bhambure et al., 2017). Our hypothesis was that situations in which baseline transport rates were lower – larger proteins with lower free-solution diffusivities and systems with higher adsorption affinity – would benefit more from the gradient loading method.

The behavior of the mAb studied above was investigated on ligand-density variants of the same Fractogel resin used previously (Bhambure et al., 2016; Bhambure et al., 2017). Figure 4.9A and B show SANS spectra for the neat and mAb-laden low- and high-density variants, with the mAb-laden samples prepared using both isocratic and gradient loading, albeit over different IS ranges; the optimal IS range is narrower for the low-density resin because less screening is needed to modulate the weaker adsorption. For the high-density resin (Figure 4.9B) at 35 mM IS, the neat and mAb-laden spectra nearly overlap. The lower surface diffusivity in the high-density case produces a core-shell adsorption structure with adsorption mainly around the bead periphery, so the central core of the bead retains the character of the neat resin.

This rationale is consistent with the lower surface diffusivity reported for strongly-adsorbed amyloid β peptide on highly hydrophilic surfaces (Shen et al., 2012). In contrast, with gradient loading, the spectrum of the mAb-laden sample deviates significantly from that of the neat resin and 3.5 times more mAb is taken up than at 35 mM IS, showing the appreciable benefit due to the enhanced surface diffusion.

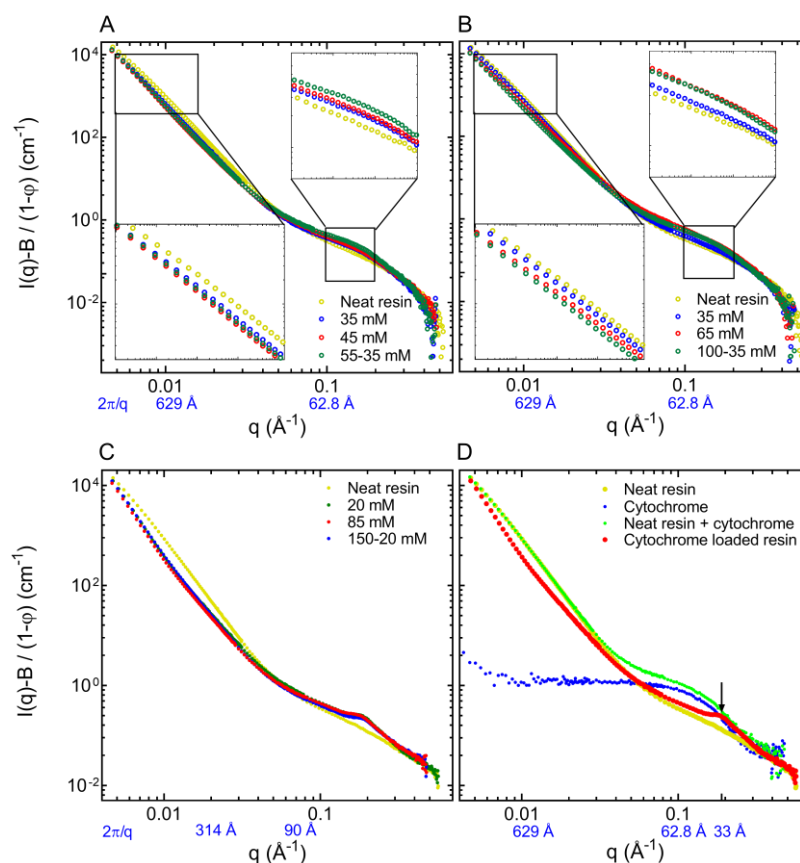


Figure 4.9 SANS spectra after background subtraction and scaling are shown for the mAb-loaded resins of low (A) and high (B) ligand densities, and cytochrome c-loaded resins (C, D) of high ligand density. The length scales corresponding to the q values are provided in blue below the abscissa. MAb masses of 22.4, 29.4 and 45.4 mg were loaded per mL of low ligand density resin (A) using buffer IS of 35 mM, 45 mM, and a gradient of 55-35 mM at pH 5.5, respectively, until the DBC was reached. (B) Similar data sets at pH 5.5 are shown for the high ligand density resin with mAb (B) loaded at 35 (13.6 mg/mL), 65 (31.4 mg/mL) and 100-35 mM (46.8 mg/mL) IS, and with cytochrome c (C) at 20 (65.4 mg/mL), 85 (75.6 mg/mL) and 150-20 mM (73.5 mg/mL) IS. (D) The scattering spectrum for cytochrome c (65.4 mg/mL of resin) loaded resin at 20 mM IS is shown in red, while the separate spectra for the neat resin and the cytochrome c solution (65.4 mg/mL) are shown in yellow and blue, respectively. The mathematical sum of the spectra for the neat resin and the cytochrome c solution is shown in green. The arrow points to a pronounced peak, the position of which is interpreted to be indicative of the nearest-neighbor distance.

For the low ligand-density resin, in contrast, all modes of protein loading (Figure 4.9A) result in overlapping spectra in the low- q region, indicating less promotion of protein surface diffusion during gradient loading in this situation of lower binding affinity. In the high- q regions ($< 200 \text{ \AA}$), where the presence of protein molecules and interactions among them contribute to the scattered intensity (Curtis et al., 2012; Koshari et al., 2015; Koshari et al., 2018), the nearest-neighbor peak between 126 and 29 \AA grows with increasing protein content in the different samples, suggesting similar protein spatial distributions. However, the corresponding peak ordering does not depend on protein content for the high-density case as protein distributions differ among samples due to differences in surface diffusion during sample loading.

The benefit gained by manipulating protein surface diffusion depends on its contribution to mass transport relative to that of protein diffusion in the fluid-filled pore space. While the surface diffusivity depends on the binding affinity, the pore diffusivity follows the free-solution diffusivity in varying inversely with the protein hydrodynamic radius, except if pore constriction is severe. SANS spectra of cytochrome c-laden samples on the high ligand-density resin acquired after loading to the DBC using the isocratic and gradient methods (Figure 4.9C) are all similar, in contrast to the mAb-laden samples (Figure 4.9B). Cytochrome c is smaller than a mAb by about a factor of ten in molecular mass and about a factor of three in hydrodynamic radius, giving it much higher free-solution and pore diffusivities. As a result, pore diffusion appears adequate to lead to a fairly uniform intraparticle distribution even in the absence of enhanced surface diffusion. The effect of protein size on intraparticle distribution was also seen for thyroglobulin (660 kDa), which adsorbed predominantly

at the particle surface (Zhu et al., 2018) due to limited mobility at a low IS but adsorbed more homogeneously at a higher IS.

The deviations in Figure 4.9C between the spectra for the protein-laden and neat samples are evaluated systematically in Figure 4.9D, for the sample loaded at 20 mM IS. The protein form factor corresponding to the amount of bound cytochrome c (blue) is added to the spectrum for the neat resin (yellow) and plotted along with the experimental spectrum (red). The experimental spectrum is lower in the low- q region because the adsorbed cytochrome c augments the resin's fractal features in the 200-1500 Å length-scale range; this effect is opposite to that reported for lysozyme adsorbed in S HyperCel™ (Koshari et al., 2015; Koshari et al., 2018), a resin with a significantly different architecture. In the high- q region, a clear peak at a nearest-neighbor spacing of ~ 33 Å is present for all three protein-laden samples in Figure 4.9C. The similar intermolecular spacing at different sample loading conditions supports our rationale that the higher pore diffusivity of cytochrome c reduces the dependence of transport properties on the binding affinity because of the reduced importance of surface diffusion.

4.4 Conclusions

The absence of a consensus regarding the role of surface diffusion in IEX of proteins is likely due in part to the variability of the surface diffusivity with solution conditions. We have shown that the surface diffusivity is a function of the adsorption equilibrium constant K_{eq} , independent of the buffer IS and pH and the resin ligand density. We have furthermore exploited this finding by introducing a novel method of column loading in which transient manipulation of the buffer IS can allow an appreciable increase in the protein surface diffusivity and hence in the protein

saturation efficiency and resin utilization. The resulting increase in DBC of as much as > 40% allows loading up to near the equilibrium binding capacity. Confocal microscopy and SANS measurements provide complementary evidence that the DBC increase is accompanied by improved and more homogeneous adsorbent utilization. A more widespread spatial distribution of adsorbed mAb, particularly in a resin such as Fractogel in which additional adsorption capacity has been introduced by polymer functionalization, may result in a reduction in surface-mediated (Guo and Carta, 2015; Voitl et al., 2010) and self-associated (Bethea et al., 2012; Esfandiary et al., 2013; Liu et al., 2005; Luo et al., 2014; Nishi et al., 2010) conformational changes. The results presented here provide an indication of where the new approach can have the most impact, namely for larger proteins under high-affinity binding conditions that are amenable to attenuation by manipulation of the solution conditions. Our observations and broadly applicable approaches can help evaluate systems where protein-adsorbent interaction is mass-transfer limited, such as other adsorptive systems, biointerfaces and biosensors. Beyond capturing the structural features at the end of uptake as has been done here, of particular value would be distinguishing pore and surface diffusion mechanisms in situ in the pore space in real time.

Chapter 5

MULTI-COLUMN DISPLACEMENT CHROMATOGRAPHY FOR SEPARATION OF CHARGE VARIANTS OF MONOCLONAL ANTIBODIES

5.1 Introduction

Displacement was classified as one of three forms of chromatography, together with elution and frontal chromatography, in 1943 (Tiselius, 1943). Separation via elution chromatography is achieved after all components of the sample first bind to the column, then are eluted sequentially in the order of increasing affinity by a buffer of gradually increasing eluent strength. It does not achieve maximum throughput because the sample mass should not exceed the dynamic binding capacity of the column. In addition, the resolution decreases with increasing sample mass. Furthermore, elution chromatography does not exploit the displacement that naturally occurs due to competitive adsorption during loading. On the other hand, frontal chromatography is difficult to adapt for mixtures of more than two proteins. Because the purification of therapeutic proteins such as monoclonal antibodies (mAbs) requires effective removal of many impurities such as host-cell proteins (HCPs), nucleic acids, and leached resin components, a combination of various advantages from each method is desirable.

The heterogeneities in the mAb product further complicate its purification. Although a therapeutic protein is often considered a single entity for simplicity, it is a distribution with variations in amino acid sequence (Li et al., 2016; Parker et al., 1978; Santos and Tuite, 1993; Tan et al., 2012), higher-order structure and chemical and enzymatic modifications (Griaud et al., 2017). Modifications such as deamidation,

sialylation, C-terminal lysine cleavage and glycation give rise to acidic mAb variants while glycine amidation, succinimide formation and amino acid oxidation can give rise to basic mAb variants (Khawli et al., 2010). These mAb charge isoforms can be generated during the process (Chung et al., 2018), resulting in product heterogeneity that can reduce drug activity (Müller-Späth et al., 2010). The rise of biosimilars of mAbs has renewed the interest in charge variants, as biosimilars are required to have charge variant compositions that match those of the innovator product (Xiao et al., 2018). When a similar charge variant profile to that of the innovator product is not obtained in cell culture, modifications are often made in downstream purification to adjust the composition (Brühlmann et al., 2015).

Ion-exchange chromatography, particularly cation-exchange (CEX), is a unit operation with the potential to separate charge variants using gradient elution methods (Guélat et al., 2012). Although partial separation is feasible at the preparative scale, the resolution is often poor and requires peak fractionation and product pooling to obtain the desired charge variant profile of the product (Kumar and Rathore, 2017). This reduces the yield of the process and increases batch-to-batch variability. The development of ion-exchange processes that include charge variant selectivity is cumbersome owing to the large number of parameters that require optimization, including pH, buffer type and concentration, resin backbone, gradient length and column loading (Kumar et al., 2015); the column format can also be replaced by a membrane ion exchanger (Sadavarte et al., 2018). Furthermore, prior research efforts in charge variant purification have been limited mainly to analytical separations.

Some previous efforts to enhance charge-variant selectivity during elution include optimization of multi-salt gradients to help increase resolution (Kumar and

Rathore, 2017) and pH gradient optimization to help increase peak fraction purity (Farnan and Moreno, 2009). In a more complex practice, hybrid gradients of salt and pH were employed to increase the purity of the eluted product (Lee et al., 2015; Zhou et al., 2007). Despite these efforts, baseline peak separation with a reasonable yield is difficult to achieve.

Transitioning from a single column to two smaller columns and recycling the unbound impurities increases the yield and purity (Persson et al., 2018). Operating the multicolumn setup in a quasi-continuous manner, termed multicolumn solvent gradient purification, alleviates the purity-yield trade-off and allows for the steady enrichment of native variants to a high yield (Müller-Späth et al., 2008). However, despite the effort and optimization required to design and run these methods, they do not optimize for the displacement that occurs during loading and allow the full capacity of the ion exchanger to be exploited. Furthermore, these patented methods recommend new chromatographic work stations that may not be readily available.

Chromatographic operation in displacement mode, on the other hand, benefits from loading up to the saturation capacity of the column (Agner, 2003; Frenz and Horváth, 1985). Product charge variants have been separated with a commercially-available high-affinity displacer, which displaces the transiently-bound product from the column (Zhang et al., 2011). However, the residual displacer contaminating the product pool proves to be a challenge with this method. Furthermore, the cost associated with using displacer molecules at a large scale can make the method uneconomical.

A variant of displacement chromatography, sample displacement chromatography, has also emerged (Liu and Tang, 2008). Here more strongly-binding

product variants are used as displacers, thus avoiding the need to clear the displacer from the product downstream. Sample displacement or self-displacement has been applied to the purification of small molecules such as peptides on reverse-phase columns or proteins on anion-exchange columns (Kotasińska et al., 2012; Srajer Gajdosik et al., 2012; Veeraragavan et al., 1991). The optimization of the loading parameters to obtain a high resin capacity can be a challenge using self-displacement chromatography in batch mode, given the variability of the charge-variant profiles for different mAb samples.

A better alternative is to merge self-displacement with elution chromatography to obtain various advantages from each method. Such an approach can be realized with a multi-column system in which the charge variants and native product can be captured on different columns (Hodges et al., 1991). Although multi-column self-displacement chromatography can be utilized to separate several small molecules, we are not aware of its application to mAb charge variants. In this work, self-displacement chromatography for the enrichment of mAb charge variants by recycling on a single column or using partial recycling on a three-column set-up is presented. A high yield and purity were achieved by optimizing the loading buffer pH and ionic strength, along with the mass to load, and the use of a dual pH-salt gradient.

5.2 Displacement chromatography principles

In cation-exchange chromatography, protein bound to the resin is usually recovered by its displacement by sodium or potassium ions; the bound protein can also be displaced with an appropriate chemical displacer (Gadam et al., 1995; Gallant and Cramer, 1997). If the displacing moiety is a component of the sample, the method is termed self-displacement or sample-displacement chromatography (Frenz and

Horváth, 1985). In the purification of mAbs using CEX, as a general rule-of-thumb, mAb charge variants with a higher positive charge can displace ones with a lower positive charge. However, displacement can occur only if the various components of the sample have different binding affinities to the resin.

The application of displacement in the context of separating charge variants can be better understood by visualizing the events along the length of the column with loading of a two-component sample under conditions that result in relatively strong adsorption and at concentrations that lead to adsorption in the plateau region of the respective isotherms. Therefore, as the sample is continuously fed to the top of the column, the binding capacity of the resin will be reached locally, and the column will become saturated locally and eventually globally. The local strong binding and approach to saturation will give rise to competitive adsorption that results in the component with the higher affinity displacing the component with the lower affinity, initially near the top of the column but progressing along the length of the column. Once the loading is stopped, a heterogeneous distribution of bound sample components – charge variants in our case – will remain along the length of the column. The components with the higher affinity will be located mainly toward the top of the column while those with the lower affinity will be bound mainly toward the bottom of the column.

The development of displacement zones can be simulated using idealized models of chromatography (Frenz and Horváth, 1985), but for charge variants, the development of enriched zones along the length of the column was simulated here using the general rate model with a multi-component Langmuir isotherm (Figure 5.1). Figure 5.1A depicts the bound protein concentration along the length of the column

when the amount of protein loaded is below the capacity of the column. In this case, although the three components bind according to their affinities to the resin, insufficient displacement is observed, as evident from the broadly overlapping zones. When the protein is loaded for a sufficient duration to match or exceed the capacity of the column, the concentration on the solid phase increases and displacement of the weakly-binding red component by the blue and the green (most strongly binding) components is evident in the sharpening of the peaks (Figures 5.1B and C). Figure 5.1 also shows that the displacement is particularly efficient at the top of the column, where the resin is in contact with protein in the mobile phase over a longer period, allowing the component with the highest affinity to displace the components with lower affinities. Furthermore, when the length of the column is increased and the protein is loaded at the capacity of what is now a longer column (Figure 5.1D), the displacement of the red component is further improved. Under conditions of ideal column kinetics, the displacement zones are predicted to be completely resolved (Frenz and Horváth, 1985), but this is not seen in Figure 5.1D because transport and kinetic limitations were included in the simulations. However, the simulation shows the eventual attainment of a largely constant form with migration along the column length.

In an ideal scenario, multiple columns of appropriate length can be connected in series to obtain zones in which different components are enriched in successive columns. These columns may then be disconnected to elute different components separately. However, the dynamics of zone development depend on the adsorption and transport properties of the components under the load conditions, and as is apparent in Figure 5.1, perfectly resolved zones are not attainable in real systems. In particular, if

the different components' affinities to the resin are not highly disparate, the displacement efficiency is compromised. MAb charge variants are usually categorized as acidic, native, and basic variants, although each category comprises a range of broadly similar variants. Unfortunately, the different populations of mAb charge variants differ only slightly in their net charges. Therefore, in this case adjacent components overlap and obtaining discrete zones of each variant along the length of the column is not feasible. Although this gives rise to reduced purity of the recovered products, the enrichment attained may often be sufficient for operational needs.

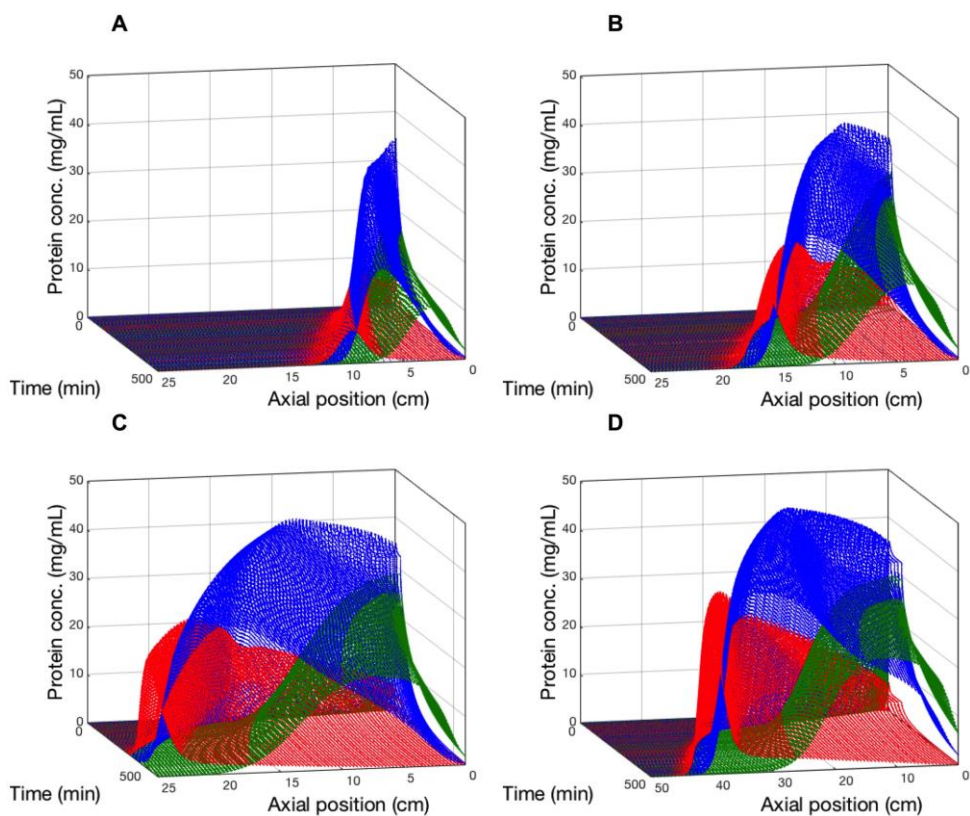


Figure 5.1 Simulations of zone development along the length of the column for a three-component mixture. Red, blue, and green surfaces represent the adsorbed concentrations of the three components. (A) Simulation for a 25 cm column with load below the column capacity. (B) Simulation for a 25 cm column with load at the column capacity. (C) Simulation for a 25 cm column with load above the column capacity. (D) Simulation for a 50 cm column with load at the column capacity.

5.3 Materials and methods

5.3.1 Materials

All chemicals were purchased from Fisher Scientific (Waltham, MA) and were used without further purification. Buffer stocks (0.5 M monobasic sodium phosphate and 0.5 M disodium hydrogen phosphate) were prepared at room temperature (23 ± 2 °C) using deionized water from a Millipore Milli-Q system (>18.2 M Ω ·cm) and were filtered with 0.22 μ m filters. Dilutions were made to obtain molarities of 10 or 15 mM and adjusted to the desired pH by mixing appropriate volumes of the 0.5 M monosodium dihydrogen phosphate and disodium hydrogen phosphate stock buffers. Elution buffers were prepared by adding sodium chloride to 200 mM from a 3 M stock solution to the buffer solutions. Similarly, 50 mM sodium acetate buffer at pH 5.0 with 200 mM sodium chloride was prepared from 1 M sodium acetate and 1 M acetic acid stock solutions.

The mAb sample used was obtained from Amgen's manufacturing facility (Thousand Oaks, CA). The mAb formulation (160 mg/mL) was stored at -80 °C and was diluted immediately before use to 5 to 10 mg/mL and buffer-exchanged into the equilibration buffer. By mixing various variant-enriched peaks obtained from CEX on Poros HS columns, three different compositions of charge variants were generated and termed samples A, B and C. The compositions of the acidic-native-basic variants for

samples A, B and C were 11.4-63.0-25.6, 17.7-65.0-17.2 and 12.3-51.7-36.0, respectively.

5.3.2 Methods

5.3.2.1 Chromatography method

The chromatography experiments were performed on an Äkta Explorer (GE Healthcare, Uppsala, Sweden) with UV and conductimetric detectors and a fraction collector. Omnifit glass columns of I.D. 0.3 cm and length 5 cm (volume 0.35 mL) were slurry (50%) packed with Poros HS 50 μm resin from Applied Biosystems (Foster City, CA). For the single-column set-up, default Äkta connections were used, while for the three-column set-up, connections were modified as shown in Figure 5.2. All the chromatographic runs were at a linear flow rate of 144 cm/hr.

5.3.2.2 Analytical chromatography method

Sample concentrations were measured using a Nanodrop 2000 (Thermo Scientific, Waltham, MA). Analysis of the eluted fractions for charge variants was performed using an Agilent® Bio MAb NP5 column, 4.6 x 250 mm, on a Waters® 2695 HPLC equipped with a UV detector. A loading buffer of 10 mM sodium phosphate, pH 6.8, was used, and samples were eluted using a 30-minute pH gradient from 6.8 to 8.0 at a flow rate of 0.8 mL/min. MAb aggregate was analyzed using an Agilent® AdvanceBio SEC 300 Å column, 4.6 x 150 mm, with 2.7 μm particles using 25 mM sodium phosphate buffer at pH 6.8 with 300 mM NaCl

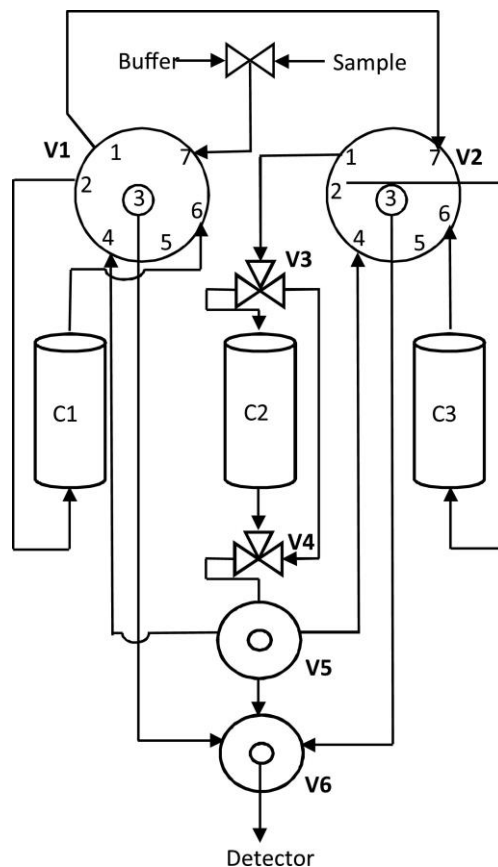


Figure 5.2 Three-column recycling set-up on the Äkta Explorer. The two three-way valves V1 and V2 are the injection and column direction valves, while V3 and V4 are the column position valves and V5 and V6 are the sample and waste valves, respectively.

5.3.2.3 Methodology for sample displacement chromatography

In an attempt to mitigate the overlapping of neighboring variants in a ternary mixture, a three-columns-in-series set-up (Figure 5.2) was used. A sufficiently large amount of the sample was loaded onto the first two columns to exceed their capacity, with the excess sample that could not be accommodated in the first two columns being captured on the third column (Figure 5.3A). Because the acidic variant has the lowest affinity to the CEX column, followed by the native and the basic variant, the basic,

native and acidic variants were retained primarily on the first, second and third columns respectively, albeit in broadly overlapping zones as discussed above.

The columns were then washed with the equilibration buffer to push the residual sample in the pore space of the first two columns onto the last column, which reduces sample loss. After washing, the valves were switched to bypass the flow to one of the first two columns, allowing the bound sample from each of the first two columns to be recovered separately using elution buffer (Figure 5.3B, C). The product bound on the third column was not eluted, and instead, in the next cycle, the valves were switched again to make the last column the first in the series, with the other two re-generated columns added as the second and last columns for the second cycle (Figure 5.3D). A sample amount equivalent to the capacity of the first two columns was then loaded onto the new first column in series. The previously described zone comprising a broad overlap of the acidic and the native variant from the first cycle thus remained in the system and therefore only a sample amount equivalent to the capacity of the first two columns was loaded. Washing of the columns and elution from the first two columns in series were repeated as described for the previous cycle (Figure 5.3E, F). Additional cycles were run until the desired purity of the native variant was met. This approach of combining displacement and recycling allows the native and the acidic variants from the last column to be recycled back into the system and thus improve the yield.

Given the three-column recycling set-up, the main design challenge in executing mAb charge variant displacement is to determine the resin's capacity for each variant given the sample's charge variant composition. Since the charge variant composition of different therapeutic mAbs can vary, the size of each column can be

calculated with respect to the composition. The resin capacity for each component can be estimated from experimental test breakthrough curves of the charge variants. However, in this work a more detailed approach was also used by modeling the displacement process from the breakthrough curves for each variant on a single column at three different starting mAb compositions using the general rate model and multicomponent Langmuir isotherm (section 5.3.2.4).

If the goal of the purification is to remove or reduce only the acidic charge variants, a simpler single-column recycling approach can be adopted (Figure 5.3G). In this set-up, one can switch from sample loading to the recycling mode as soon as the acidic component is displaced by the other two components. Switching to the recycling mode allows the flow-through, which is a mixture of the displaced acidic components as well as the ternary load, to be re-fed to the column to provide more contact time between the resin and the native and the basic variants that were not retained during the initial sample loading. The drawback of a single-column recycling set-up could be a lower yield, but given the need for only a single column, the effort and cost required are lower. Furthermore, the basic variant can be removed afterwards following the same principle using anion-exchange chromatography.

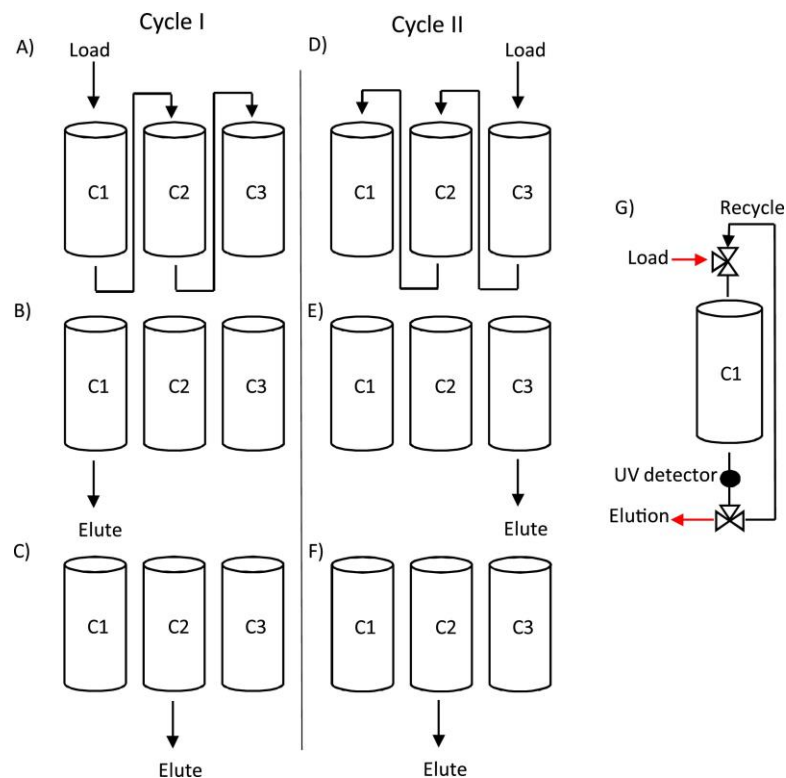


Figure 5.3 (A-F) Schematics of different stages of three-column displacement chromatography with recycling. (G) Schematic of single-column process with recycling.

5.3.2.4 Mechanistic modeling

The general rate model, given in section 4.2.2.2, was coupled with the multicomponent Langmuir isotherm model to describe the partitioning of solute between the liquid and solid phases. When all the components compete for the same binding sites, the binding model can be written as

$$\frac{\partial q_i}{\partial t} = k_{ai}c_{pi}q_{maxi} \left(1 - \sum_{j=0}^{N_{comp}-1} \frac{q_j}{q_{maxj}} \right) - k_{di}q_i \quad i = 0, \dots, N_{comp} - 1 \quad (5.1)$$

where q_{maxi} is the maximum binding capacity and k_{ai} and k_{di} are the association and dissociation rate constants of the i^{th} component. All the column chromatography

simulations were performed using CADET (Chromatography Analysis and Design Toolkit), made available by Forschungszentrum Jülich, Germany.

5.4 Results and discussion

5.4.1 Optimizing the selectivity for mAb variants using one-column breakthrough experiments

Displacement chromatography requires that the variants under consideration have differing affinities to the resin to allow the displacement of a variant with a lower binding affinity by a variant with a higher binding affinity. The subtle differences in the resin's selectivity for the variants can be resolved by careful selection of the pH and buffer strength. On a CEX column, the resolution of the acidic and basic charge variants is reduced at lower pH values, where the affinity of all species to the resin increases. On the other hand, the affinity and the static capacity are reduced at higher pH, making careful pH selection critical. In addition to pH, the buffer ionic strength should be chosen to optimize the resolution and the capacity for each variant in the presence of the other two variants. To this end, one-column breakthrough experiments at three pH values, two buffer strengths and three different charge variant compositions were conducted, where the breakthrough curves for the individual variants were determined by separating fractions using analytical CEX.

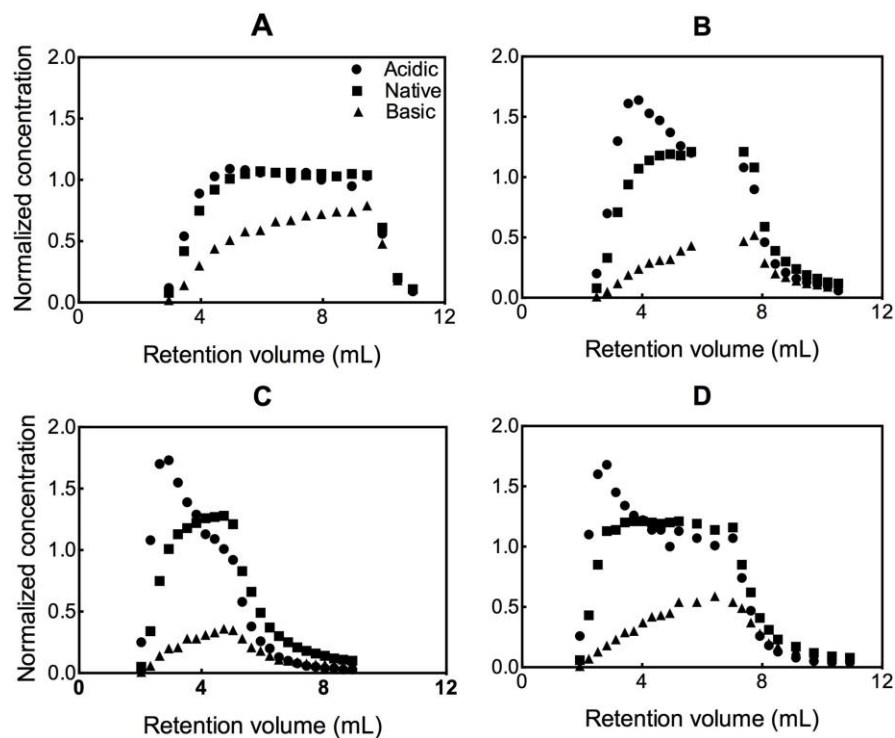


Figure 5.4 Chromatograms showing the normalized breakthrough curve for each variant using sodium phosphate buffer of pH 6.3 (A), 6.5 (B) and 6.7 (C) at 10 mM sodium phosphate buffer and pH 6.5 (D) at 15 mM sodium phosphate buffer.

Once loading ceased, the concentrations of all the variants leaving the column declined. Furthermore, since the basic variant displaced both the acidic and main variants, a dual breakthrough trend can be seen on careful examination. Especially in Figure 5.4B, near a retention volume of 5 mL, a transition can be seen in the breakthrough curves of the acidic and the basic variants. Prior to this transition point, a significant amount of the acidic variant was displaced, while after the transition point, the normalized concentration of the acidic variant had reached near unity while the native variant was still being displaced. This ordering in displacement is expected given the acidic variant's lower affinity to the column, compared to the basic variant.

The highest capacity and the best separation among the conditions explored were obtained using 10 mM sodium phosphate at pH 6.5 (Figure 5.4B), based on quantitative analysis of the breakthrough curves. At the lower pH of 6.3, all the variants bind more strongly to the column and therefore minimal displacement is seen (Figure 5.4A), while at the higher pH of 6.7 (Figure 5.4C), the capacity was lower than that at pH 6.5. Increasing the buffer strength to 15 mM also reduced the overall capacity, so pH 6.5 at 10 mM was selected for all subsequent experiments, but it is worth noting that having satisfactory capacity at both pH values of 6.5 and 6.7 allows for a more robust method.

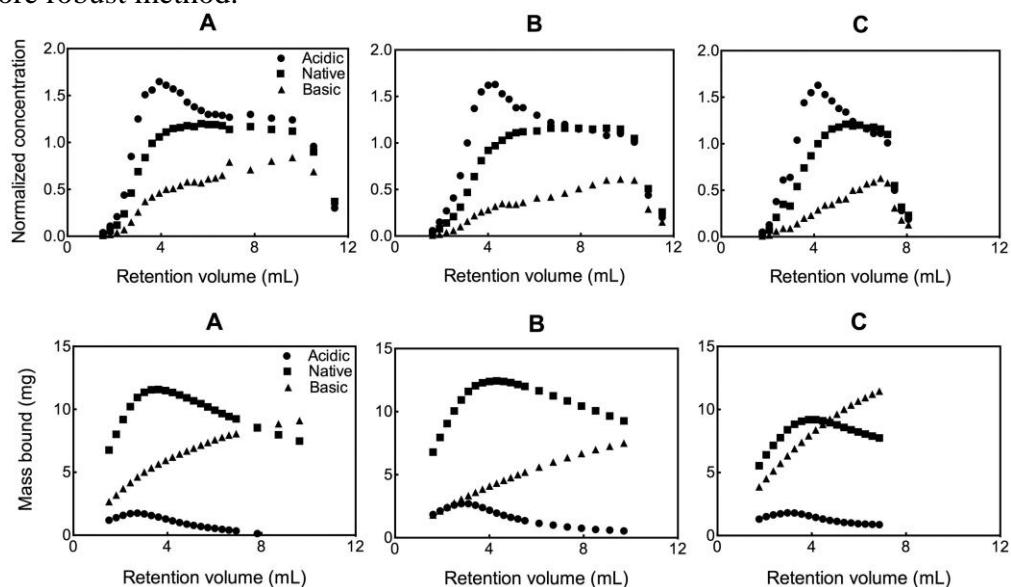


Figure 5.5 Top panels: Normalized chromatograms showing the breakthrough curve for each variant for each of three mAb variant feed compositions. Bottom panels: The mass of each variant retained within the column as a function of the retention time. The compositions of the acidic-native-basic variants for samples A, B and C were 11.4-63.0-25.6, 17.7-65.0-17.2 and 12.3-51.7-36.0, respectively.

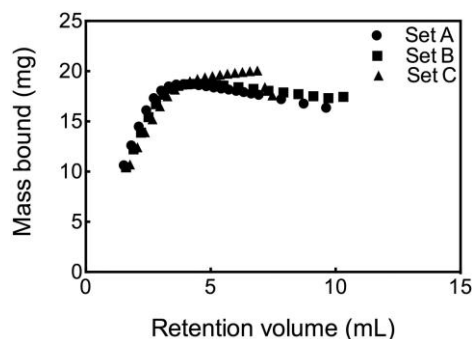


Figure 5.6 The total mass of mAb retained within the column as a function of the retention time for the three cases shown in Figure 5.5.

In addition to the optimal pH and buffer strength, the column capacity for each variant in the presence of the other two variants was investigated by evaluating the breakthrough curves of mixtures of three different charge variant compositions. Figure 5.5 shows the breakthrough curves in terms of both the concentration normalized to the starting concentration (top panels) and the instantaneous mass of each variant within the column (bottom panels), as a function of retention volume. As expected, the acidic-enriched sample (A) has a higher mass of the acidic variant bound while the basic-enriched sample (B) has a higher mass of the basic variant bound on the column. More importantly, despite the differences in the compositions, the total mass within the column for all three samples was the same (17.6 mg) at an approximate retention volume of 4 ml (Figure 5.6). After this point, the total mass within the column either rises for the more basic mixture or drops for the more acidic mixture. A total mass of 17.9 mg corresponds to 50 mg of protein per mL of resin and thus 90% of this value (45 mg/mL) can be used for loading onto each column in the displacement chromatography set-up.

5.4.2 One-column recycling set-up

The simplest set-up for mAb enrichment using displacement chromatography is a single column with recycle. If a mAb sample is loaded onto the column beyond saturation capacity, the higher-affinity basic and native variants will displace the acidic variant. However, some native variant is also displaced by the basic variant and is lost along with the acidic variant during the breakthrough. Allowing the acidic-variant-rich breakthrough to re-enter the column from the top reduces the loss of the main variant.

The one-column recycling approach was implemented with mAb representing 53 mg/mL of resin (110% of capacity) loaded onto a Poros 50 HS column of 0.35 mL I.D. and 5 cm bed height and the loaded mAb was recycled for 40 column volumes (approx. 14 mL). In the resulting chromatogram (Figure 5.7), the UV curve shows the concentration of mAb within the recycling system as a function of the retention volume since the UV detector is immediately downstream of the column. The total concentration of mAb in the recycling loop becomes invariant after about 40 CV. The bound mAb was eluted using a salt gradient and the eluate was analyzed by analytical CEX. The eluted peak contained 2.1% acidic, 53.9% native and 43.9% basic variants of the mAb, while the starting composition was 11.1%, 64.3% and 24.6% respectively, demonstrating that the recycling method allowed reduction of the acidic variant by 81% of the original. The recycle stream's composition was 24.4%, 66.5% and 9.1% respectively, resulting in a yield of 61% for the native variant. Although the level of the acidic variant was significantly reduced, this finding also shows that a one-column system is not sufficient to displace two variants from a ternary mixture.

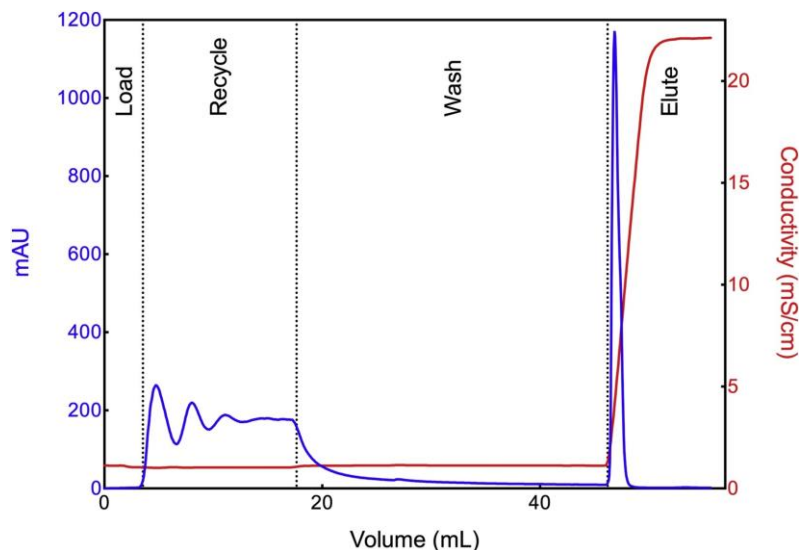


Figure 5.7 Chromatogram showing the recycled and the subsequently eluted mAb. UV absorbance at 295 nm and conductivity over the course of the experiment are shown in blue and red respectively.

5.4.3 Two-column set-up

The displacement and the subsequent enrichment of components in a ternary mixture require a minimum of two columns. Using a two-column set-up for a ternary mixture in which the component affinities to the column are sufficiently disparate would result in the removal of the acidic component in the breakthrough or early elution and the enrichment of the native and basic variants on the second and first columns, respectively. However, for mAb charge variants for which the affinities to the resin are similar, further improvements are desired.

Improvement of the resolution of the native and basic variants in elution of the first and the second columns in the two-column set-up would help mitigate the effect of the overlap between the native and the basic variants in the columns. To this end a dual gradient of pH and salt was utilized to augment the separation resulting from displacement. Figure 5.8A shows the mAb elution profile from a two-column set-up

with a salt gradient alone while Figure 5.8B shows the elution profile resulting from a dual gradient using an elution buffer of pH 5.5. Baseline resolution of the two elution peaks was achieved when an elution buffer of a lower pH of 5 was used (Figure 5.8C). Only one peak is generated with a salt gradient while two peaks, the latter of which is enriched in the basic variant, are generated with a dual gradient.

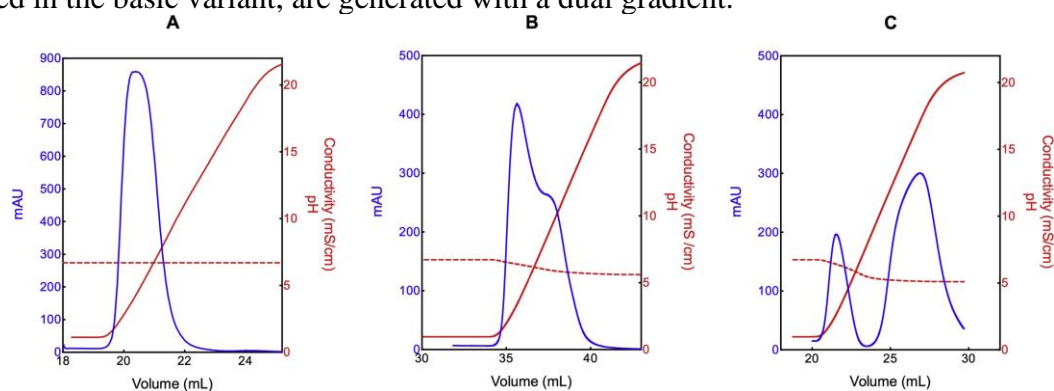


Figure 5.8 Chromatograms showing mAb elution profiles using dual salt–pH gradient in a two-column set-up. UV absorbance and conductivity over the course of the experiment are shown in blue and red respectively. (A) Salt gradient alone. (B) Dual gradient, with pH gradient from 6.5 to 5.5. (C) Dual gradient, with pH gradient from 6.5 to 5.0.

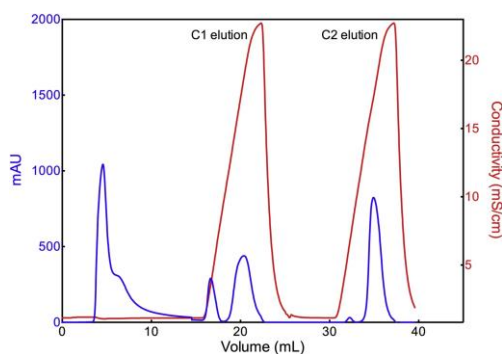


Figure 5.9 Chromatogram showing the absorbance and conductivity obtained in the two-column set-up and the resulting eluted mAb. The elution and loading buffers were of pH 5.5 and 6.5. UV absorbance at 295 nm and conductivity over the course of the experiment are shown in blue and red, respectively.

Table 5.1 Charge variant profile of different peaks in two-column system.

Fraction	Acidic %	Native %	Basic %	Mass % of load	Recovery of native mAb (%)
Breakthrough	16.5	83.5	0	47.9	61.4
Column 1 peak 1	2.7	70.7	26.6	5.8	6.3
Column 1 peak 2	2.3	17.9	79.8	19.3	4.1
Column 2 peak 2	4.5	69.8	25.7	26.4	28.2

5.4.4 Three-column set-up

The two-column system was improved by allowing what was previously the breakthrough to be captured on a third column. After loading and washing, the adsorbates were eluted from the first two columns and the columns were repositioned so that the third column became the first column in the next loading phase, as shown in Figure 5.3. This improvement upon the two-column system allows a higher yield. Three equally-sized columns were used for the three-column experiments, but since the native variant is a much larger fraction than the acidic and basic variants, a dual salt–pH gradient was used for elution to improve resolution.

Using the three-column set-up, five cycles of loading and recycle were performed. The yields and purities of the native variant and the chromatograms associated with the five-cycle run are shown in Table 5.2 and Figure 5.10, respectively. For each two-column pair of elutions, the latter peaks are enriched in the basic variant and therefore the former peaks were pooled to determine the yield and the purity of the native variant. As shown in Table 5.2, 70-90% yield and 80-90%

purity are obtained using the three-column set-up and a dual gradient. After completion of the second cycle, purities and yields up to 91% were obtained.

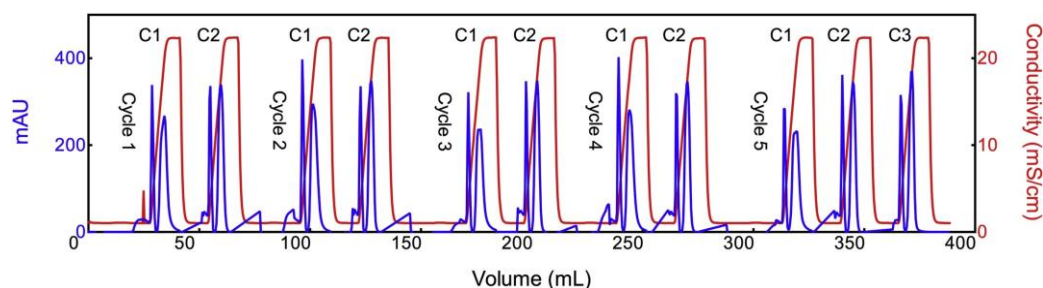


Figure 5.10 Chromatograms showing five cycles of the three-column experiment and the subsequently eluted mAb. The load buffer was of pH 6.5 and the elution buffer was of pH 6.5 - 5.0. UV absorbance at 295 nm and conductivity over the course of the experiment are shown in blue and red, respectively.

Table 5.2 Number of cycles, total mass loaded and eluted native variant yield and purity for the three-column experiments.

Cycle	Load (mg/mL of resin)	Native yield %	Native purity %
1	45 (3 column load)	71	79
2	45 (2 column load)	91	91
3	45 (2 column load)	89	89
4	45 (2 column load)	85	86
5	45 (2 column load)	82	91

The capabilities of the displacement method can be seen in perspective by comparison with separation of the same sample using a simple, shallow, linear gradient of 40 column volumes, using the same equipment, column and buffers described in Materials and Methods. The elution peak (Figure 5.11A) shows a single

shoulder that reflects some separation of basic variants. A more detailed analysis, obtained by collecting and analyzing 23 fractions (as shown in Figure 5.11A) by HPLC and then pooling in order of decreasing native variant content, confirms some separation of basic from the native and acidic variants but no meaningful separation of the acidic variants (Figure 5.11B). Optimal pooling of fractions for a specified yield of 90% would give a native variant pool of at most 70% purity, in contrast to the 90% obtained by the displacement method.

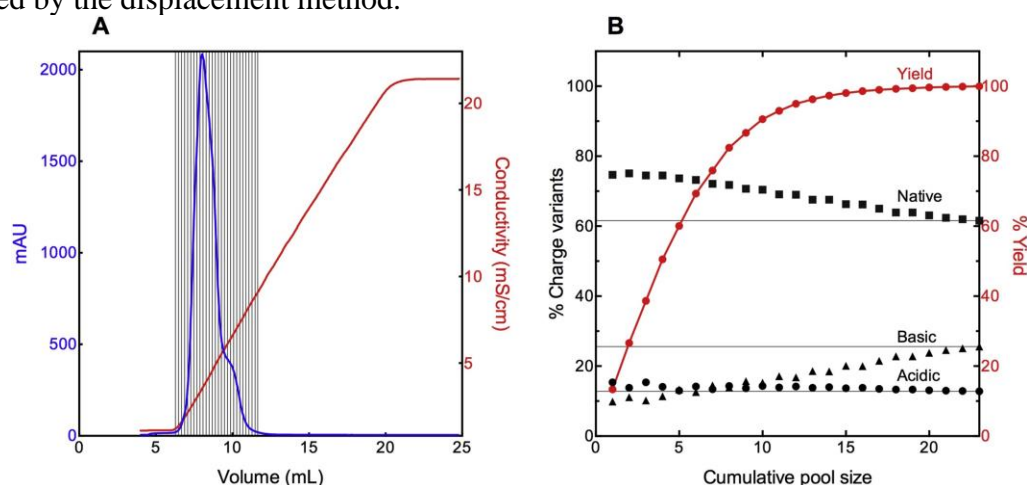


Figure 5.11 Separation of charge variants by a conventional linear gradient of 40 column volumes using column and conditions described in Materials and Methods. (A) Chromatogram showing elution profile. Absorbance at 280 nm and conductivity are shown in blue and red, respectively, while the vertical lines show the fractions collected. (B) Composition and yield of the elution pool as a function of fraction number, shown in descending native variant content, pooled. The horizontal lines indicate the charge variant composition of the load.

5.4.5 Predicting displacement behavior in the column using general rate model

In designing optimal displacement experiments, the resin's capacity for each charge variant and the amounts to be loaded were determined by generating breakthrough curves. Although this approach is convenient in the absence of other

alternatives, it does not reveal the profiles of the bound charge variant compositions along the length of the column. The development of the displacement by the component(s) of higher affinity of the component(s) with lower affinity and the consequent emergence of zones along the column were instead simulated using a mechanistic model. Although simulations from the model are not required to carry out the displacement work, they can help visualize the differing progression of the charge variants from the feed along the length of the column as displacement occurs.

The general rate model with a multi-component Langmuir isotherm was fitted to the component breakthrough elution profiles of the three mAb samples with different charge variant compositions (A, B and C) using the fitting isotherm parameters $k_{a,i} / k_{d,i}$ and $q_{\max,i}$, as shown in Figure 5.12. The initial estimates of the parameters were found by fitting a breakthrough elution profile of the pure native component. The parameters for the other variants, including both isotherm and transport parameters, were obtained by fitting to the breakthrough data and are shown in Table 5.3.

The fits and predictions for the native and acidic variants were quite accurate while those of the basic variant showed some deviation. The fitted breakthrough curve for the basic variant captured the initial curvature of the experimental data but the plateau region was not well explained by the model. However, since the model explained the displacement of the native and the acidic variants with sufficient accuracy, the parameters obtained were used further without any additional adjustment.

Table 5.3 Parameters resulting from fitting experimental data to the general rate model with a multi-component Langmuir isotherm.

Parameters	Acidic variant	Native	Basic variant
k_a/k_d	900	1311	1511
q_{\max}	1.0 mM	1.2 mM	2.0 mM
Axial dispersion coefficient	$3.9 \times 10^{-8} \text{ m}^2\text{s}^{-1}$		
Surface diffusivity	$5 \times 10^{-13} \text{ m}^2\text{s}^{-1}$		
Pore diffusivity	$1.2 \times 10^{-12} \text{ m}^2\text{s}^{-1}$		

The right panels of Figure 5.12 show the simulated enrichment of the acidic, native and basic components along the length of the column for a total sample loading of 45 mg/mL of resin capacity, which was fed at a constant rate. It is worth noting that the simulated breakthrough curves show that the basic variant does not exit columns of 20 and 25 cm. The simulations allow the length required for optimal displacement with known charge variant composition to be estimated, as well as the resin's capacity for each variant. Furthermore, the model shows the previously-described zone development occurring on the solid phase. The 3-D plots in Figure 5.13 show the protein concentration in the solid phase as a function of time and axial position for a mAb sample for loading of 45 mg/mL of resin capacity. The enrichment of both the acidic and native components occurring along the length of the column can clearly be seen. The enrichment of the acidic variant occurs at a much faster rate than that of the native variant since the acidic variant is displaced by both the native and the basic variants while the native variant is displaced only by the basic variant. Furthermore, the zones enriched in the acidic and the native variant overlap more broadly than those

of the native and the basic variant, due to the more similar affinity to the resin between the acidic and the native variant in contrast to that between the native and the basic variant. These results suggest that a complete separation of the acidic variant from the native variant is not possible under these conditions.

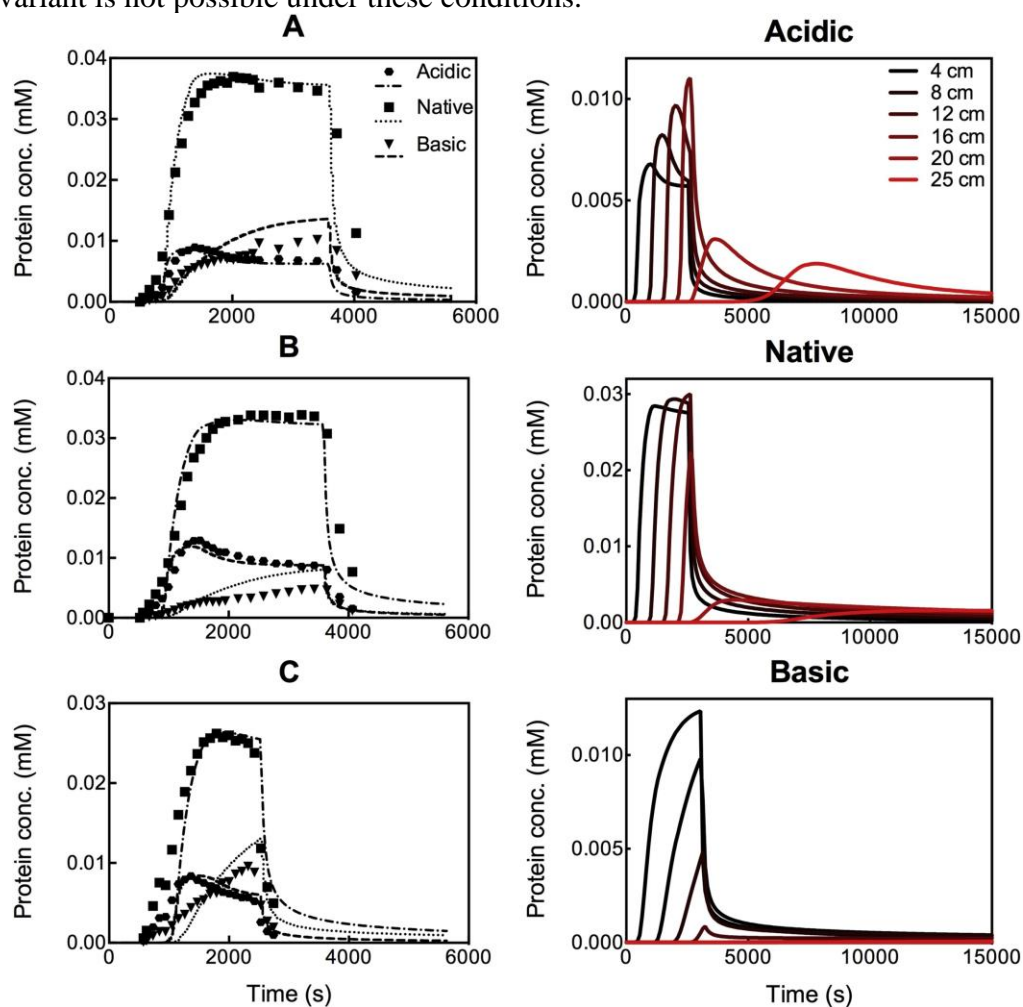


Figure 5.12 (Left) Experimental breakthrough curves for samples with various compositions (A, B and C) as well as fits to the general rate model with a multi-component Langmuir isotherm. The variant compositions for A, B and C are as given in Figure 5.5. (Right) Simulated breakthrough curves of the acidic, native, and basic variants showing the exiting protein mass per bed volume as a function of time. No basic variant was seen exiting columns of 20 and 25 cm under a loading of 45 mg/mL resin in the simulation.

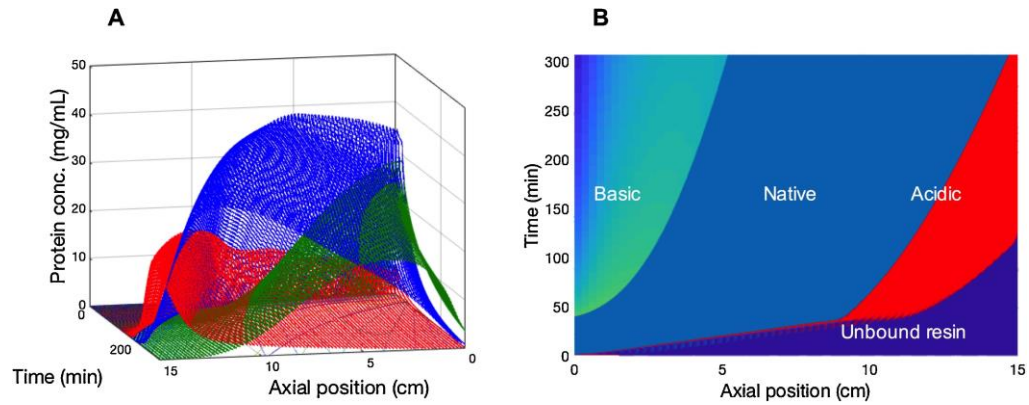


Figure 5.13 3-D depictions of the charge variants' predicted concentrations as a function of the column axial position and time in a 15 cm column using the simulations of the mechanistic model. Concentrations are shown (A) on the solid phase and (B) in a 2-D projection of (A).

5.4.6 Implementation approach

Separating mAb charge variants in preparative ion-exchange chromatography can be challenging given the biophysical similarities among the variants, but the results presented above show that the principles of displacement chromatography along with a multi-column approach and dual gradient elution can be used with partial recycling to achieve a separation with a high purity and yield. However, applying these principles in process development on a larger scale, subject to restrictions on packable column length and variations in the compositions and properties of the input charge variants, is not straightforward. Our results suggest that if the starting mAb charge variant composition does not vary by more than 5% from the range of compositions that we explored, an acceptable yield is feasible with fixed column lengths. An optimal pH and ionic strength should first be chosen to allow for maximum displacement and resin capacity, based on single-column breakthrough experiments such as those shown in Figure 5.4 Correspondingly, an analysis of total

mAb bound, such as that shown in Figures 5.5 and 5.6, can provide an initial estimate of the sample amount to be loaded on the columns. However, as the simulations in Figure 5.1 show, the development of displacement zones is a function of column capacity relative to column load.

Some of the empirical exploration necessary in the above approach can be avoided by using a mechanistic model such as that employed here for direct optimization of the operating parameters. The profile of the charge variants along the length of the column and hence the optimal length of each column can also be calculated. If the displacement of the charge variants along the length of column does not result in enriched zones of individual variants, as was the case here for the native and the acidic variants, a recycling approach can be implemented. However, the recycling set-up requires the first and last columns to be of equal length.

It is worth noting that the yield and purity of the resolved native variant depend largely on the length of the center column in which the native component is enriched. If purity is paramount, the length of the center column can be reduced, while if yield is more important, the center column can be lengthened. In essence, the relative length of the center column is the primary design handle that can be chosen based on desired yield and purity. Although the use of a dual gradient is not essential, it serves as an additional tool to improve the yield and purity.

Whichever of these approaches is used, the appreciable enrichment achieved allows multiple degrees of freedom in using the different fractions. The charge variant composition is of particular interest for biosimilars, where the enriched fractions can be remixed to match the charge variant proportions of the innovator product. However, if enrichment of the main variant is desired, the approach presented here can

achieve this with high yield and a high degree of column utilization. The method would, of course, also be adaptable for enrichment of charge variants in non-mAb proteins.

5.5 Conclusions

The separation and enrichment of mAb native charge variants to both a yield and a purity of ~ 90% was achieved. A multi-prong approach including a combination of self-displacement ion-exchange chromatography with a dual gradient of pH and salt, along with partial recycling and a multi-column set-up, were utilized to this end. To enrich two components from a ternary mixture, a single column with recycling was shown to be sufficient, as demonstrated by > 85 % reduction of the acidic variant. Furthermore, the inadequacy of a two-column set-up without recycling was demonstrated as it achieved separation of the acidic and the basic variants but with a low yield of < 30 %. However, upon addition of a third column, the native variant from the breakthrough was captured on the third column, improving the yield, and the dual gradient provided improved resolution between the basic and native variants.

The design of separation processes was carried out with and without the use of a mechanistic model. The multi-column design demonstrated in this work is a set-up for the mAb compositions that we have used, but other designs are possible. The primary benefit of our work is in the exploitation of the self-displacement principle to separate the charge variants on a preparative scale while utilizing the column to its full capacity. Given the relevance and increased usage of continuous chromatography in the bioprocessing industry, this work can aid in the design of separation processes for the enrichment of mAb charge variants. These variants can then be easily combined to target a desired charge variant composition. Apart from mAb charge variants, our

methods and approaches can be utilized in the separation and enrichment of any multicomponent protein mixtures with differing affinities.

Chapter 6

DISPLACEMENT CHROMATOGRAPHY FOR SEPARATION OF HOST-CELL PROTEINS AND PRODUCT AGGREGATES

6.1 Introduction

The purification of therapeutic proteins such as monoclonal antibodies (mAbs) requires effective removal of many process and product related impurities such as host-cell proteins (HCPs), nucleic acids, and leached resin components, product aggregates and certain product isoforms. Certain heterogeneities in the product, such as disulfide bond scrambling, contribute to protein aggregation (Morris et al., 2009; Remmele et al., 2006; Roberts, 2007), among other causes. Aggregates (Liu et al., 2005; Luo et al., 2014; Vázquez-Rey and Lang, 2011) may grow across cell culture, recovery, purification, and storage, and their chromatographic separation from monomers is difficult due to their similar isoelectric points and hydrophobicities. Since mAb aggregates also contain the Fc domain and cannot be separated by protein A chromatography (Marichal-Gallardo and Álvarez, 2012; Shukla et al., 2007), they are often separated using cation-exchange chromatography (CEX) in bind-and-elute mode (Borg et al., 2014). Although more effectively achieved by protein A chromatography, reductions in the residual HCP after a CEX step are also routinely observed (Levy et al., 2016; Liu and Tang, 2008).

As demonstrated in Chapter 5, heterogeneities in the product give rise to subtle variations in their affinities to CEX resins. Similar to mAb charge variants, protein

aggregates (Khanal et al., 2019a; Reck et al., 2017) are retained differently on CEX resins. This difference in retention has also been leveraged to separate aggregates through salt gradient elution (Suda et al., 2009; Zhou et al., 2007), hybrid pH-salt gradient elution (Khanal et al., 2019a; Zhou et al., 2007), and flow-through operation (Ichihara et al., 2018; Ichihara et al., 2019; Khanal et al., 2019a; Suda et al., 2009; Ulmer et al., 2019; Vogg et al., 2020a). Separation of mAb aggregates using flow-through ion-exchange chromatography is enabled by displacement of bound monomer by incoming aggregates (Carta and Jungbauer, 2010). Since the aggregates bind more strongly on the column, they can be separated using a significantly smaller column than would be needed for elution chromatography. However, unlike for elution chromatography, the loading conditions influence the separation in flow-through chromatography as separation occurs during loading. While Reck et al. achieved the greatest separation of mAb monomer/dimer mixtures at intermediate ionic strength (Reck et al., 2017) using Nuvia HR-S, Stone et al. (Stone et al., 2019) generally found greater aggregate removal with decreasing buffer conductivity. Stone et al. also reported decreasing aggregate removal with increasing pH, sample concentration, charge density of the resin and protein residence time using Eshmuno® CP-FT. While the aggregate-binding capacity is resin-dependent (Zhang et al., 2017), the extent to which aggregates displace monomer is variable from mAb to mAb (Ichihara et al., 2018; Liu and Tang, 2008).

Despite the variability among different mAbs, all studies demonstrate an advantage of frontal operation: the ability to overload the column. This can enable improved separation because overloading promotes displacement as a result of the increased likelihood of displacement in the presence of a larger amount of the

displacing species (Khanal et al., 2019a). However, overloading can contribute to yield loss (Khanal et al., 2019a) because mAb monomers and aggregate have similar affinities to CEX resins. Combining overloading with a multi-column set up, as was done in Chapter 5, not only allows capture of the initial breakthrough onto the subsequent columns but also reduces the required resin mass (Vogg et al., 2020a). To this end, Vogg et al. have demonstrated a two-column counter-current flow-through chromatography set up to be more robust than similar batch processes for the separation of mAb aggregates.

Although some studies have evaluated displacement for mAb aggregate removal (Ichihara et al., 2018; Ichihara et al., 2019; Reck et al., 2017; Stone et al., 2019; Suda et al., 2009; Vogg et al., 2020a; Wollacott et al., 2015), investigation of how displacement affects the population of HCPs has not extended beyond a secondary analysis validating the effectiveness of proposed methods (Ichihara et al., 2018; Ichihara et al., 2019; Liu and Tang, 2008; Ulmer et al., 2019; Wollacott et al., 2015). Unlike mAb aggregates, which, although heterogeneous, all originate from the mAb product, HCPs are a heterogeneous set of proteins of various biophysical properties, function, and abundance. While aggregates collectively bind more strongly to the resin than do the monomers, HCPs display a distribution of affinities for the resin, with subgroups of HCPs binding to the resin with equivalent, less or more affinity than the product. Therefore it is less practical to treat HCPs as a single impurity when discussing their displacement.

Another factor complicating HCP separation is their low prevalence. The feed HCP content in this work is one to two orders of magnitude lower than the starting aggregate content of 1.4%, making displacement analysis of HCPs less trivial.

Additionally, although an enzyme-linked immunosorbent assay (ELISA) is a benchmark assay method, the antibodies provided in ELISA kits do not cover the full spectrum of HCPs, and low-affinity binding cannot be detected (Gunawan et al., 2018; Zhu-Shimoni et al., 2014). Therefore HCP quantification using ELISA does not necessarily measure HCP subpopulation amounts accurately. Furthermore, studies have shown that problematic HCPs need not be present in large quantities (Beatson et al., 2011).

Given the outlined difficulties and uncertainties associated with the investigation of HCPs, systematic studies exploring the migration of HCP along a column due to displacement have not been published. Evaluation of HCP removal by overloaded chromatography has been limited to resin and conductivity screening (Liu and Tang, 2008). Considering the importance of displacement in flow-through chromatography, we demonstrate displacement for low-prevalence impurities such as mAb aggregates (1.4%) and HCPs ($\geq 0.002\%$). We then evaluate factors enhancing displacement and leverage these in the proposed displacement chromatography designs.

6.2 Materials and methods

6.2.1 Materials

An acetate buffer system was used for chromatography experiments at pH 5-5.75 and a phosphate buffer system was used for chromatography experiments at pH 6.2 and for HPLC analysis. The mAb formulation (160 mg/mL), provided by Amgen (Thousand Oaks, CA), was buffer-exchanged immediately before use into the appropriate buffer using a GE Sephadex G25 desalting column and diluted to a

working concentration range of 2.9-22.0 mg/mL. The mAb concentration in solution was measured by absorbance at 280 nm using a Nanodrop 2000 (Thermo Scientific, Waltham, MA). An HCP standard (HCP006) from Chinese hamster ovary cells was purchased from Canopy Biosciences (St. Louis, MO) and added to the mAb solution to obtain HCP concentrations of 20-1630 ng/mg (parts per million, ppm) of mAb.

The chromatography experiments were performed on an Äkta Pure workstation (GE Healthcare, Uppsala, Sweden) with UV and conductimetric detectors and a fraction collector. Glass columns (Omnifit, Diba Industries Inc., CT) of inner diameter 0.3 cm and lengths of 2.5-5 cm (volume 0.177-0.353 mL) were first slurry (50%) packed with Poros HS 50 resin (Applied Biosystems, Foster City, CA). The chromatographic runs were conducted at linear flow rates of 50-300 cm/hr and mAb concentrations of 2.9-22 mg/mL. Under column operation, the protein sample was first loaded onto the equilibrated column(s), followed by washing of the column(s) using the equilibration buffer and elution using the elution buffer. All columns were sanitized with 0.5 M NaOH after every five runs. The order of column elution for the multi-column setups is shown in Figure 6.1.

MAb aggregate was quantified using an Agilent® AdvanceBio size-exclusion chromatography (SEC) 300 Å column, 4.6 x 150 mm, with 2.7 µm particles using 50 mM sodium phosphate buffer at pH 6.8 with 200 mM NaCl in isocratic mode, on a Waters® 2695 HPLC equipped with a UV detector. HCP content was quantified using an ELISA kit by Canopy Biosciences for the CHO HCPs (HCP001), following the manufacturer's protocol and using a Synergy2 Microplate Spectrometer/Fluorimeter (Biotek, Winooski, VT).

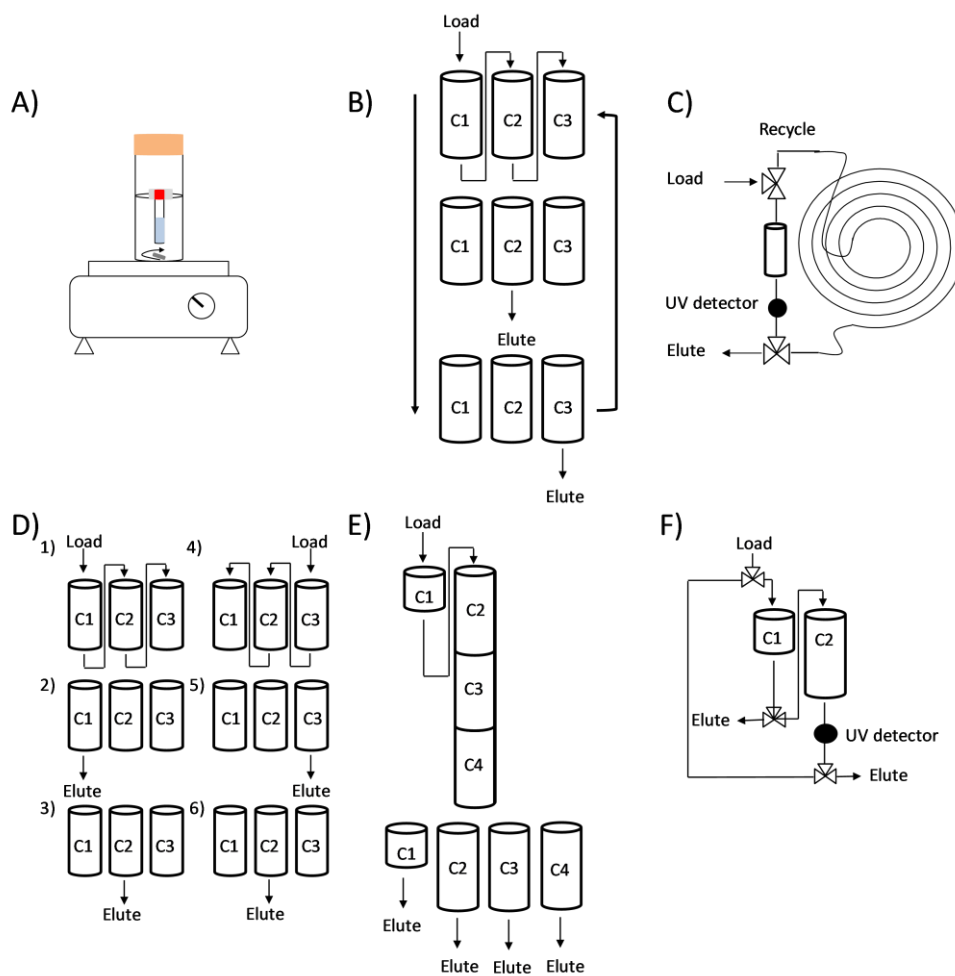


Figure 6.1 (A-C) Schematics of displacement approaches used for aggregate removal: (A) batch experiment conducted on a stir plate, (B) three-column displacement chromatography with partial recycling, and (C) recycling. (D-F) Schematics of displacement approaches used for HCP removal: (D) three-column displacement chromatography with partial recycling, (E) four columns in series, and (F) two-column recycling.

6.2.2 Aggregate displacement methods

6.2.2.1 Batch

Poros HS resin (177 μL) was placed inside a Spectrum Spectra/Por Float-A-Lyzer G2 dialysis device with a 1,000,000 Da molecular weight cut-off. The dialysis device was placed in a 50 mL conical tube with 8.6 mL of 8.8 mg/mL mAb solution. The sample pH was 5.75 and the buffer ionic strength was 35 mM. A small stir bar placed inside the conical tube ensured mixing of the solution on the stir plate. The mAb and aggregate depletion from the solution was evaluated by sampling 100 μL of solution at each time point shown in Figure 6.2C, measuring the absorbance at 280 nm and injecting 50 μg onto the SEC column on the HPLC.

6.2.2.2 Three-column

Sample amounting to 90% of the total resin capacity for the mAb monomer (45 mg/mL resin) was loaded onto a setup comprising a series of three 0.35 mL columns, as shown in Figure 6.1B. In doing so, nearly thrice and twice the capacities of the first and second columns respectively were fed, with the excess feed that could not be accommodated in the first two columns being captured on the third column. During loading, aggregate, which has a higher affinity to the resin, displaces the monomer, which has a lower affinity to the resin. Therefore, the first column is aggregate-enriched, while the subsequent columns have decreasing aggregate content.

The columns were washed with equilibration buffer to allow capture of the sample in the pores of the first two columns on the third column to reduce losses. After the wash, the bound monomer from the last two columns was eluted separately and sequentially by switching the valves to bypass the flow of the elution buffer to the other two columns. Although the first column is aggregate-enriched, because most of

the bound mAb is monomer, the content from the first column was not yet eluted and discarded. Instead, to accumulate more aggregate onto the first column in the next cycle, additional sample was fed onto the first column with the other two re-generated columns added in series. The amount of sample fed at each additional cycle amounted to the capacity of the first two columns. Washing and elution from the last two columns were repeated as described for the previous cycle. A total of 7 cycles were run.

6.2.2.3 Recycle

A small (0.177 mL) column with capacity for ~ 10% of the total feed was used. The column was connected to a loop accommodating excess sample volume [16.7 mL]. During application of a 4.3 mg/mL sample at 0.35 mL/min, the effluent from the column was retained in the lengthy loop. Once the loop was filled, the retained effluent was recycled back onto the column and this cycle was repeated three times. Additional runs were carried out using the same approach at sample concentrations of 12.3 and 22.0 mg/mL, all with with a fixed sample mass of 71 mg.

In a variant of the recycling method, instead of passing the column effluent through a lengthy loop, it was concentrated in-line using a Minimate tangential flow filtration (TFF) capsule (50 kDa) Omega membrane and fed back into the column. This approach was implemented to address the dilution of the recycled sample compared to the initial feed. This approach is therefore referred to as the concentrate-and-recycle approach.

6.2.3 HCP displacement methods

6.2.3.1 Three-column

Following a procedure similar to that in section 6.2.2.2, sample amounting to 90% of the total resin capacity for the mAb monomer was loaded onto a three-columns-in-series setup, as shown in Figure 6.1D. During loading, those HCPs (presumably basic) with a higher affinity to the resin than the mAb displaced the mAb, while the mAb displaced the lower-affinity (presumably more acidic) subset of HCPs. Therefore, the first column is expected to be enriched in basic HCPs while the last column is expected to be enriched in acidic HCPs.

The columns were washed with equilibration buffer and eluted separately, as outlined in section 6.2.1.2. The product bound on the third column was not eluted and instead, in the next cycle, the valves were switched again to make the last column the first in the series, with the other two re-generated columns added as the second and third columns for the second cycle. A sample amount equivalent to the capacity of the first two columns was then loaded onto the new first column in series. Washing of the columns and elution from the first two columns in series were repeated as described. A total of 3 cycles were run.

6.2.3.2 Four-column

Sample amounting to 90% of the total resin capacity for the mAb monomer (45 mg per mL resin) was loaded onto a four-columns-in-series setup, as shown in Figure 6.1E. The first column was chosen to be half the length of the other 0.35 mL columns to allow for the evaluation of displacement zone development in what is essentially the top portion of a long column. Following loading, the columns were washed with equilibration buffer and eluted separately and sequentially.

6.2.3.3 Two-column

A two-column recycling approach, shown in Figure 6.1F, was evaluated for HCP displacement. Sample amounting to 115% of the total resin capacity (27 mg) was fed to the 0.177- and 0.35-mL columns in series at 0.35 mL/min at 7 mg/mL sample concentration. The effluent from the second column was recycled back into the second column and this procedure was repeated seven times, after which the two columns were washed in series and eluted sequentially.

6.3 Results and discussion

6.3.1 Aggregate separation by displacement using frontal methods

The mAb sample containing 1.4% aggregate was loaded onto a 0.353 mL column and the breakthrough was collected in fractions of 0.3 mL. The aggregate breakthrough curve was then resolved from the monomer breakthrough curve through SEC quantification of the aggregate in the breakthrough fractions. Figure 6.2A shows that the monomer exited the column earlier than the aggregate, as it not only bound more weakly to the column but was also displaced by the more strongly-bound aggregate. Because the displacement of the monomer by the aggregate is a result of their differing affinities to the resin, enhancing the contrast in their affinities can improve separation.

The affinity of protein binding to an adsorbent is dictated by factors pertaining to the protein, adsorbent, and the environment. Distinct proteins have different affinities to a resin, which results in the species with the weaker affinity exiting the column earlier and at a higher relative concentration. However, considering that aggregates are formed from monomers, monomers and oligomers can have similar isoelectric points and affinities for CEX resins. Therefore the buffer conditions

employed here were chosen to enhance the subtle differences in their affinities. Figure 6.2A shows that the breakthrough curves of the monomers and the aggregates at pH 5.0 were close to one another, indicating that displacement was not pronounced at pH 5.0. Increasing the pH to 5.5 and 5.75 delayed aggregate breakthrough, indicating a greater displacement of the monomer by the aggregate. However, increasing the pH further to 6.2 did not further enhance the displacement, as the overall affinity of the sample to the resin was reduced. Figure 6.2A therefore indicates that optimal displacement occurs at an intermediate binding strength, where the contrast in the affinities of the two components is most pronounced. More generally, Figure 6.2A indicates that pH can be used as a handle to promote displacement, which can result in improved aggregate separation as reported (Reck et al., 2017; Stone et al., 2019).

Apart from the buffer conditions, the sample residence time or flow rate can also impact displacement through its effect on mAb transport. Figure 6.2B shows the effect of residence time on the efficiency by which aggregate displaces monomer by quantifying the aggregate content in the breakthrough pool. Decreasing the linear velocity to 100 cm/hr enhanced aggregate separation by largely eliminating transport limitations, and decreasing the flow rate further did not improve the separation of aggregates.

Figure 6.2C shows that batch contacting is inadequate to exploit competitive adsorption enough to obtain a practical reduction in the solution aggregate content over time. Although the protein residence time impacts the extent of displacement, the displacement is inadequate to achieve meaningful enrichment even at long times because the batch experiment lacks the spatial dimension that allows the phenomenon to develop further. As a sample is fed to a column, the top portion of the column

becomes saturated. Despite this saturation, when additional sample is fed, the incoming component with a higher affinity displaces the bound component with a lower affinity, initially near the top but progressing along the length of the column. Such zone development is intrinsic to displacement chromatography (Frenz and Horváth, 1985) and has been demonstrated for displacement of charge variants of the same mAb on the same resin previously (Khanal et al., 2019a).

6.3.2 Aggregate separation by displacement using sample recycling

Given the development of displacement zones with passage of the sample through the column, recycling of the column effluent was explored to promote additional removal of the most strongly-bound component, i.e., aggregate. A volume of sample equivalent to 10 times the capacity of the column was fed to ensure initial saturation, then recycling was used to promote competition and displacement. Ideally, the 1.4% aggregates should bind preferentially and displace any monomer while leaving residual capacity for 8.6% monomer, resulting in < 10% loss of monomer yield upon disposal of the bound sample. Figure 6.2D shows the reduction in aggregate content in the column effluent across three rounds of recycling at feed concentrations of 4.3 and 12.3 mg/mL, with both experiments conducted at a linear velocity of 300 cm/hr and a total feed mass of 71 mg. Despite a three-fold difference in starting sample concentration, the impurity removal is similar after three rounds of recycling. Another advantage of this set up is the lack of purity/yield trade-off. As indicated in the right ordinate of Figure 6.2D, recirculation across a small column does not change the yield [approximately 90%] significantly, as the only product discarded is that bound to the fixed bed of resin.

Figure 6.2D also shows that a lower sample concentration results in less aggregate reduction with successive rounds of recycling. In an attempt to exploit this effect, the column effluent was concentrated using a TFF device before being reloaded onto the column, but this did not improve aggregate removal (red triangular point in Figure 6.2E). Further investigation of sample concentration during recycling confirmed that a lower concentration is conducive to the displacement of the monomer by the aggregate (Figure 6.2E). This is likely due to a longer loading time incurred under a lower sample concentration using a fixed flow rate and fixed sample mass. Understanding the effect of sample concentration, buffer conditions, and transport parameters on displacement allows displacement to be optimized.

6.3.3 Aggregate separation by displacement using a multicolumn setup

Once conditions conducive to displacement are chosen, it is possible to segregate and extract the displaced components. This can be achieved by performing displacement chromatography for a sample containing two or more components in a multi-column mode. In an ideal scenario, multiple columns of appropriate lengths can be connected in series to allow extraction of zones in each of which one component is enriched. A schematic of such a method with a three-columns-in-series setup is shown in Figure 6.1B. Because the aggregate has a higher affinity than the monomer to the CEX column, the aggregate was retained primarily on the first column, albeit not entirely, partially due to transport limitations, as seen in the shallow breakthrough curves in Figure 6.2A. After sample loading, these columns were washed together, then eluted separately. To obtain a product with less aggregate, only the bound protein from columns 2 and 3 was recovered by elution, as shown in the schematic and the elution chromatogram in Figure 6.3A-B. More sample was then loaded onto column 1

with columns 2 and 3 in series for further aggregate accumulation in column 1. This approach allows the aggregate to be accumulated on column 1 with increasing feed, improving the recovery. Indeed, after 7 rounds of feed into the three-column setup, column 1 contained 10% of aggregate. In addition, Figure 6.3C shows a relatively higher concentration of the aggregate in column 2 compared to column 3, demonstrating that the aggregate consistently displaces the monomer from column 2 to 3 across cycles. As expected, increasing rounds of loading onto a fixed-bed column result in a trade-off between aggregate removal and recovery, as shown in Figure 6.3D. Such a representation gives an indication of the productivity and capacity possible using the three-column setup.

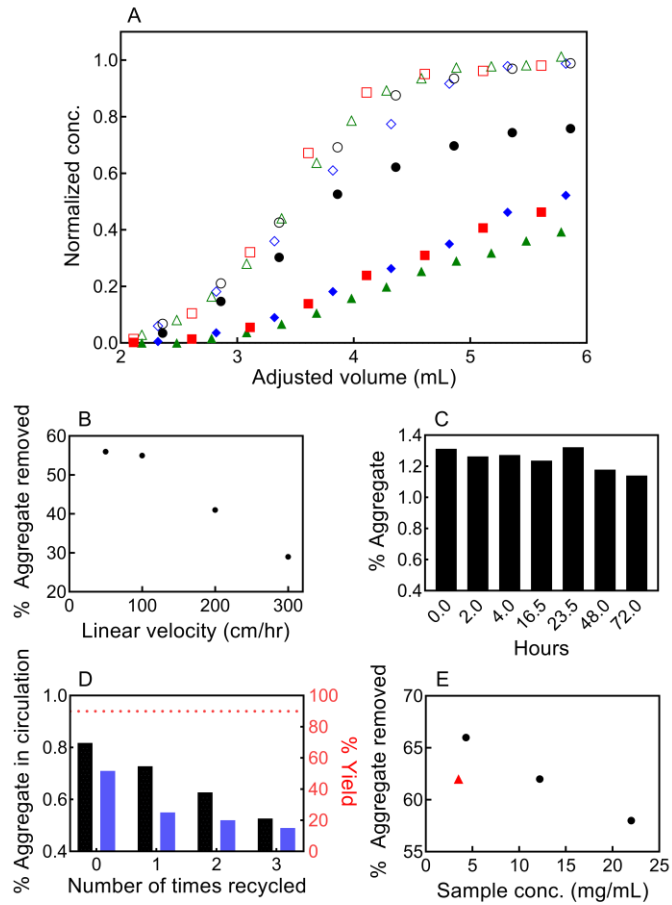


Figure 6.2 (A) mAb breakthrough curves generated at 300 cm/hr using 32 mM ionic strength acetate buffer, pH 5 (black circles), 5.5 (red rectangles), and 5.75 (green triangles), and 12 mM ionic strength phosphate buffer, pH 6.2 (blue diamonds). The open and closed symbols represent the monomer and the aggregate, respectively. The abscissa has been adjusted to align the monomer breakthrough curves for ease of comparison. (B) Dependence of monomer displacement and thus aggregate removal on linear velocity determined from breakthrough data. (C) Aggregate content in the solution outside the dialysis device measured over time for the batch experiment depicted in Figure 6.1A at 35 mM ionic strength, pH 5.75. (D) Aggregate content in the tubing depicted in Figure 6.1C, across rounds of recycling. The black and blue bars depict % aggregate for feed concentrations of 12.3 and 4.3 mg/mL, respectively, while the dotted red line represents the yield for both. (E) The effect of sample concentration on aggregate removal using recycling (Figure 6.1C) is represented by black circles, while the recycle and concentrate approach at a starting concentration of 3.5 mg/mL is depicted by the red triangle.

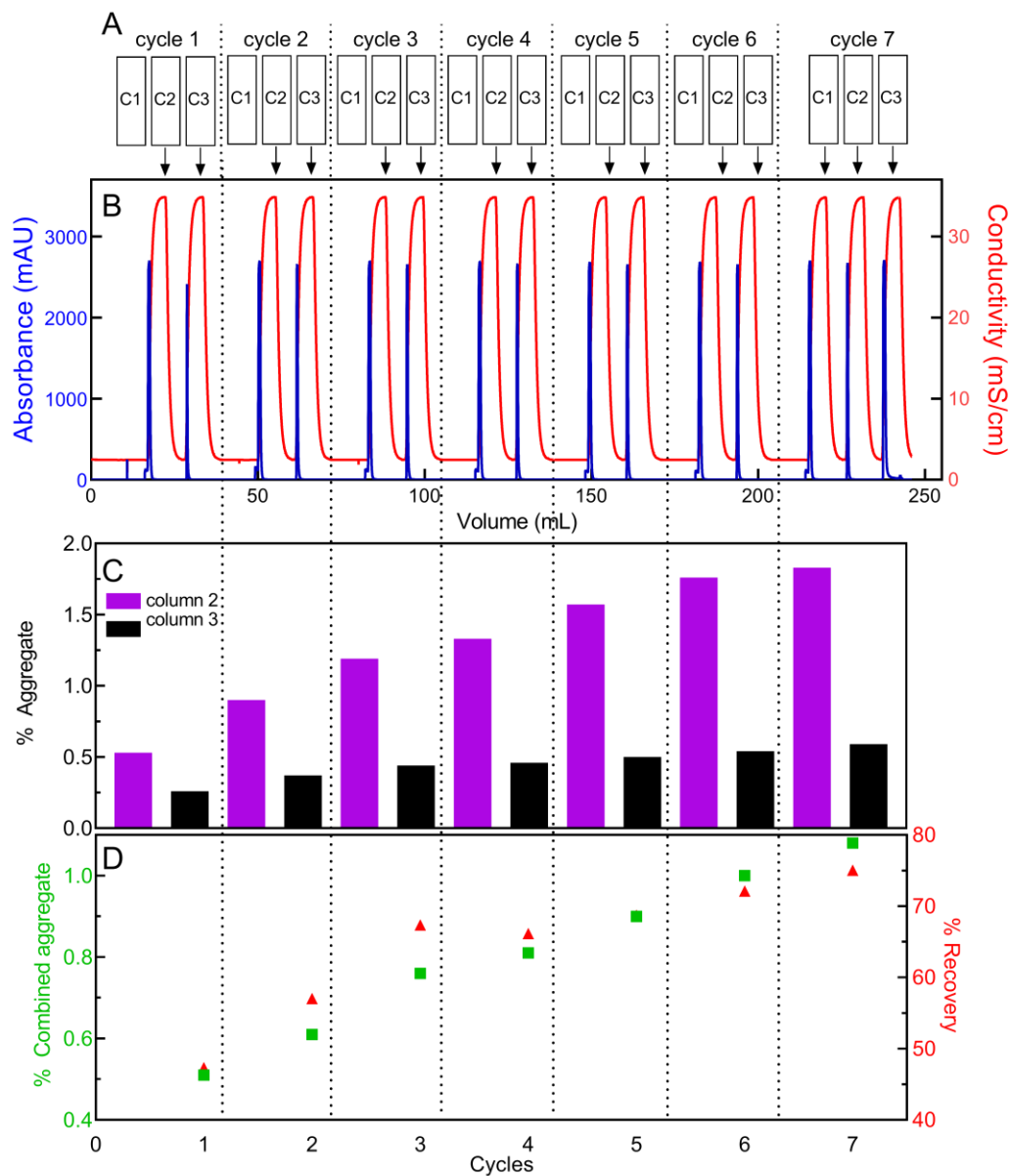


Figure 6.3 Elution schematic (A) and chromatogram (B) for the three-column approach depicted in Figure 6.1B. The aggregate content in elution from each column across different cycles is presented in (C), while the combined aggregate content between column 2 and 3 and the recovery from those two columns for the respective cycles are presented in (D).

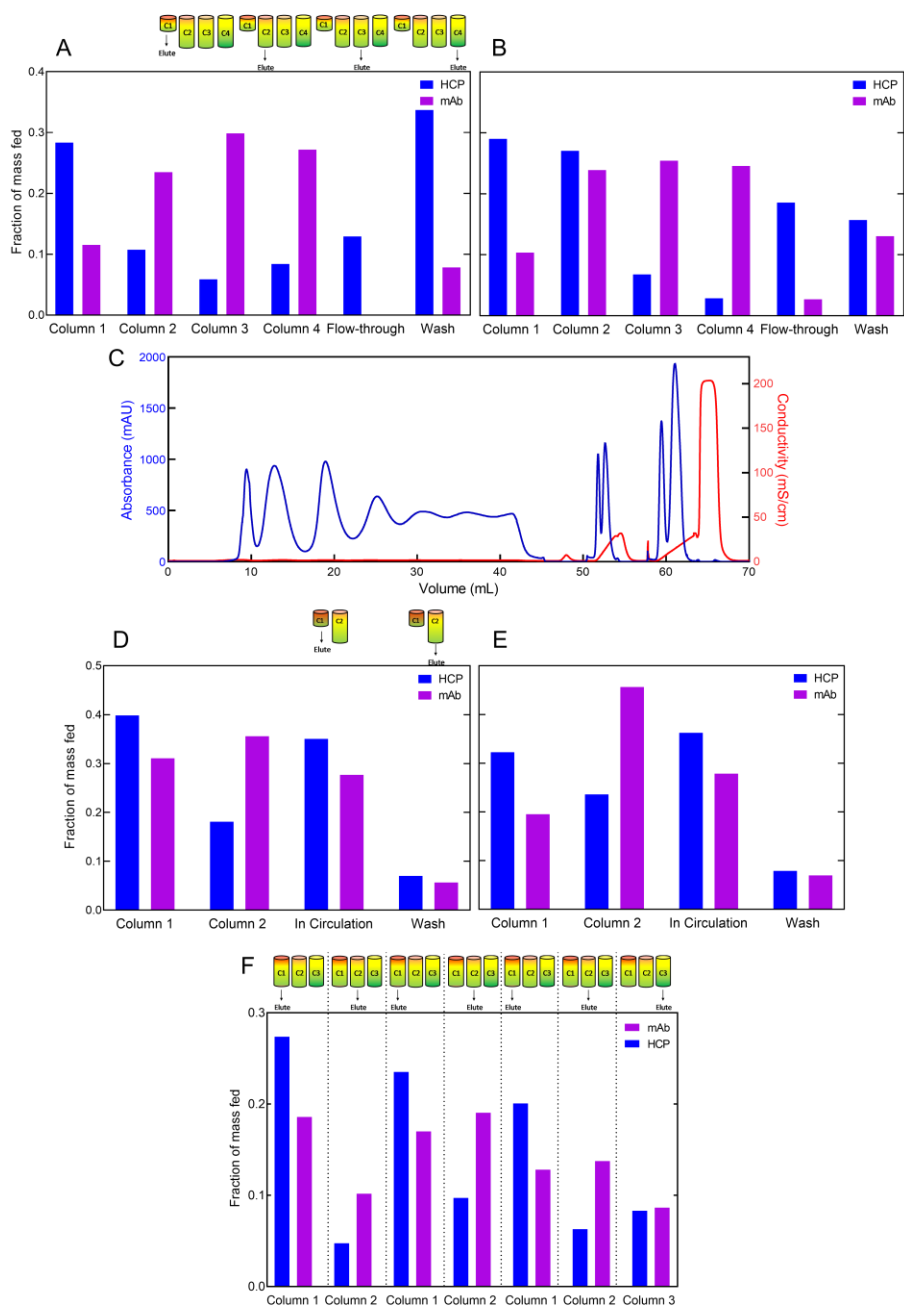


Figure 6.4 HCP and mAb content in the column eluates of four-column set-up depicted in Figure 6.1E with a starting HCP concentration of 20 ppm (A) and 1630 ppm (B), two-column recycling approach depicted in Figure 6.1F with a starting HCP concentration of 23 (D) and 1558 ppm (E), and three-column set-up depicted in Figure 6.1D (F). The chromatogram for the two-column recycling set-up depicted in Figure 6.1F is shown in (C).

6.3.4 HCP separation by displacement

The displacement of HCPs is relatively difficult to establish using the breakthrough method employed for the mAb aggregate as it would require large quantities of HCPs. However, the distribution of HCPs along the length of a column can be determined using a multi-column-in-series setup, which allows for the investigation of HCP displacement. The displacement separation of low-prevalence (20-1630 ppm) HCPs in the various multi-column set-ups outlined in Figure 6.1D-F was evaluated. A four-column-in-series set-up with a small first column was implemented to capture the HCPs displacing the mAb and those displaced by the mAb on the first column and in the flow-through, respectively. Furthermore, the distribution of the remaining HCPs, which have affinities to the resin that are closer to that of the mAb, could be evaluated within the second, third, and fourth columns.

Figures 6.4A and B show the normalized HCP and mAb content of the eluates from the four-columns-in-series set-up depicted in Figure 6.1E, obtained using HCP feed concentrations of 20 and 1630 ppm of the mAb concentration, respectively. The bars from the left to the right of the figures represent the migration end-points of HCPs starting from the top to the bottom and ultimately into the flow-through of what is essentially a long column. The bars on the left, reflecting amounts near the start of the series of columns, represent the relatively more basic group of HCPs that bind more strongly to the resin, while the bars on the right (end of series of columns) represent the relatively more acidic group of HCPs that bind more weakly to the resin. Since the sample contains a diverse population of HCPs with varying charge properties, only a small fraction of the HCP is seen in the flow-through. That the U-shaped distribution is asymmetric is reasonable given that the pI distribution of CHO HCP in harvest is skewed toward the acidic side (Jin et al., 2010). Despite the first column being half the

size of the second column, its HCP content is more than twice that in the second column (Figure 6.4A). This is due partly to the intrinsic retention behavior of the more basic HCPs but also to their displacement of the mAb as well as the displacement by the mAb of the more acidic HCPs. Although the HCPs are present in small quantities, displacement zones develop due to the presence of a large amount of the mAb. Figure 6.4A confirms that each column carries a high load of mAb; in the absence of this excess mAb, workable zone development would not be observed. That displacement then occurs is due to the differential binding affinities among the HCP components and between them and the mAb. Figure 6.4B shows that increasing the feed concentration by ~80-fold results in carryover of the HCP from the first column into the second column and into the flow-through. In contrast to the HCPs, the mAb is concentrated in the center of the multi-column system, flanked by the HCP-heavier regions toward the top and bottom of the column series.

To further establish that displacement of mAb and HCPs is indeed occurring throughout the length of the column and that it is not merely a representation of the pI distribution of the HCPs, a two-column recycling system (Figure 6.1F) was set up. Figures 6.4D-E show that this approach results in similar HCP and mAb distributions as the four-column-in-series set-up. The results in Figures 6.4D and E were obtained with HCP feed concentrations of 23 and 1558 ppm, respectively. In both cases, more HCP was found in column 1 and in circulation than in column 2, whereas more mAb was found in column 2 than in column 1 and in circulation. When the HCP feed concentration was increased 68-fold, the displacement of the mAb from column 1 to column 2 by the additional HCP could be clearly seen through the lower mAb content in column 1 of Figure 6.4E compared to that of Figure 6.4D. Furthermore,

displacement of the mAb by the relatively more basic HCPs was also seen using a three-column displacement chromatography set-up with cyclic feeding (Figure 6.1D). Figure 6.4F shows the HCP content in the eluates across three cycles. The HCP content in column 1 was consistently greater than that in column 2 across all cycles due to the displacement of the mAb by the relatively basic HCPs. However, because additional sample amounting to 66% of the initial feed was fed to the system through each cycle, the HCP carried over from the first column into the second column in cycles 2 and 3.

All three methods outlined above demonstrate that HCP zones formed along the length of the multi-column system during sample loading. Though the HCPs were present in minuscule quantity, the broad differences in their isoelectric points and hence their binding affinities suggest displacement as the mechanism behind their separation. The displacement became particularly apparent when more sample was loaded, or recycling was employed.

6.3.5 Significance of displacement in multi-column systems

The utility of separation by means of displacement extends beyond the separation of binary mixtures to separation of multiple groups of proteins based on trends in binding affinity. Our previous (Khanal et al., 2019a) and current findings show that displacement results in zone development across serially-connected columns, of which the early zone includes aggregates, basic charge variants, and more basic HCPs, while the later zone includes acidic charge variants and more acidic HCPs. Such zone development is conducive to the separation of the product, which is enriched in the center of the multicolumn system. The ability to remove low prevalence HCPs based on displacement is particularly attractive, given the growing

concern over the persistent presence of difficult-to-remove HCPs (Levy et al., 2014; Levy et al., 2016; Vanderlaan et al., 2018). Fortunately, displacement is inherently present in all column operations and can especially benefit continuous chromatography operations, in which sample application can proceed beyond the point of DBC.

The benefit of displacement is realized once breakthrough occurs in a column, surpassing the point of DBC. Figure 6.2A shows that early breakthrough fractions are enriched in the monomer as the aggregate preferentially binds to the column. As adsorption proceeds beyond resin saturation locally, competition ensues, leading to the displacement of bound monomer by incoming aggregates or basic species. Overloading is achieved in the methods outlined above via substantial loading across a small column or across multi-column systems. The recycling method presented in Figure 6.1C provides a proof-of-concept demonstration of how displacement can be enhanced significantly, although extending the duration over which proteins remain bound to a column may lead to protein conformational changes (Corbett et al., 2013; Gillespie et al., 2012; Gospodarek et al., 2014; Guo and Carta, 2015). Overloading across the columns saturates the columns serially, promotes displacement, and enhances separation. We demonstrate that accounting for displacement can further help continuous chromatography surpass batch chromatography in separation performance.

6.4 Conclusions

Although cation-exchange chromatography is routinely employed for impurity separation, the effect of displacement during sample application on the separation performance is seldom leveraged or highlighted. Whether explicitly stated or not,

methods employing self-displacement chromatography are gradually (Brown et al., 2010; Ichihara et al., 2018; Ichihara et al., 2019; Khanal et al., 2019a; Liu et al., 2011; Vogg et al., 2020b; Vogg et al., 2020a) emerging as they offer higher productivity with similar and adaptable sequences of operations. We have demonstrated various chromatography design strategies for the enhancement of displacement between the mAb product and aggregates and HCPs on CEX resins. These include a combination of overloading, recycling, and continuous multi-column approaches. The development of displacement zones along the length of the column makes displacement chromatography particularly suitable for continuous chromatography designs where multiple smaller columns are preferred. Differently enriched zones along multiple columns, such as the U-shaped distribution of HCPs with enriched mAb in between, as obtained here, enables intentional and efficient fractionation of a more pure product. Such findings indicate that a collection of impurities, comprising aggregates and basic charge variant and HCPs, displace the product and thus precede the product-enriched zone in the system, while acidic variants and HCPs can be captured or allowed to flow through further downstream. Such zone development is contingent upon overloading onto smaller columns, which also has the benefit of enabling higher resin utilization and improving yield; this translates to significant cost saving across the entire bioprocessing train as a smaller footprint is required. Our evaluation of the effect of the operational parameters such as protein residence time and protein concentration on displacement can also allow for better process control strategies.

Chapter 7

CONCLUSIONS AND RECOMMENDATIONS

The performance of adsorptive purification processes depends firstly on the adsorption equilibrium between the adsorbate and the adsorbent and secondly on the transport of the adsorbate to the adsorption site. The thesis addresses biomacromolecular adsorption and transport in five studies. The first two analyze structure-function relationships of depth filters and the last three bring innovations to ion-exchange chromatography through engineering analysis of competitive adsorption and surface diffusion.

Both cell-culture harvest clarification and therapeutic protein product polishing steps are primarily carried out using unit operations such as filters and chromatographic resins. It is essential to understand whether and how the sample binds to the adsorbent to select an appropriate adsorbent, predict its performance, and ultimately control and automate the unit operation. To this end, characterization of the depth filter and evaluation of its adsorptive capacity for various proteins and mechanisms for nucleic acid retention is presented in Chapters 2 and 3. The importance of diffusion of the bound protein along the adsorbent surface in protein uptake into chromatographic resin beads is substantiated in Chapter 4. This work shows that the protein diffusivity on a charged surface depends explicitly on its affinity to the surface. Finally the importance of enhancing and exploiting the differences in the affinities of distinct or highly similar proteins for their superior separation is demonstrated in Chapters 5 and 6. For each topic outlined above, the

conclusions followed by the recommendations for future investigations are given below in subsequent paragraphs.

The multiple components comprising a depth filter make decoupling of the mechanisms by which various impurities, such as proteins, nucleic acids, and cellular debris, are bound and removed, difficult. To this end, the adsorption of model proteins and mAbs onto depth filters and their components to measured properties such as surface area, morphology, surface charge density, and composition is correlated in Chapter 2. Our results corroborate the importance of the binder in dictating the adsorptive ability of depth filter using a diverse tool set, such as nitrogen sorption measurements, SEM, light scattering, titration and confocal microscopy. In addition, our work with the filter aids and the composite depth filters raises questions regarding the current approach to depth filter selection in bioprocessing. The resin binder's dual role as the depth filter adhesive and an adsorptive coating suggest that its charge characteristic along with its surface wettability is of interest. Furthermore, the selection of the polymeric binder should be informed by the pI of the drug target and the range of the pIs of the majority of the appropriate host cell proteins. Lastly, it may be desirable, in certain cases, to determine ways to utilize the anion charge of the filter aids that are abundant in the depth filter.

An extension of the current work could include the evaluation of HCP adsorption and clearance using proteomic methods (Gilgunn et al., 2019). The polymeric resin binder, a critical component, was found to be the primary contributor to the depth filter's adsorptive functionality. Because the evaluated depth filters contain cationic but not anionic polymers, the impurity clearance of new depth filters comprising both charge characteristics (Onur et al., 2019) could be explored in the

future. Furthermore, the depth filter's capacity for proteins that adsorb was found to be well estimated from its total surface area. Correlation of depth filter capacity to protein biophysical characteristics and binding orientation would add to the current understanding.

In addition to protein adsorption, this dissertation investigates the mechanisms by which double-stranded DNA (dsDNA) is retained on depth filters. The retention of DNA on depth filters was visualized using confocal microscopy and found that genomic DNA and longer lengths of DNA are primarily excluded on the surface, while short oligos are able to adsorb throughout the depth filter. DNA from a small harvest was also retained on the surface suggesting DNA during harvest clarification is lengthy and cleared primarily through exclusion. Finally, it was found that DNA displaces further into the filter with an increase in amount, flux or volume of buffer. These findings can be leveraged in further improving the design of depth filter and in the design of various filtration media for DNA purification.

Future efforts should evaluate the DNA retention profile in an industrial spent depth filter through the selective staining of DNA to complement the current results. The experimental approaches and techniques employed in this work can aid in the analysis of other depth filter impurity and product retention profiles. In particular, the presented microscopy experiments can be adapted for in-situ analysis of impurity retention.

Protein adsorbent affinity can impact protein transport, apart from dictating the adsorption capacity. An original method to alleviate protein mass-transfer limitations is proposed in Chapter 4. The work shows that diffusion of a protein on a charged surface depends explicitly on its affinity to the surface. The sample-loading method

modulates the buffer ionic strength for transient control of protein surface diffusion and hence overall transport during protein loading. The impact of the gradient loading method on the nanoscale protein distribution within the resin was characterized by small-angle neutron scattering. The findings not only support the prevalence of surface diffusion in IEX but also validate the gradient method, which leverages it in promoting IEX resin utility by 43%. The methodologies developed and employed in this work can be adapted for the analysis of the impact of a variety of constant- or variable-condition protein-loading parameters on protein uptake and spatial distribution in commercial or custom-designed resin beads.

In the future, in-situ investigation of the sample under gradient loading would provide additional data that may be modeled to gain greater mechanistic insight. The investigation of protein mobility inside the resin beads may also be extended to include dynamic neutron or x-ray scattering techniques. More generally, current methodology and findings in the realm of chromatography may be extended to other adsorptive systems with mass-transfer limitations, such as immunosensors and microfluidic devices.

While a sample application method to alleviate protein mass-transfer limitations is presented in Chapter 4, how to capture the protein lost from mass-transfer limitations using multiple columns is demonstrated in Chapter 5 and 6. Using experiments and mechanistic modeling, competitive adsorption can be promoted to separate even highly similar mAb isoforms effectively. In addition to an optimal ionic environment, saturated loading enhances the displacement of a more weakly-binding adsorbate by a more strongly-binding competitor. Displacement chromatography also potentially mitigates on-column unfolding (Corbett et al., 2013; Gillespie et al., 2012;

Gospodarek et al., 2014; Guo and Carta, 2014; Guo and Carta, 2015) through weaker product binding, a hypothesis for future investigation. The evaluated effect of the operational parameters on displacement can assist in developing process control strategies. Furthermore, the multicolumn setups employed in Chapters 5 and 6 allow capture of the breakthrough from a column on the next column, enabling continuous loading and full utilization of the resin capacity. The proposed designs have been shown to enhance displacement among mAb charge variants, mAb aggregates, and host-cell proteins.

Future efforts adapting the current designs for continuous operation can steer efficient usage of equipment and labor while purifying the product more consistently and efficiently at a reduced cost. Chromatography methods with smaller footprints, such as the methods mentioned above, have yet to be widely adopted because of concerns about the complexity of the equipment setup (Subramanian, 2017). However, mechanistic models, such as those used here, can alleviate the risks and aid in process development.

This dissertation addresses how adsorbate-adsorbent affinity and competitive adsorption affect the adsorbate's binding capacity, transport, and separation. Using our understanding of the principles above, innovative yet translatable methods are proposed in the fields of depth filtration and ion-exchange chromatography. The methodologies developed and employed here can be adapted to investigate and enhance the performance of filtration, chromatography, and other applications.

REFERENCES

- 3M. 2013. 3M solutions for biopharmaceutical process development , manufacturing and process monitoring. *Catalog*.
<http://multimedia.3m.com/mws/media/4936270/3m-biopharmaceutical-catalog.pdf>.
- Aboulaich N, Chung WK, Thompson JH, Larkin C, Robbins D, Zhu M. 2014. A novel approach to monitor clearance of host cell proteins associated with monoclonal antibodies. *Biotechnol. Prog.* **30**:1114–1124.
- Aggarwal S. 2010. What’s fueling the biotech engine-2009-2010. *Nat. Biotechnol.* **28**:1165–1171.
- Agner E. 2003. Method of displacement chromatography. *US Pat.* 4,575,330. USA 6576134 B1. <https://patents.google.com/patent/US6576134B1/en>.
- Alothman ZA. 2012. A review: Fundamental aspects of silicate mesoporous materials. *Materials (Basel)*. **5**:2874–2902.
- An Z. 2018. “Magic Bullets” at the center stage of immune therapy: a special issue on therapeutic antibodies. *Protein Cell* **9**:1–2.
- Arai T, Norde W. 1990. The behavior of some model proteins at solid-liquid interfaces 1. Adsorption from single protein solutions. *Colloids and Surfaces* **51**:1–15.
- Arosio P, Rima S, Morbidelli M. 2013. Aggregation mechanism of an IgG2 and two IgG1 monoclonal antibodies at low pH: From oligomers to larger aggregates. *Pharm. Res.* **30**:641–654.
- Asthagiri D, Lenhoff AM. 1997. Influence of structural details in modeling electrostatically driven protein adsorption. *Langmuir* **13**:6761–6768.
- Bailey-Kellogg C, Gutiérrez AH, Moise L, Terry F, Martin WD, De Groot AS. 2014. CHOPPI: A web tool for the analysis of immunogenicity risk from host cell proteins in CHO-based protein production. *Biotechnol. Bioeng.* **111**:2170–2182.

- Basconi JE, Carta G, Shirts MR. 2014. Multiscale modeling of protein adsorption and transport in macroporous and polymer-grafted ion exchangers. *AIChE J.* **60**:3888–3901.
- Beatson R, Sproviero D, Maher J, Wilkie S, Taylor-Papadimitriou J, Burchell JM. 2011. Transforming growth factor- β 1 is constitutively secreted by chinese hamster ovary cells and is functional in human cells. *Biotechnol. Bioeng.* **108**:2759–2764.
- Bee JS, Tie L, Johnson D, Dimitrova MN, Jusino KC, Afdahl CD. 2015. Trace levels of the CHO host cell protease cathepsin D caused particle formation in a monoclonal antibody product. *Biotechnol. Prog.* **31**:1360–1369.
- Bergna HE, Roberts WO eds. 2005. Colloidal silica: fundamentals and applications. CRC Press 248 p.
- Berman HM, Battistuz T, Bhat TN, Bluhm WF, Bourne PE, Burkhardt K, Feng Z, Gilliland GL, Iype L, Jain S, Fagan P, Marvin J, Padilla D, Ravichandran V, Schneider B, Thanki N, Weissig H, Westbrook JD, Zardecki C. 2002. The protein data bank. *Acta Crystallogr. Sect. D Biol. Crystallogr.* **58**:899–907.
- Bethea D, Wu SJ, Luo J, Hyun L, Lacy ER, Teplyakov A, Jacobs SA, O’Neil KT, Gilliland GL, Feng Y. 2012. Mechanisms of self-association of a human monoclonal antibody CNTO607. *Protein Eng. Des. Sel.* **25**:531–537.
- Bhambure R, Angelo JM, Gillespie CM, Phillips M, Graalfs H, Lenhoff AM. 2017. Ionic strength-dependent changes in tentacular ion exchangers with variable ligand density. II. Functional properties. *J. Chromatogr. A* **1506**:55–64.
- Bhambure R, Gillespie CM, Phillips M, Graalfs H, Lenhoff AM. 2016. Ionic strength-dependent changes in tentacular ion exchangers with variable ligand density. I. Structural properties. *J. Chromatogr. A* **1463**:90–101.
- Borg N, Brodsky Y, Moscariello J, Vunnum S, Vedantham G, Westerberg K, Nilsson B. 2014. Modeling and robust pooling design of a preparative cation-exchange chromatography step for purification of monoclonal antibody monomer from aggregates. *J. Chromatogr. A* **1359**:170–181.
- Borochoy N, Eisenberg H, Kam Z. 1981. Dependence of DNA conformation on the concentration of salt. *Biopolymers* **20**:231–235.
- Bowes BD, Lenhoff AM. 2011. Protein adsorption and transport in dextran-modified ion-exchange media. III. Effects of resin charge density and dextran content on

- adsorption and intraparticle uptake. *J. Chromatogr. A* **1218**:7180–7188.
- Brouwer I, Sitters G, Candelli A, Heerema SJ, Heller I, Melo De AJ, Zhang H, Normanno D, Modesti M, Peterman EJG, Wuite GJL. 2016. Sliding sleeves of XRCC4-XLF bridge DNA and connect fragments of broken DNA. *Nature* **535**:566–569.
- Brown A, Bill J, Tully T, Radhamohan A, Dowd C. 2010. Overloading ion-exchange membranes as a purification step for monoclonal antibodies. *Biotechnol. Appl. Biochem.* **56**:59–70.
- Brown D, Kienzle P. 2015. Neutron activation and scattering calculator. <https://www.ncnr.nist.gov/resources/activation/>.
- Brühlmann D, Jordan M, Hemberger J, Sauer M, Stettler M, Broly H. 2015. Tailoring recombinant protein quality by rational media design. *Biotechnol. Prog.* **31**:615–629.
- Brunauer S, Deming LS, Deming WE, Teller E. 1940. On a theory of the van der waals adsorption of gases. *J. Am. Chem. Soc.* **62**:1723–1732.
- Budd PM, Makhseed SM, Ghanem BS, Msayib KJ, Tattershall CE, McKeown NB. 2004. Microporous polymeric materials. *Mater. Today* **7**:40–46.
- Buyel JF, Gruchow HM, Fischer R. 2015. Depth filters containing diatomite achieve more efficient particle retention than filters solely containing cellulose fibers. *Front. Plant Sci.* **6**:1134.
- Carta G, Jungbauer A. 2010. Protein chromatography: process development and scale-up. *Protein Chromatogr. Process Dev. Scale-Up*. John Wiley & Sons.
- Castellanos MM, Clark NJ, Watson MC, Krueger S, McAuley A, Curtis JE. 2016. Role of omlecular flexibility and colloidal descriptions of proteins in crowded environments from small-angle scattering. *J. Phys. Chem. B* **120**:12511–12518.
- Chang C, Lenhoff AM. 1998. Comparison of protein adsorption isotherms and uptake rates in preparative cation-exchange materials. *J. Chromatogr. A* **827**:281–293.
- Charlton HR, Relton JM, Slater NKH. 1998. DNA from clarified, large-scale, fed-batch, mammalian cell culture is of predominantly low molecular weight. *Biotechnol. Lett.* **20**:789–794.

- Charlton HR, Relton JM, Slater NKH. 1999. Characterisation of a generic monoclonal antibody harvesting system for adsorption of DNA by depth filters and various membranes. *Bioseparation* **8**:281–291.
- Chennamsetty N, Voynov V, Kayser V, Helk B, Trout BL. 2009. Design of therapeutic proteins with enhanced stability. *Proc. Natl. Acad. Sci. U. S. A.* **106**:11937–11942.
- Choi JG, Do DD, Do HD. 2001. Surface diffusion of adsorbed molecules in porous media: Monolayer, multilayer, and capillary condensation regimes. *Ind. Eng. Chem. Res.* **40**:4005–4031.
- Chollangi S, Parker R, Singh N, Li Y, Borys M, Li Z. 2015a. Development of robust antibody purification by optimizing protein-A chromatography in combination with precipitation methodologies. *Biotechnol. Bioeng.* **112**:2292–2304.
- Chollangi S, Parker R, Singh N, Li Y, Borys M, Li Z. 2015b. Development of robust antibody purification by optimizing protein-A chromatography in combination with precipitation methodologies. *Biotechnol. Bioeng.* **112**:2292–2304.
- Chu B. 1970. Laser light scattering. *Annu. Rev. Phys. Chem.* **21**:145–174.
- Chung S, Tian J, Tan Z, Chen J, Lee J, Borys M, Li ZJ. 2018. Industrial bioprocessing perspectives on managing therapeutic protein charge variant profiles. *Biotechnol. Bioeng.* **115**:1646–1665.
- Claman H. 1963. Tolerance to a protein antigen in adult mice and the effect of nonspecific factors. *J. Immunol.* **91**:833–839.
- Corbett R, Carta G, Iskra T, Gallo C, Godavarti R, Salm JR. 2013. Structure and protein adsorption mechanisms of clean and fouled tentacle-type anion exchangers used in a monoclonal antibody polishing step. *J. Chromatogr. A* **1278**:116–125.
- Creighton TE. 1985. Proteins: Structures and molecular properties. *Trends Biochem. Sci.* 2nd ed. W.H Freeman and Company. Vol. 10 82 p.
- Curtis JE, Nanda H, Khodadadi S, Cicerone M, Lee HJ, McAuley A, Krueger S. 2012. Small-angle neutron scattering study of protein crowding in liquid and solid phases: Lysozyme in aqueous solution, frozen solution, and carbohydrate powders. *J. Phys. Chem. B* **116**:9653–9667.

- Debye P, Anderson HR, Brumberger H. 1957. Scattering by an inhomogeneous solid. II. the correlation function and its application. *J. Appl. Phys.* **28**:679–683.
- Debye P, Bueche AM. 1949. Scattering by an inhomogeneous solid. *J. Appl. Phys.* **20**:518–525.
- Deniz A. 2007. Probing nanoscale structure and dynamics of amyloidogenic proteins using single-molecule fluorescence. *Nanomedicine Nanotechnology, Biol. Med.* **3**:342.
- Dixit N, Salamat-Miller N, Salinas PA, Taylor KD, Basu SK. 2016. Residual host cell protein promotes polysorbate 20 degradation in a sulfatase drug product leading to free fatty acid particles. *J. Pharm. Sci.* **105**:1657–1666.
- Dorsey N, Eschrich J, Cyr G. 1997. The role of charge in the retention of DNA by charged cellulose-based depth filters. *BioPharm* **10**:46–49.
- Dunne O, Weidenhaupt M, Callow P, Martel A, Moulin M, Perkins SJ, Haertlein M, Forsyth VT. 2017. Matchout deuterium labelling of proteins for small-angle neutron scattering studies using prokaryotic and eukaryotic expression systems and high cell-density cultures. *Eur. Biophys. J.* **46**:425–432.
- Dziennik SR, Belcher EB, Barker GA, Lenhoff AM. 2005. Effects of ionic strength on lysozyme uptake rates in cation exchangers. I: Uptake in SP sepharose FF. *Biotechnol. Bioeng.* **91**:139–153.
- Ellis F. 1953. Handbook of radiotherapy. *Bmj* **1**:770.
- Esfandiary R, Hayes DB, Parupudi A, Casas-finet J, Bai S, Samra HS, Shah AU, Sathish HA. 2013. A systematic multitechnique approach for detection and characterization of reversible self-association during formulation development of therapeutic antibodies. *J. Pharm. Sci.* **102**:62–72.
- Farnan D, Moreno GT. 2009. Multiproduct high-resolution monoclonal antibody charge variant separations by pH gradient ion-exchange chromatography. *Anal. Chem.* **81**:8846–8857.
- Farrar SR, Preston DR, Toranzos GA, Girard M, Erdos GA, Vasuhdivan V. 1991. Use of modified diatomaceous earth for removal and recovery of viruses in water. *Appl. Environ. Microbiol.* **57**:2502–2506.

- Feller BE, Kellis JT, Cascão-Pereira LG, Robertson CR, Frank CW. 2010. The role of electrostatic interactions in protease surface diffusion and the consequence for interfacial biocatalysis. *Langmuir* **26**:18916–18925.
- Frenz J, Horváth C. 1985. High performance displacement chromatography: Calculation and experimental verification of zone development. *AIChE J.* **31**:400–409.
- Gadam SD, Gallant SR, Cramer SM. 1995. Transient profiles in ion-exchange displacement chromatography. *AIChE J.* **41**:1676–1686.
- Gallant SR, Vunnum S, Cramer SM. 1996. Optimization of preparative ion-exchange chromatography of proteins: Linear gradient separations. *J. Chromatogr. A* **725**:295–314.
- Gallant SR, Cramer SM. 1997. Productivity and operating regimes in protein chromatography using low-molecular-mass displacers. *J. Chromatogr. A* **771**:9–22.
- Gamble CN. 1966. The role of soluble aggregates in the primary immune response of mice to human gamma globulin. *Int. Arch. Allergy Immunol.* **30**:446–455.
- Gao SX, Zhang Y, Stansberry-Perkins K, Buko A, Bai S, Nguyen V, Brader ML. 2011. Fragmentation of a highly purified monoclonal antibody attributed to residual CHO cell protease activity. *Biotechnol. Bioeng.* **108**:977–98.
- Garcia HG, Grayson P, Han L, Inamdar M, Kondev J, Nelson PC, Phillips R, Widom J, Wiggins PA. 2007. Biological consequences of tightly bent DNA: The other life of a macromolecular celebrity. *Biopolymers* **85**:115–130.
- Gerba CP, Hou K. 1985. Endotoxin removal by charge-modified filters. *Appl. Environ. Microbiol.* **50**:1375–1377.
- Gilgunn S, El-Sabbahy H, Albrecht S, Gaikwad M, Corrigan K, Deakin L, Jellum G, Bones J. 2019. Identification and tracking of problematic host cell proteins removed by a synthetic, highly functionalized nonwoven media in downstream bioprocessing of monoclonal antibodies. *J. Chromatogr. A* **1595**:28–38.
- Gillespie R, Nguyen T, Macneil S, Jones L, Crampton S, Vunnum S. 2012. Cation exchange surface-mediated denaturation of an aglycosylated immunoglobulin (IgG1). *J. Chromatogr. A* **1251**:101–110.
- Gilson MK, Honig BH. 1987. Calculation of electrostatic potentials in an enzyme

- active site. *Nature* **330**:84–6.
- Goerke AR, To BCS, Lee AL, Sagar SL, Konz JO. 2005. Development of a novel adenovirus purification process utilizing selective precipitation of cellular DNA. *Biotechnol. Bioeng.* **91**:12–21.
- Goldrick S, Joseph A, Mollet M, Turner R, Gruber D, Farid SS, Titchener-Hooker NJ. 2017. Predicting performance of constant flow depth filtration using constant pressure filtration data. *J. Memb. Sci.* **531**:138–147.
- Gospodarek AM, Hiser DE, O’Connell JP, Fernandez EJ. 2014. Unfolding of a model protein on ion exchange and mixed mode chromatography surfaces. *J. Chromatogr. A* **1355**:238–252.
- Griaud F, Winter A, Denefeld B, Lang M, Hensinger H, Straube F, Sackewitz M, Berg M. 2017. Identification of multiple serine to asparagine sequence variation sites in an intended copy product of LUCENTIS® by mass spectrometry. *MAbs* **9**:1337–1348.
- Griffith WL, Triolo R, Compere AL. 1987. Analytical scattering function of a polydisperse Percus-Yevick fluid with Schulz- (-) distributed diameters. *Phys. Rev. A* **35**:2200–2206.
- Griffiths E. 1997. WHO Expert Committee on Biological Standardization - Highlights of the meeting of October 1996. In: WHO, editor. *Biologicals*, Vol. 25, pp. 359–362.
- Gritti F, Guiochon G. 2011. Importance of sample intraparticle diffusivity in investigations of the mass transfer mechanism in liquid chromatography. *AIChE J.* **57**:346–358.
- Gritti F, Guiochon G. 2014. Mass transfer mechanism in chiral reversed phase liquid chromatography. *J. Chromatogr. A* **1332**:35–45.
- Guélat B, Ströhlein G, Lattuada M, Delegrange L, Valax P, Morbidelli M. 2012. Simulation model for overloaded monoclonal antibody variants separations in ion-exchange chromatography. *J. Chromatogr. A* **1253**:32–43.
- Gunawan F, Nishihara J, Liu P, Sandoval W, Vanderlaan M, Zhang H, Krawitz D. 2018. Comparison of platform host cell protein ELISA to process-specific host cell protein ELISA. *Biotechnol. Bioeng.* **115**:382–389.

- Guo J, Carta G. 2014. Unfolding and aggregation of a glycosylated monoclonal antibody on a cation exchange column. Part II. Protein structure effects by hydrogen deuterium exchange mass spectrometry. *J. Chromatogr. A* **1356**:129–137.
- Guo J, Carta G. 2015. Unfolding and aggregation of monoclonal antibodies on cation exchange columns: Effects of resin type, load buffer, and protein stability. *J. Chromatogr. A* **1388**:184–194.
- Gutka HJ, Yang H, Kakar S eds. 2017. Biosimilars: regulatory, clinical, and biopharmaceutical development. Springer 220–240 p.
- Guzman RZ, Carbonell RG, Kilpatrick PK. 1986. The adsorption of proteins to gas-liquid interfaces. *J. Colloid Interface Sci.* **114**:536–547.
- Hammermann M, Steinmaier C, Merlitz H, Kapp U, Waldeck W, Chirico G, Langowski J. 1997. Salt effects on the structure and internal dynamics of superhelical DNAs studied by light scattering and Brownian dynamics. *Biophys. J.* **73**:2674–2687.
- Hardin AM, Harinarayan C, Malmquist G, Axén A, van Reis R. 2009. Ion exchange chromatography of monoclonal antibodies: Effect of resin ligand density on dynamic binding capacity. *J. Chromatogr. A* **1216**:4366–4371.
- Harinarayan C, Mueller J, Ljunglöf A, Fahrner R, Van Alstine J, Van Reis R. 2006. An exclusion mechanism in ion exchange chromatography. *Biotechnol. Bioeng.* **95**:775–787.
- Harris LJ, Skaletsky E, McPherson A. 1998. Crystallographic structure of an intact IgG1 monoclonal antibody. *J. Mol. Biol.* **275**:861–872.
- Hernandez I, Bott SW, Patel AS, Wolf CG, Hospodar AR, Sampathkumar S, Shrank WH. 2018. Pricing of monoclonal antibody therapies: higher if used for cancer? *Am. J. Manag. Care* **24**:109–112.
- Hernandez R. 2015. Continuous manufacturing: A changing processing paradigm. *BioPharm Int.* **28**:20–41.
- Hodges RS, Burke TWL, Mant CT. 1991. Multi-column preparative reversed-phase sample displacement chromatography of peptides. *J. Chromatogr. A* **548**:267–280.

- Van Holten RW, Autenrieth SM. 2003. Evaluation of depth filtration to remove prion challenge from an immune globulin preparation. *Vox Sang.* **85**:20–24.
- Iammarino M, Nti-gyabaah J, Chandler M, Roush D, Göklen K. 2007. Impact of cell density and viability on primary clarification of mammalian cell broth-an analysis using disc-stack centrifugation and charged depth filtration. *Bioprocess Int.* **38**:38–50.
- Ichihara T, Ito T, Gillespie C. 2019. Polishing approach with fully connected flow-through purification for therapeutic monoclonal antibody. *Eng. Life Sci.* **19**:31–36.
- Ichihara T, Ito T, Kurisu Y, Galipeau K, Gillespie C. 2018. Integrated flow-through purification for therapeutic monoclonal antibodies processing. *MAbs* **10**:325–334.
- Jin M, Szapiel N, Zhang J, Hickey J, Ghose S. 2010. Profiling of host cell proteins by two-dimensional difference gel electrophoresis (2D-DIGE): Implications for downstream process development. *Biotechnol. Bioeng.* **105**:306–316.
- Jiskoot W, Van Hertrooij JJCC, Klein Gebbinck JWTM, Van der Velden-de Groot T, Crommelin DJA, Beuvery EC. 1989. Two-step purification of a murine monoclonal antibody intended for therapeutic application in man. Optimisation of purification conditions and scaling up. *J. Immunol. Methods* **124**:143–156.
- Johnsson B, Löfås S, Lindquist G. 1991. Immobilization of proteins to a carboxymethyl-dextran-modified gold surface for biospecific interaction analysis in surface plasmon resonance sensors. *Anal. Biochem.* **198**:268–277.
- Kalyani S, Priya JA, Rao PS, Krishnaiah A. 2005. Removal of copper and nickel from aqueous solutions using chitosan coated on perlite as biosorbent. *Sep. Sci. Technol.* **40**:1483–1495.
- Kaneki N, Xu Y, Kumari A, Halsall HB, Heineman WR, Kissinger PT. 1994. Electrochemical enzyme immunoassay using sequential saturation technique in a 20- μ l capillary: digoxin as a model analyte. *Anal. Chim. Acta* **287**:253–258.
- Khanal O, Kumar V, Lenhoff AM. 2020a. Displacement to separate host cell proteins and aggregates in cation-exchange chromatography of monoclonal antibodies. *Biotechnol. Bioeng.* **Submitted**.
- Khanal O, Kumar V, Schlegel F, Lenhoff AM. 2020b. Estimating and leveraging protein diffusion on ion-exchange resin surfaces. *Proc. Natl. Acad. Sci. U. S. A.* **117**:7004–7010.

- Khanal O, Kumar V, Westerberg K, Schlegel F, Lenhoff AM. 2019a. Multi-column displacement chromatography for separation of charge variants of monoclonal antibodies. *J. Chromatogr. A* **1586**:40–51.
- Khanal O, Singh N, Traylor SJ, Xu X, Ghose S, Li ZJ, Lenhoff AM. 2018. Contributions of depth filter components to protein adsorption in bioprocessing. *Biotechnol. Bioeng.* **115**:1938–1948.
- Khanal O, Xu X, Singh N, Traylor SJ, Huang C, Ghose S, Li ZJ, Lenhoff AM. 2019b. DNA retention on depth filters. *J. Memb. Sci.* **570–571**:464–471.
- Khawli LA, Goswami S, Hutchinson R, Kwong ZW, Yang J, Wang X, Yao Z, Sreedhara A, Cano T, Tesar DB, Nijem I, Allison DE, Wong PY, Kao Y-H, Quan C, Joshi A, Harris RJ, Motchnik P. 2010. Charge variants in IgG1: isolation, characterization, in vitro binding properties and pharmacokinetics in rats. *MAbs* **2**:613–624.
- Kim YN, Lee YC, Choi M. 2013. Complete degradation of perchlorate using Pd/N-doped activated carbon with adsorption/catalysis bifunctional roles. *Carbon N. Y.* **65**:315–323.
- Kline SR. 2006. Reduction and analysis of SANS and USANS data using IGOR Pro. *J. Appl. Crystallogr.* **39**:895–900.
- Knight R, Ostreicher E. 1998. Charge-modified filter media. In: Meltzer, TH, Jornitz, MW, editors. *Filtr. Biopharm. Ind.* New York: Marcel Dekker, pp. 95–125.
- Kondo A, Oku S, Higashitani K. 1991. Adsorption of γ -globulin, a model protein for antibody, on colloidal particles. *Biotechnol. Bioeng.* **37**:537–543.
- Kopaciewicz W, Rounds MA, Fausnaugh J, Regnier FE. 1983. Retention model for high-performance ion-exchange chromatography. *J. Chromatogr. A* **266**:3–21.
- Koshari SHS, Wagner NJ, Lenhoff AM. 2015. Characterization of lysozyme adsorption in cellulosic chromatographic materials using small-angle neutron scattering. *J. Chromatogr. A* **1399**:45–52.
- Koshari SHS, Wagner NJ, Lenhoff AM. 2018. Effects of resin architecture and protein size on nanoscale protein distribution in ion-exchange media. *Langmuir* **34**:673–684.

- Kotasińska M, Richter V, Thiemann J, Schlüter H. 2012. Cation exchange displacement batch chromatography of proteins guided by screening of protein purification parameters. *J. Sep. Sci.* **35**:3170–3176.
- Kumar V, Leweke S, von Lieres E, Rathore AS. 2015. Mechanistic modeling of ion-exchange process chromatography of charge variants of monoclonal antibody products. *J. Chromatogr. A* **1426**:140–153.
- Kumar V, Rathore AS. 2017. Mechanistic Modeling Based PAT Implementation for Ion-Exchange Process Chromatography of Charge Variants of Monoclonal Antibody Products. *Biotechnol. J.* **12**:1700286.
- Latulippe DR, Zydney AL. 2010. Radius of gyration of plasmid DNA isoforms from static light scattering. *Biotechnol. Bioeng.* **107**:134–142.
- Leblanc Y, Ramon C, Bihoreau N, Chevreux G. 2017. Charge variants characterization of a monoclonal antibody by ion exchange chromatography coupled on-line to native mass spectrometry: Case study after a long-term storage at +5 °C. *J. Chromatogr. B Anal. Technol. Biomed. Life Sci.* **1048**:130–139.
- Lee YF, Schmidt M, Graalfs H, Hafner M, Frech C. 2015. Modeling of dual gradient elution in ion exchange and mixed-mode chromatography. *J. Chromatogr. A* **1417**:64–72.
- Lenhoff AM. 2008. Multiscale modeling of protein uptake patterns in chromatographic particles. *Langmuir* **24**:5991–5995.
- Lesins V, Ruckenstein E. 1988. Patch controlled attractive electrostatic interactions between similarly charged proteins and adsorbents. *Colloid Polym. Sci.* **266**:1187–1190.
- Levy NE, Valente KN, Choe LH, Lee KH, Lenhoff AM. 2014. Identification and characterization of host cell protein product-associated impurities in monoclonal antibody bioprocessing. *Biotechnol. Bioeng.* **111**:904–912.
- Levy NE, Valente KN, Lee KH, Lenhoff AM. 2016. Host cell protein impurities in chromatographic polishing steps for monoclonal antibody purification. *Biotechnol. Bioeng.* **113**:1260–1272.
- Li Y, Fu T, Liu T, Guo H, Guo Q, Xu J, Zhang D, Qian W, Dai J, Li B, Guo Y, Hou S, Wang H. 2016. Characterization of alanine to valine sequence variants in the Fc region of nivolumab biosimilar produced in Chinese hamster ovary cells. *MAbs* **8**:951–960.

- von Lieres E, Andersson J. 2010. A fast and accurate solver for the general rate model of column liquid chromatography. *Comput. Chem. Eng.* **34**:1180–1191.
- Lin YC, Li C, Fakhraai Z. 2018. Kinetics of Surface-Mediated Fibrillization of Amyloid- β (12-28) Peptides. *Langmuir* **34**:4665–4672.
- Liu HF, Ma J, Winter C, Bayer R. 2010. Recovery and purification process development for monoclonal antibody production. *MAbs* **2**:480–499.
- Liu HF, McCooley B, Duarte T, Myers DE, Hudson T, Amanullah A, van Reis R, Kelley BD. 2011. Exploration of overloaded cation exchange chromatography for monoclonal antibody purification. *J. Chromatogr. A* **1218**:6943–6952.
- Liu H, Tang K. 2008. US2008/0058507A1 Method for the Removal of Aggregate Proteins from Recombinant Samples Using Ion Exchange Chromatography. U.S.: U.S. Patent Application 10/589,068.
- Liu J, Nguyen MDH, Andya JD, Shire SJ. 2005. Reversible self-association increases the viscosity of a concentrated monoclonal antibody in aqueous solution. *J. Pharm. Sci.* **94**:1928–1940.
- Ljunglöf A, Lacki KM, Mueller J, Harinarayan C, Van Reis R, Fahrner R, Van Alstine JM. 2007. Ion exchange chromatography of antibody fragments. *Biotechnol. Bioeng.* **96**:515–524.
- Low D, O’Leary R, Pujar NS. 2007. Future of antibody purification. *J. Chromatogr. B Anal. Technol. Biomed. Life Sci.* **848**:48–63.
- Lu JR, Perumal S, Zhao X, Miano F, Enea V, Heenan RR, Penfold J. 2005. Surface-induced unfolding of human lactoferrin. *Langmuir* **21**:3354–3361.
- Luo H, Macapagal N, Newell K, Man A, Parupudi A, Li Y, Li Y. 2014. Effects of salt-induced reversible self-association on the elution behavior of a monoclonal antibody in cation exchange chromatography. *J. Chromatogr. A* **1362**:186–193.
- Lützenkirchen J, Preočanin T, Kovačević D, Tomišić V, Lövgren L, Kallay N. 2012. Potentiometric titrations as a tool for surface charge determination. *Croat. Chem. Acta* **85**:391–417.
- Marichal-Gallardo PA, Álvarez MM. 2012. State-of-the-art in downstream processing of monoclonal antibodies: Process trends in design and validation. *Biotechnol. Prog.* **28**:899–916.

- Maschio C, Arruda ACF. 2000. Application of X-ray computerized tomography to characterize particle retention within depth filters. *Part. Part. Syst. Charact.* **17**:28–32.
- Matijević E. 1979. Principles of colloid and surface chemistry. *J. Colloid Interface Sci.* **70**:399.
- Medved' I, Černý R. 2011. Surface diffusion in porous media: A critical review. *Microporous Mesoporous Mater.* **142**:405–422.
- Michaeli I, Absolom DR, Van Oss CJ. 1980. Diffusion of adsorbed protein within the plane of adsorption. *J. Colloid Interface Sci.* **77**:586–587.
- Miyabe K, Guiochon G. 2000. Kinetic study of the mass transfer of bovine serum albumin in anion-exchange chromatography. *J. Chromatogr. A* **866**:147–171.
- Miyabe K, Guiochon G. 2010. Surface diffusion in reversed-phase liquid chromatography. *J. Chromatogr. A* **1217**:1713–1734.
- Moore W V., Leppert P. 1980. Role of aggregated human growth hormone (hGH) in development of antibodies to hGH. *J. Clin. Endocrinol. Metab.* **51**:691–697.
- Morris AM, Watzky MA, Finke RG. 2009. Protein aggregation kinetics, mechanism, and curve-fitting: A review of the literature. *Biochim. Biophys. Acta - Proteins Proteomics* **1794**:375–397.
- Mulcahy AW, Hlavka JP, Case SR. 2018. Biosimilar Cost Savings in the United States: Initial Experience and Future Potential. *Rand Heal. Q.* **7**:3.
- Müller-Späth T, Krättli M, Aumann L, Ströhlein G, Morbidelli M. 2010. Increasing the activity of monoclonal antibody therapeutics by continuous chromatography (MCSGP). *Biotechnol. Bioeng.* **107**:652–662.
- Müller-Späth T, Aumann L, Melter L, Ströhlein G, Morbidelli M. 2008. Chromatographic separation of three monoclonal antibody variants using multicolumn countercurrent solvent gradient purification (MCSGP). *Biotechnol. Bioeng.* **100**:1166–1177.
- Müller E. 2005. Properties and characterization of high capacity resins for biochromatography. *Chem. Eng. Technol.* **28**:1295–1305.
- Murray K, Ang CE, Gull K, Hickman JA, Dickson AJ. 1996. NSO myeloma cell death: Influence of bcl-2 overexpression. *Biotechnol. Bioeng.* **51**:298–304.

- National Academies of Sciences, Engineering and M. 2017. Preparing for future products of biotechnology. Washington, DC: National Academies Press. 1–212 p.
- National institute of Health. 2018. Cancer Statistics. <https://www.cancer.gov/about-cancer/understanding/statistics>.
- Ng P, Mitra G. 1994. Removal of DNA contaminants from therapeutic protein preparations. *J. Chromatogr. A* **658**:459–463.
- Nishi H, Miyajima M, Nakagami H, Noda M, Uchiyama S, Fukui K. 2010. Phase separation of an IgG1 antibody solution under a low ionic strength condition. *Pharm. Res.* **27**:1348–1360.
- Nygren H, Alaeddin S, Lundström I, Magnusson KE. 1994. Effect of surface wettability on protein adsorption and lateral diffusion. Analysis of data and a statistical model. *Biophys. Chem.* **49**:263–272.
- Oberholzer MR, Lenhoff AM. 1999. Protein adsorption isotherms through colloidal energetics. *Langmuir* **15**:3905–3914.
- Onur A, Shanmugam K, Ng A, Garnier G, Batchelor W. 2019. Cellulose fibre- perlite depth filters with cellulose nanofibre top coating for improved filtration performance. *Colloids Surfaces A Physicochem. Eng. Asp.* **583**:123997.
- Oo C, Kalbag SS. 2016. Leveraging the attributes of biologics and small molecules, and releasing the bottlenecks: a new wave of revolution in drug development. *Expert Rev. Clin. Pharmacol.* **9**:747–749.
- Park S, Venditti RA, Jameel H, Pawlak JJ. 2006. Changes in pore size distribution during the drying of cellulose fibers as measured by differential scanning calorimetry. *Carbohydr. Polym.* **66**:97–103.
- Parker J, Pollard JW, Friesen JD, Stanners CP. 1978. Stuttering: high-level mistranslation in animal and bacterial cells. *Proc. Natl. Acad. Sci. U. S. A.* **75**:1091–1095.
- Persson O, Andersson N, Nilsson B. 2018. Design of two-column batch-to-batch recirculation to enhance performance in ion-exchange chromatography. *J. Chromatogr. A* **1531**:112–121.
- Petricciani JC, Horaud FN. 1995. DNA, dragons and sanity. *Biologicals* **23**:233–238.
- Reck JM, Pabst TM, Hunter AK, Carta G. 2017. Separation of antibody monomer-dimer mixtures by frontal analysis. *J. Chromatogr. A* **1500**:96–104.

- Remmele RL, Callahan WJ, Krishnan S, Zhou L, Bondarenko P V., Nichols AC, Kleemann GR, Pipes GD, Park S, Fodor S, Kras E, Brems DN. 2006. Active dimer of epratuzumab provides insight into the complex nature of an antibody aggregate. *J. Pharm. Sci.* **95**:126–145.
- Roberts CJ. 2007. Non-native protein aggregation kinetics. *Biotechnol. Bioeng.* **98**:927–938.
- Rouquerol J, Llewellyn P, Rouquerol F. 2007. Is the BET equation applicable to microporous adsorbents? *Stud. Surf. Sci. Catal.* **160**:49–56.
- Russo E. 2003. Special report: The birth of biotechnology. *Nature* **421**:456–457.
- Rybka J, Hölzel A, Melnikov SM, Seidel-Morgenstern A, Tallarek U. 2015. A new view on surface diffusion from molecular dynamics simulations of solute mobility at chromatographic interfaces. *Fluid Phase Equilib.* **407**:177–187.
- Rybka J, Hölzel A, Tallarek U. 2017. Surface Diffusion of Aromatic Hydrocarbon Analytes in Reversed-Phase Liquid Chromatography. *J. Phys. Chem. C* **121**:17907–17920.
- Sadavarte R, Madadkar P, Filipe CD, Ghosh R. 2018. Rapid preparative separation of monoclonal antibody charge variants using laterally-fed membrane chromatography. *J. Chromatogr. B Anal. Technol. Biomed. Life Sci.* **1073**:27–33.
- Salic A, Mitchison TJ. 2008. A chemical method for fast and sensitive detection of DNA synthesis in vivo. *Proc. Natl. Acad. Sci. U. S. A.* **105**:2415–2420.
- Sanchez-Sevilla A, Thimonier J, Marilley M, Rocca-Serra J, Barbet J. 2002. Accuracy of AFM measurements of the contour length of DNA fragments adsorbed on mica in air and in aqueous buffer. *Ultramicroscopy* **92**:151–158.
- Santos MAS, Tuite MF. 1993. New insights into mRNA decoding - implications for heterologous protein synthesis. *Trends Biotechnol.* **11**:500–505.
- Schmidt-Traub H. 2005. Preparative chromatography: of fine chemicals and pharmaceutical agents. John Wiley & Sons. 1–458 p.
- Schreffler J, Bailey M, Klimek T, Agneta P, Wiltsie WE, Felo M, Maisey P, Zuo X, Routhier E. 2015. Characterization of postcapture impurity removal across an adsorptive depth filter. *Bioprocess Int.* **13**:36–45.

- Sharma MK, Raikar S, Srivastava S, Gupta SK. 2017. Examining single-use harvest clarification options: A case study comparing depth-filter turbidities and recoveries. *Bioprocess Int.* **15**.
- Shen L, Adachi T, Vanden Bout D, Zhu XY. 2012. A mobile precursor determines amyloid- β peptide fibril formation at interfaces. *J. Am. Chem. Soc.* **134**:14172–14178.
- Shibata CT, Lenhoff AM. 1992. TIRF of salt and surface effects on protein adsorption. II. Kinetics. *J. Colloid Interface Sci.* **148**:485–507.
- Shibayama M. 1998. Spatial inhomogeneity and dynamic fluctuations of polymer gels. *Macromol. Chem. Phys.* **199**:1–30.
- Shukla AA, Hubbard B, Tressel T, Guhan S, Low D. 2007. Downstream processing of monoclonal antibodies-Application of platform approaches. *J. Chromatogr. B Anal. Technol. Biomed. Life Sci.* **848**:28–39.
- Sifniotis V, Cruz E, Eroglu B, Kayser V. 2019. Current Advancements in Addressing Key Challenges of Therapeutic Antibody Design, Manufacture, and Formulation. *Antibodies* **8**:36.
- Singh N, Arunkumar A, Peck M, Voloshin AM, Moreno AM, Tan Z, Hester J, Borys MC, Li ZJ. 2017. Development of adsorptive hybrid filters to enable two-step purification of biologics. *MAbs* **9**:350–363.
- Sivia D. 2012. Elementary scattering theory for X-ray and neutron users. Oxford University Press. Vol. 23 35–35 p.
- Smith DE, Perkins TT, Chu S. 1996. Dynamical Scaling of DNA Diffusion Coefficients. *Macromolecules* **29**:1372–1373.
- Smith SL. 1996. Ten years of Orthoclone OKT3 (muromonab-CD3): A review. *J. Transpl. Coord.* **6**:109–119.
- Somasundaram B, Pleitt K, Shave E, Baker K, Lua LHL. 2018. Progression of continuous downstream processing of monoclonal antibodies: Current trends and challenges. *Biotechnol. Bioeng.* **115**:2893–2907.
- Srajer Gajdosik M, Clifton J, Josic D. 2012. Sample displacement chromatography as a method for purification of proteins and peptides from complex mixtures. *J. Chromatogr. A* **1239**:1–9.

- Stana-Kleinschek K, Ribitsch V. 1998. Electrokinetic properties of processed cellulose fibers. In: . *Colloids Surfaces A Physicochem. Eng. Asp.*, Vol. 140, pp. 127–138.
- Stone MT, Cotoni KA, Stoner JL. 2019. Cation exchange frontal chromatography for the removal of monoclonal antibody aggregates. *J. Chromatogr. A* **1599**:152–160.
- Stone MC, Tao Y, Carta G. 2009. Protein adsorption and transport in agarose and dextran-grafted agarose media for ion exchange chromatography: Effect of ionic strength and protein characteristics. *J. Chromatogr. A* **1216**:4465–4474.
- Storck S, Bretinger H, Maier WF. 1998. Characterization of micro- and mesoporous solids by physisorption methods and pore-size analysis. *Appl. Catal. A Gen.* **174**:137–146.
- Subramanian G ed. 2017. Continuous biomanufacturing - Innovative technologies and methods. *Contin. Biomanufacturing - Innov. Technol. Methods*. John Wiley & Sons.
- Suda EJ, Thomas KE, Pabst TM, Mensah P, Ramasubramanyan N, Gustafson ME, Hunter AK. 2009. Comparison of agarose and dextran-grafted agarose strong ion exchangers for the separation of protein aggregates. *J. Chromatogr. A* **1216**:5256–5264.
- Svergun DI, Richard S, Koch MHJ, Sayers Z, Kuprin S, Zaccai G. 1998. Protein hydration in solution: Experimental observation by x-ray and neutron scattering. *Proc. Natl. Acad. Sci. U. S. A.* **95**:2267–2272.
- Tan Q, Guo Q, Fang C, Wang C, Li B, Wang H, Li J, Guo Y. 2012. Characterization and comparison of commercially available TNF receptor 2-Fc fusion protein products. *MAbs* **4**:761–774.
- Tan YH, Liu M, Nolting B, Go JG, Gervay-Hague J, Liu GY. 2008. A nanoengineering approach for investigation and regulation of protein immobilization. *ACS Nano* **2**:2374–2384.
- Tauer C, Buchacher A, Jungbauer A. 1995. DNA clearance in chromatography of proteins, exemplified by affinity chromatography. *J. Biochem. Biophys. Methods* **30**:75–78.
- Thomas H, Coquebert de Neuville B, Storti G, Morbidelli M, Joehnck M, Schulte M. 2013. Role of tentacles and protein loading on pore accessibility and mass transfer in cation exchange materials for proteins. *J. Chromatogr. A* **1285**:48–56.

- Tilton RD, Robertson CR, Gast AP. 1990. Lateral diffusion of bovine serum albumin adsorbed at the solid-liquid interface. *J. Colloid Interface Sci.* **137**:192–203.
- Tiselius A. 1943. Displacement development in adsorption analysis. *Ark. Kemi. Miner. Geol.* **16**:1–18.
- Ulmer N, Vogg S, Müller-Späth T, Morbidelli M. 2019. Purification of human monoclonal antibodies and their fragments. In: . *Methods Mol. Biol.*, Vol. 1904, pp. 163–188.
- Vanderlaan M, Zhu-Shimoni J, Lin S, Gunawan F, Waerner T, Van Cott KE. 2018. Experience with host cell protein impurities in biopharmaceuticals. *Biotechnol. Prog.* **34**:828–837.
- Vázquez-Rey M, Lang DA. 2011. Aggregates in monoclonal antibody manufacturing processes. *Biotechnol. Bioeng.* **108**:1494–1508.
- Veeraragavan K, Bernier A, Braendli E. 1991. Sample displacement mode chromatography: purification of proteins by use of a high-performance anion-exchange column. *J. Chromatogr. A* **541**:207–220.
- Vlasak J, Ionescu R. 2011. Fragmentation of monoclonal antibodies. *MAbs* **3**:253–263.
- Vogg S, Müller-Späth T, Morbidelli M. 2020a. Design space and robustness analysis of batch and counter-current frontal chromatography processes for the removal of antibody aggregates. *J. Chromatogr. A* **1619**:460943.
- Vogg S, Pfeifer F, Ulmer N, Morbidelli M. 2020b. Process intensification by frontal chromatography: Performance comparison of resin and membrane adsorber for monovalent antibody aggregate removal. *Biotechnol. Bioeng.* **117**:662–672.
- Voitl A, Butté A, Morbidelli M. 2010. Behavior of human serum albumin on strong cation exchange resins: I. Experimental analysis. *J. Chromatogr. A* **1217**:5484–5491.
- Voordouw G, Kam Z, Borochoy N, Eisenberg H. 1978. Isolation and physical studies of the intact supercoiled. The open circular and the linear forms of CoIE1-plasmid DNA. *Biophys. Chem.* **8**:171–189.
- Walsh G. 2010. Biopharmaceutical benchmarks 2010. *Nat. Biotechnol.* **28**:917–924.

- Wang D, Chin HY, He C, Stoykovich MP, Schwartz DK. 2016. Polymer surface transport is a combination of in-plane diffusion and desorption-mediated flights. *ACS Macro Lett.* **5**:509–514.
- Wang D, He C, Stoykovich MP, Schwartz DK. 2015. Nanoscale topography influences polymer surface diffusion. *ACS Nano* **9**:1656–1664.
- Wang H, Meng S, Guo K, Liu Y, Yang P, Zhong W, Liu B. 2008. Microfluidic immunosensor based on stable antibody-patterned surface in PMMA microchip. *Electrochem. commun.* **10**:447–450.
- Wang X, Maloney TC, Paulapuro H. 2003. Internal fibrillation in never-dried and once-dried chemical pulps. *Appita J.* **56**:455–459.
- Weaver LE, Carta G. 1996. Protein adsorption on cation exchangers: Comparison of macroporous and gel-composite media. *Biotechnol. Prog.* **12**:342–355.
- Wesselingh JA, Bosma JC. 2001. Protein ion-exchange adsorption kinetics. *AIChE J.* **47**:1571–1580.
- Wierenga DE, Cogan J, Petricciani JC. 1995. Administration of tumor cell chromatin to immunosuppressed and non-immunosuppressed non-human primates. *Biologicals* **23**:221–224.
- Wollacott R, Roth L, Sears T, Sharpe R, Jiang M, Ozturk S. 2015. The development of a flow-through mode cation exchange process for the purification of a monoclonal antibody. *Bioprocess. J.* **14**:5–13.
- Woo M, Yavorsky D, Amara J, Singh N. 2015. High capacity composite depth filter media with low extractables. Google Patents. <https://www.google.ch/patents/US20160114272>.
- Woodcock J, Woosley R. 2008. The FDA critical path initiative and its influence on new drug development. *Annu. Rev. Med.* **59**:1–12.
- Wu SY. 2000. Green A: Projection of chronic illness prevalence and costs inflation. *RAND Corp.*
- Wurm FM. 2004. Production of recombinant protein therapeutics in cultivated mammalian cells. *Nat. Biotechnol.* **22**:1393–1398.
- Wyllie AH. 1980. Glucocorticoid-induced thymocyte apoptosis is associated with endogenous endonuclease activation. *Nature* **284**:555–556.

- Xiao Z, Yin X, Han L, Sun B, Shen Z, Liu W, Yu F. 2018. A comprehensive approach for evaluating charge heterogeneity in biosimilars. *Eur. J. Pharm. Sci.* **115**:19–24.
- Yang H, Viera C, Fischer J, Etzel MR. 2002. Purification of a large protein using ion-exchange membranes. *Ind. Eng. Chem. Res.* **41**:1597–1602.
- Yao Y, Lenhoff AM. 2006. Pore size distributions of ion exchangers and relation to protein binding capacity. *J. Chromatogr. A* **1126**:107–119.
- Yearley EJ, Godfrin PD, Perevozchikova T, Zhang H, Falus P, Porcar L, Nagao M, Curtis JE, Gawande P, Taing R, Zarraga IE, Wagner NJ, Liu Y. 2014. Observation of small cluster formation in concentrated monoclonal antibody solutions and its implications to solution viscosity. *Biophys. J.* **106**:1763–1770.
- Yigzaw Y, Piper R, Tran M, Shukla AA. 2006a. Exploitation of the adsorptive properties of depth filters for host cell protein removal during monoclonal antibody purification. *Biotechnol. Prog.* **22**:288–296.
- Yigzaw Y, Piper R, Tran M, Shukla AA. 2006b. Exploitation of the adsorptive properties of depth filters for host cell protein removal during monoclonal antibody purification. *Biotechnol. Prog.* **22**:288–296.
- Yoon Y, Lueptow RM. 2006. Concentration of colloidal silica suspensions using fluorescence spectroscopy. *Colloids Surfaces A Physicochem. Eng. Asp.* **277**:107–110.
- Yoshida H, Yoshikawa M, Kataoka T. 1994. Parallel transport of BSA by surface and pore diffusion in strongly basic chitosan. *AIChE J.* **40**:2034–2044.
- Zhang S, Iskra T, Daniels W, Salm J, Gallo C, Godavarti R, Carta G. 2017. Structural and performance characteristics of representative anion exchange resins used for weak partitioning chromatography. *Biotechnol. Prog.* **33**:425–434.
- Zhang T, Bourret J, Cano T. 2011. Isolation and characterization of therapeutic antibody charge variants using cation exchange displacement chromatography. *J. Chromatogr. A* **1218**:5079–86.
- Zhao J, Granick S. 2004. Polymer lateral diffusion at the solid-liquid interface. *J. Am. Chem. Soc.* **126**:6242–6243.
- Zhao J, Granick S. 2007. How polymer surface diffusion depends on surface coverage. *Macromolecules* **40**:1243–1247.

- Zhou JX, Dermawan S, Solamo F, Flynn G, Stenson R, Tressel T, Guhan S. 2007. pH-conductivity hybrid gradient cation-exchange chromatography for process-scale monoclonal antibody purification. *J. Chromatogr. A* **1175**:69–80.
- Zhu-Shimoni J, Yu C, Nishihara J, Wong RM, Gunawan F, Lin M, Krawitz D, Liu P, Sandoval W, Vanderlaan M. 2014. Host cell protein testing by ELISAs and the use of orthogonal methods. *Biotechnol. Bioeng.* **111**:2367–2379.
- Zhu M, Fuks P, Carta G. 2018. Protein adsorption in anion exchange resins – effects of polymer grafting, support structure porosity, and protein size. *J. Chem. Technol. Biotechnol.* **93**:1948–1958.
- Zobel-Roos S, Schmidt A, Mestmäcker F, Mouellef M, Huter M, Uhlenbrock L, Kornecki M, Lohmann L, Ditz R, Strube J. 2019. Accelerating biologics manufacturing by modeling or: Is Approval under the QbD and PAT approaches demanded by authorities acceptable without a digital-twin? *Processes* **7**:94.

Appendix

PUBLICATION REPRINT PERMISSIONS

Portions of Chapter 2 are reproduced with permission from reference (Khanal et al., 2018). Copyright (2018) John Wiley and Sons.

Portions of Chapter 3 are reproduced from reference (Khanal et al., 2019b). Copyright (2019) Elsevier.

Portions of Chapter 4 are reproduced from reference (Khanal et al., 2020b). Copyright (2020) National Academy of Sciences.

Portions of Chapter 5 are reproduced from reference (Khanal et al., 2019a). Copyright (2019) Elsevier.

Portions of Chapter 6 are reproduced from reference (Khanal et al., 2020a).